An Investigation of Mixing and Transport at a Sheared Density Interface

Thesis by

Gregory Daniel Sullivan

In Partial Fulfillment of the Requirements

for the Degree of

Doctor of Philosophy

California Institute of Technology

Pasadena, California

1992

(submitted April 24, 1992)

Acknowledgements

Abstract

Scalar transport is investigated at a density interface imbedded in a turbulent shear flow. This problem is investigated first experimentally, and based on the experimental findings, a physical model for entrainment is developed.

Steady-state interfacial shear flows are generated in a laboratory water channel for layer Richardson numbers, Ri, between about 1 and 10. The flow field is made optically homogeneous, enabling the combined use of laser-Doppler velocimetry and laser-induced fluorescence with photodiode array imaging to measure the velocity and concentration fields at high resolution.

False-color images of the concentration field provide valuable insight into mixing and transport at the interface. The dominant interfacial mixing mechanism is found to depend on the local mean shear Richardson number, Ri_S: for Ri_S less than about 0.40 to 0.45, local mixing is dominated by Kelvin-Helmholtz (K-H) instabilities; for somewhat larger values of Ri_S, mixing is dominated by interfacial wave breaking. In both cases, vertical transport of mixed fluid into adjacent turbulent layers is accomplished by large-scale turbulent eddies which impinge on the interface and scour fluid from its outer edges.

Based on the experimental results, a model for interfacial mixing and entrainment is developed. A local equilibrium is assumed in which the rate of loss of interfacial fluid by eddy scouring is balanced by the rate of production (local mixing) by interfacial instabilities and molecular diffusion. In the case of one-sided entrainment, the model results are as follows: when interfacial mixing is diffusion dominated, $\delta/h \sim Pe^{-1/2}$ and $E \sim Ri^{-1}Pe^{-1/2}$, where δ is the interface thickness, h is the boundary layer thickness, Pe is the Péclet number, and E is the normalized entrainment velocity; when mixing is wave breaking dominated, $\delta/h \sim Ri^{-1/2}$ and $E \sim Ri^{-3/2}$; and when mixing

is K-H dominated, $\delta/h \sim Ri^{-1}$ and $E \sim Ri^{-2}$. In all cases the maximum concentration anomaly is $\Gamma_m \sim Ri^{-1}$. The model for single-sided entrainment is simply extended to the case in which both layers are entraining. In the latter case it is found that entrainment depends on combinations of parameters from both layers.

The proposed entrainment model is supported by experimental results from this and previous studies. The data from this study are in agreement with $\Gamma_m \sim Ri^{-1}$ and are consistent with model results for δ/h; results from previous studies support model predictions for E and δ/h.

Table of Contents

List of Figures

List of Tables

List of Symbols

English

a	wave amplitude
a_B	maximum billow height
a, a_u, a_v	major diameter of ellipsoidal focal volume
a_f	flowmeter calibration coefficient
a_p	particle radius
A	calibration coefficient for LDV signal processor
A	parameter in error calculation
b, b_u, b_v	minor diameter of ellipsoidal focal volume
b_f	flowmeter calibration coefficient
B	calibration coefficient for LDV signal processor
B	parameter in error calculation
c	speed of light
$c(y,t)$	concentration
$\bar{c}$	mean concentration
c'	rms concentration
c_∞	mean concentration at outer edge of layer
C	normalized area of distorted interface
C_i	dye concentration corresponding to i^{th} pixel
C_0	unmixed fluid dye concentration
d	depth of single layer
d_i	depth of eddy penetration into interface
D	mixed layer depth
D_i	dark (pixel) response

e_{pe}	rate of gain of potential energy
e_s	rate of supply of energy
E_0, E_2, E_r, E_s	electric field amplitudes
E	normalized entrainment velocity
E(f)	power spectral density
$\hat{\mathbf{e}}_1$, $\hat{\mathbf{e}}_2$	unit vectors
f_0, f_1, f_2	light frequencies
f_c	cut-off frequency
f_D	Doppler frequency shift
f_e	frequency of eddy interaction
f_m	measured input signal frequency
F	Bragg cell relative frequency shift
F_1, F_2	internal Froude numbers
g	acceleration due to gravity
h_0, h_1	boundary layer thicknesses
h_s	velocity gradient thickness
H	total depth of two fluid system
H_i	optical transfer function
i	current
I	laser beam intensity
k', k'_u, k'_v	constants used in velocity determination
k	wavenumber
k	von-Kármán constant
K	probability threshold
l	eddy size
l_R	Ozmidov scale

l_1	distance from measurement site to upper layer entrance splitter tip
l_2	distance from measurement site to lower layer entrance splitter tip
L	length used in LDV angle determination
L	Monin-Obukhov length
L_b	length of calibration box
M_f, M_s, M_w	mass of flask: dry, with saline solution, and with ethanol solution
n	index of refraction
N	number of samples
N	Brunt-Väisälä frequency
N(f)	noise spectrum
Pe	layer Péclet number
Q	volumetric flowrate
Q_1	inflowrate of alcohol-water
Q_2	inflowrate of saline solution
Q_3	outflowrate of alcohol-water
Q_4	outflowrate of saline solution
R	flowmeter reading
Re	layer Reynolds number
Ri	layer Richardson number
Ri*	layer Richardson number based on u*
Ri_b	maximum Ri for wave breaking
Ri_c	maximum Ri for K-H instabilities
Ri_g	mean gradient Richardson number
Ri_{gc}	critical mean gradient Richardson number
Ri_s	mean shear Richardson number

Ri_{sc}	critical mean shear Richardson number
Ri_t	maximum Ri for turbulent interface
t	time
t_a	available time for fluid incorporation
t_e	eddy turnover time
t_i	average duration of eddy interaction
t_s	time for successive K-H instability
T	total sample time
u	streamwise velocity
u	eddy fluctuating velocity scale
u'	velocity component measured by LDV
u'	rms horizontal velocity
u	velocity vector
u_*	shear velocity
u_e	entrainment velocity
u_i	mean interface velocity
u_i	i^{th} measured value of u
$\overline{u}$	sample mean value of u
u_{GB}	volume gained by wave breaking
u_{GD}	volume gained by molecular diffusion
u_{GKH}	volume gained by K-H instabilities
u_L	volume lost by eddy scouring
U	velocity measured by LDV
U	mean layer velocity
U_0, U_1	free stream velocities
v	vertical velocity
v'	velocity component measured by LDV

v'	rms vertical velocity
v_i	i^{th} measured value of v
$\overline{v}$	sample mean value of v
V	voltage
V_i, V_{ci}	output voltage from the i^{th} pixel
w_1, w_2	lengths used in LDV angle determination
$\hat{x}'$, $\hat{y}'$, $\hat{x}$, $\hat{y}$	unit vectors

Greek

β	angle used in LDV measurement
δ	mean interface thickness
δ_0, δ_1	interface half-widths
Δb	buoyancy difference
ΔC	concentration difference
$\Delta \rho$	density difference
ΔU	mean velocity difference
Δy	distance between measurements along laser beam
$\Delta(f,F,u,v,\beta,\gamma,\theta)$	error values
ε	dye attenuation coefficient
ε	efficiency of energy conversion
ε	dissipation rate
ϕ_0, ϕ_2	phase of electric fields
$\Phi(f)$	optimal filter
Φ_η	power spectral density for interface position
γ	angle used in LDV measurement
Γ	concentration anomaly

Γ_m	maximum concentration anomaly
κ	scalar molecular diffusivity
λ	wavelength of light
μ	viscosity
η	interface position
$\overline{\eta}$	mean interface position
ρ	fluid density
ρ_0	mean density of lower layer
ρ_1	mean density of upper layer
ρ_p	particle density
$-\rho\overline{u'v'}$	Reynolds stress
θ	normalized concentration
$\theta, \theta_u, \theta_v$	angle between scattering and reference beam
θ_{off}	angle between bisectrice of reference and scattering beam and normal to flume wall
ν	kinematic viscosity
σ_u^2	sample variance of u
σ_v^2	sample variance of v
τ_L	large-scale time
τ_s	surface stress
ξ_i	distance along laser beam
ω	circular wave frequency

CHAPTER 1

INTRODUCTION

1.1. General Background

Density interfaces occur commonly in a wide variety of flows of various scales. Geophysical (large-scale) examples include haloclines in stratified estuaries, temperature inversions in the atmospheric boundary layer, and thermoclines in the upper layer of the ocean. Engineering (smaller-scale) examples include thermal and wastewater discharges, methane gas flow in coal mines, artificial destratification in reservoirs, and surface layer flow in solar ponds.

In most flows of practical interest, the scales of length and velocity are (relatively) quite large, ensuring turbulent flow everywhere, except possibly very close to the interface. There buoyancy forces can be so great that turbulent motions are suppressed on all scales. The density interfaces in these flows are typically very sharp and are characteristically regions of high density and velocity gradient.

Attention is restricted in this study to cases in which the flow away from the interface is turbulent, but buoyancy forces in the interface are sufficiently large that the interfacial flow is laminar (except possibly during sporadic periods of instability). These cases comprise an important class of density-stratified shear flows due not only to their practical relevance, but also because advances in their understanding represent steps forward in understanding density stratified turbulence in general.

An idealized density interface is shown schematically in figure 1.1.1. A sharp interface of mean thickness δ separates fluid of density ρ_1, above, from fluid of density $\rho_1+\Delta\rho$, below. The layers have free stream velocities U_1 and U_0 and boundary layer

thicknesses† h_1 and h_0. The mean interface velocity is u_i and gravity acts vertically downward. In this problem a non-dimensional parameter of fundamental importance is the layer Richardson number given by

$$\mathrm{Ri} = \frac{\Delta b h}{(U - u_i)^2}, \tag{1.1.1}$$

where $\Delta b = g\Delta\rho/\rho_1$ is the buoyancy jump at the interface. The layer Richardson number represents the relative importance of buoyancy and inertial forces. If viscosity and molecular diffusion are important, then the layer Reynolds number

$$\mathrm{Re} = \frac{|U - u_i| h}{\nu}, \tag{1.1.2}$$

and Péclet number

$$\mathrm{Pe} = \frac{|U - u_i| h}{\kappa}, \tag{1.1.3}$$

are also relevant. Here ν is the kinematic viscosity and κ is the scalar diffusivity. In general, when both layers are turbulent and entraining, the parameters Ri_0, Ri_1, Re_0, Re_1, Pe_0, and Pe_1 govern the flow.

In problems of this type it is convenient to define an entrainment velocity, u_e, as the volume of equivalent adjacent layer fluid incorporated into a layer per unit area per unit time. u_e essentially determines the vertical transport of scalar across the interface, which is of great interest in geophysical and engineering density interfacial flows. In addition to controlling the concentrations of such important quantities as salt,

† The boundary layer thickness is loosely defined here as the thickness of the turbulent layer. A more precise definition is given in §3.1.

temperature, oxygen, and pollutant, entrainment also plays an important role in determining overall circulation patterns.

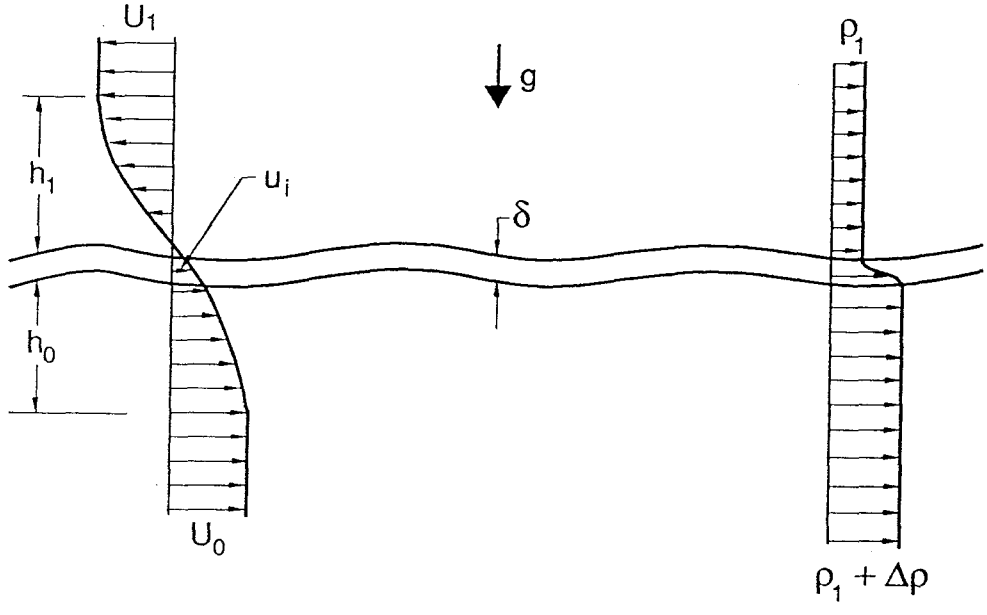

FIGURE 1.1.1. Idealized density interface.

A number of experimental studies have investigated aspects of the interfacial entrainment problem. Considerable attention has focussed on the determination of an entrainment 'law', or relation between normalized entrainment, $E=u_e/U$, and non-dimensional parameters governing the flow. However, there is currently no consensus on the form of such a relation.

In what follows, results relevant to the problem of mixing at a sheared density interface are reviewed. Results involving additional complicating factors such as rotation and double-diffusive convection are not considered. Also, results from shear-free experiments such as the grid-generated turbulence experiments of Hannoun &

List (1988) are not discussed, since it is questionable† whether results from zero-mean shear cases are germane to the sheared problem. Fernando (1991) reviews recent work done on the general problem of turbulent mixing at a density interface.

Sheared density interfaces have been investigated in a variety of experimental configurations. The first studies were performed by Ellison & Turner (1959) on surface jet flows and and on gravity currents flowing down a sloping floor. Following this, Lofquist (1960) investigated mixing between a horizontally flowing saline layer and ambient fresh water. Next, in an annular tank with an applied surface stress, Kato & Phillips (1969) investigated mixing between two fluid layers, the upper nearly homogeneous and the lower linearly stratified. Following this, Moore & Long (1971) investigated two-layer counterflows driven by horizontal jets issuing from the floor and ceiling of a racetrack-shaped tank. Later, Kantha, Phillips & Azad (1977) and Deardorff & Willis (1982) studied mixing in experiments similar to those of Kato & Phillips. More recently, Narimousa, Long & Kitaigorodskii (1986) and Stephensen & Fernando (1991) investigated two-layer flows in racetrack-shaped tanks; in their case the upper layer motion was driven by a specially designed disc pump.

Generally speaking, qualitative observations from the experiments are as follows. At low Ri, buoyancy inhibits massive interface convolutions, but small-scale turbulence persists at the interface and entrainment proceeds in a manner qualitatively similar to that at the outer edge of a turbulent boundary layer or jet. As Ri increases, the interface becomes less convoluted and regularly spaced Kelvin-Helmholtz (K-H) instabilities are observed. The unstable K-H waves grow and roll-up to form turbulent billows, similar to those observed by Thorpe (1973). The K-H instabilities generated at the sheared density interfaces are sporadic: they appear, grow, roll-up and collapse,

† The turbulence generated in the sheared case depends on the shear itself and, more importantly, the mean shear is believed to play an important role in interfacial mixing processes.

and after some time they form again. As Ri is further increased, the billow amplitudes decrease until finally K-H instabilities are no longer observed. At larger Ri, turbulent eddies are observed to impinge upon the interface and shear the crests off from interfacial waves. As Ri is further raised, interfacial wave activity is reduced, until finally the interface is completely flat and entrainment is purely diffusive.

Values of Ri marking the transition between mixing regimes vary somewhat with experiment; this may be attributed to the varying ways in which Ri is measured, and complicating effects such as secondary circulations, side-wall drag and additional sources of turbulence.

Quantitative results from the mixing experiments are as follows. Ellison & Turner studied entrainment over the range $0 < Ri < 0.8$ and found that E decreased rapidly with Ri, tending toward zero for values of Ri greater than about 0.8. Unfortunately, they could not obtain accurate estimates of E for values of Ri much greater than this, and since their experiments lie primarily in the range of Ri for which the interface is turbulent, their results are outside the scope of the present study. Studying a much wider range of Ri, $1 < Ri < 40$, Lofquist found that E decreased monotonically with increasing Ri, but did not follow a simple power law over the entire range. He also investigated the influence of Re on entrainment, but found no systematic dependence over the range studied. Moore & Long studied entrainment for $1 < Ri < 30$ and found that a relation of the form $E \sim Ri^{-1}$ fit their data reasonably well, however the introduction of additional length and velocity scales associated with the flow producing jets may have influenced their results.

Kato & Phillips scaled their results with the friction velocity, $u_* = \sqrt{\tau_S/\rho}$, where τ_S is the surface stress, and found that a relation of the form $E_* \sim Ri_*^{-1}$ represented their data reasonably well over the full Ri_* range studied, *viz.* $20 < Ri_* < 300$. Here

$E_* = u_e/u_*$ and Ri_* is based on u_*. Based on their results, they suggested a proportionality between the rate of increase of potential energy of the system and the rate of dissipation of turbulent kinetic energy in the mixed layer. Later, in studying a wider range of Ri_*, $30 < Ri_* < 1000$, Kantha, Azad & Phillips found no simple power law over the entire Ri_* range. Phillips (1977) then suggested that the relevant scaling velocity was the mean difference in velocity between the two layers, since shear-flow instabilities at the density interface appeared to initiate the entrainment process. With this in mind, Price (1979) attempted to re-scale the experiments of Kato & Phillips and Kantha, Azad & Phillips using a momentum balance and the assumption that Ri assumed a quasi-equilibrium value of about 0.6. He found that for $0.5 < Ri < 1$ the data were reasonably represented by $E \sim Ri^{-4}$. However, results from the experiments of Deardorff & Willis questioned the validity of the quasi-equilibrium Ri hypothesis, and further suggested that viscous diffusion of momentum was important, inasmuch as it reduced the velocity difference across the interface. Deardorff & Willis suggested that their data were well represented by $E_* \sim Ri^{-1.4}Ri_*^{-1/2}$.

More recently, Narimousa & Fernando (1987) analyzed the experiments of Narimousa, Long & Kitaigorodskii and found that the data were reasonably represented by $E \sim Ri^{-1}$ for $0.5 < Ri < 25$. They also found that normalized rms wave amplitudes were proportional to $Ri^{-1/2}$ and from this suggested that the energy gained by interfacial disturbances was proportional to the energy of large-scale eddies (which presumably generated them). Finally, using laser-induced fluorescence and video imaging, Stephensen & Fernando measured interfacial thicknesses and suggested that $\delta/h \sim Ri^{-1}$ for Ri less than about 5, and $\delta/h \sim$ constant for Ri greater than about 5.

As the results above show, there is currently no agreement on the form of an entrainment relation. Experimental peculiarities make comparisons difficult, especially in the absence of a theoretical model to suggest the basis on which experimental

results should be compared. Greatly needed is a self-consistent model for entrainment, based on physical principles, that can be (critically) verified experimentally.

1.2. Objectives

Given the current level of understanding of mixing processes in density interfacial flows, the objectives of this study are as follows:

(1) to investigate experimentally, with high resolution laser diagnostic techniques, scalar transport at a sheared density interface over a range of parameters for which the interface is quasi-laminar and the flow in at least one adjacent layer is turbulent;

(2) to identify important mechanisms involved in mixing and transport processes at the interface; and

(3) to develop a self-consistent model for the vertical transport of buoyancy (entrainment).

1.3. Overview

The following is an overview of the remaining sections of this work. In §2 the experimental facility used in this study is described in detail, including the flow generation system and the laser diagnostic systems. In §3 results obtained from five experiments are presented. In §4 experimental results are discussed, with particular emphasis on implications concerning mixing and transport processes at the density interface. In §5 a model for entrainment is developed. Model predictions are compared with experimental results and practical applications are discussed. Finally, in §6 a summary is given and suggestions are made for future work.

CHAPTER 2

EXPERIMENTAL FACILITY

2.1. Flume Layout and Flow Generation System

The facility used in this study is essentially a modified version of a flume built by Rasi (1989). Additional inlets and outlets (and associated flow management devises) have been installed at each end of the original flume to enable the generation of two-layer, quasi-equilibrium† flows over a range of conditions. The modified flume is shown schematically in figure 2.1.1.

The physical dimensions of the flume are as follows. The distance between the two inlets is 4.87 m (including the length of the splitter plates) and the flume extends an extra 1.80 m from the salt water inlet to the overflow weir. Between the two inlets the flume is 10 cm wide and has a depth capacity of 67 cm. Immediately behind the salt-water inlet (towards the overflow weir) there is a rectangular section of depth 85 cm, length 60 cm, and width 10 cm which leads to an outlet port below. Behind this section, the flume widens to 60 cm and is bounded at the rear by a sharp-crested overflow weir of height 20 cm.

The salt-water and fresh water inlets are shown in detail in figures 2.1.2 and 2.1.3, respectively. In each of the inlet sections, the flow passes through two series of aluminum honeycomb and brass screen. The aluminum honeycomb consists of hexagonal elements, spaced about 13 per cm^2, and the brass screens are 18 x 18 mesh. The purpose of the honeycomb and screens is to straighten the flow and to

† The flows are quasi-equilibrium in the sense that they are slowly varying in the longitudinal direction; flow variables may then be considered dependent on local values of governing parameters.

break larger-scale disturbances down to smaller-scales. They also act to enhance the physical integrity of the inlet section.

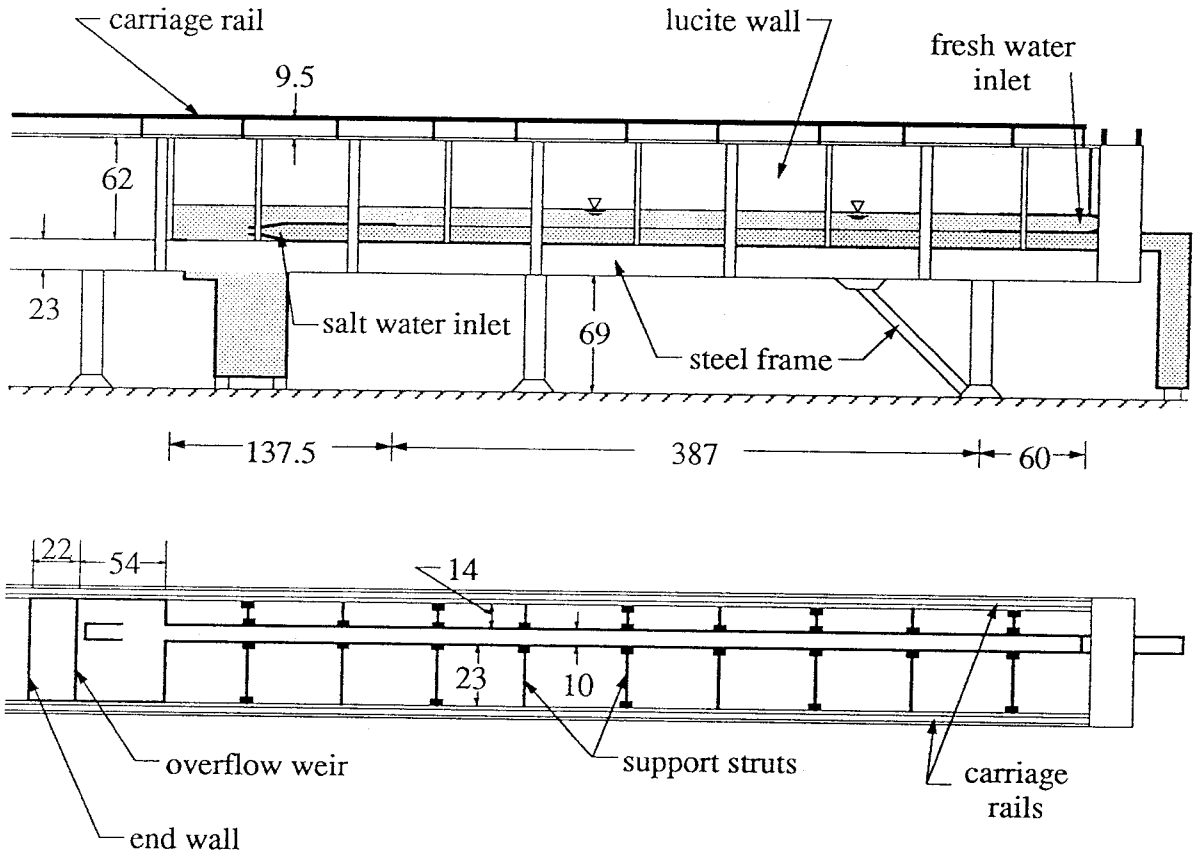

FIGURE 2.1.1. Schematic of two-layer flow facility. Side view is shown above and plan view below. All dimensions are in cm.

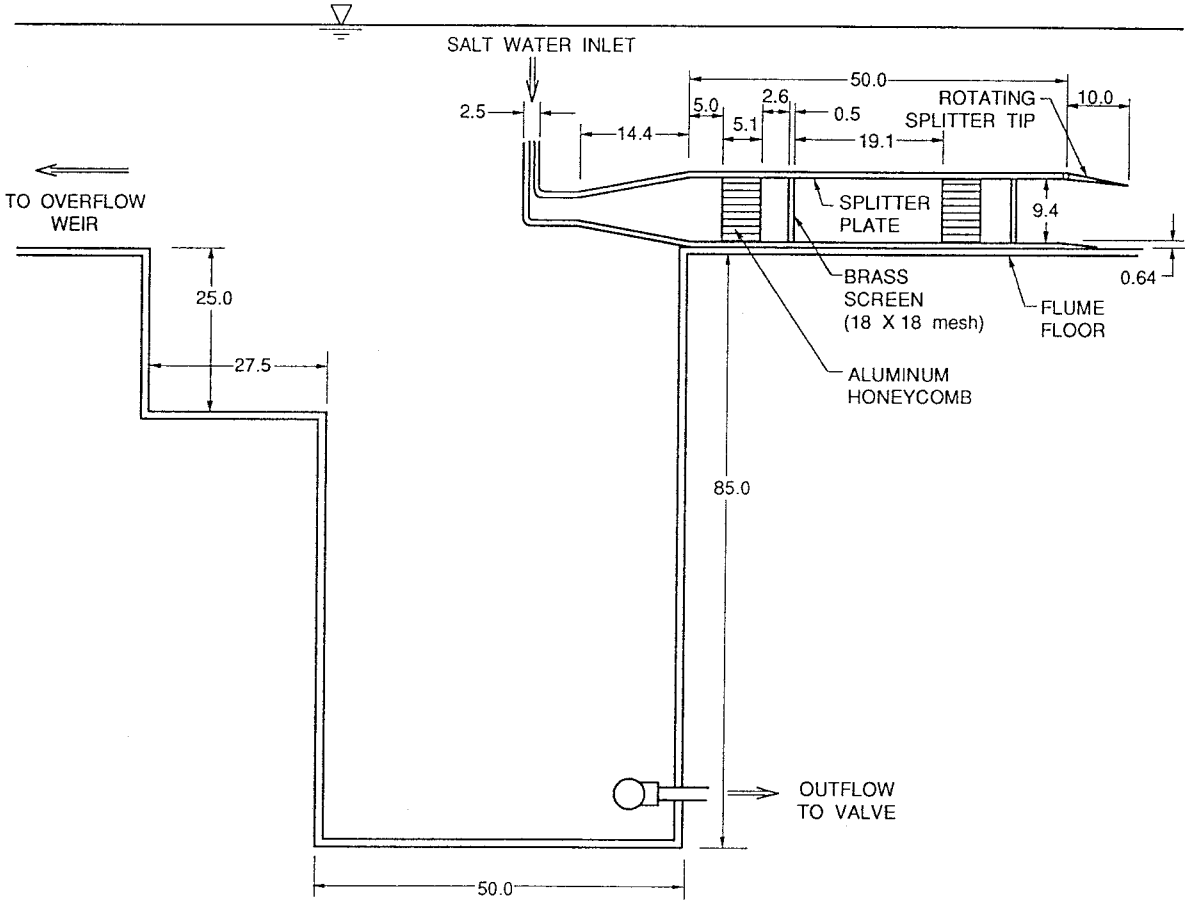

FIGURE 2.1.2. Salt-water inlet. All dimensions are in cm.

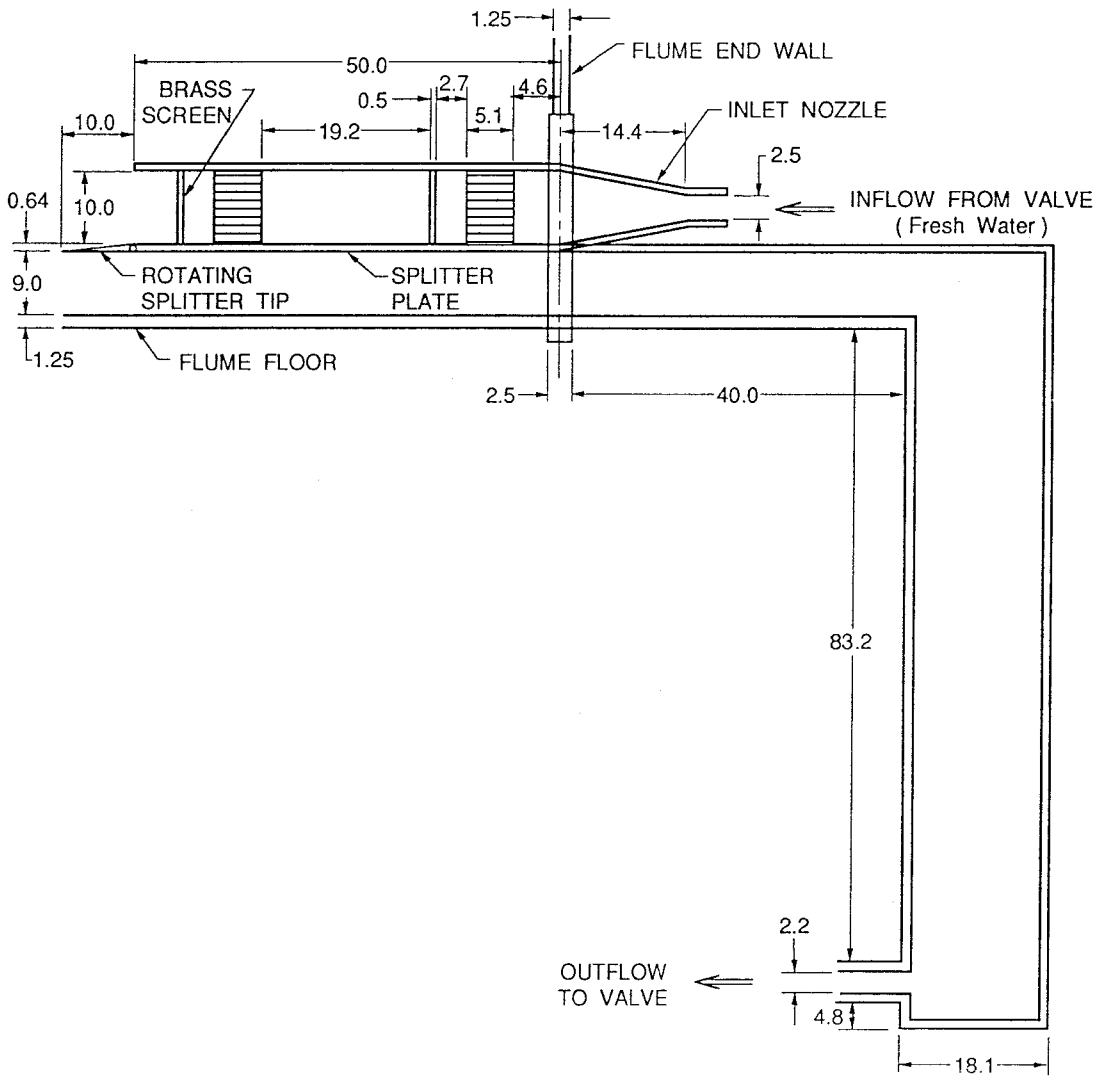

FIGURE 2.1.3. Fresh-water inlet. All dimensions are in cm.

The flume walls and floor are constructed of 1.27 cm thick Lucite. The side walls are supported by lateral struts which keep lateral deflections below 1%. The flume itself rests on a series of support bars spaced 20 to 30 cm apart. The support bars have dimensions 2.5 cm x 17.8 cm x 0.6 cm and are each supported by two adjustable brass screws, raising them slightly above a steel platform of width 60 cm. The brass screws enable the flume to be levelled to within 1.5 mm over 2 m. Precision rails run along the top of the flume parallel to the side walls to support an instrument carriage.

A series of irregular rock is packed on the flume floor to within approximately 10 cm of each inlet. The rocks are approximately ellipsoidal with average major and minor diameters 1.8 cm and 1.0 cm, respectively, resulting in an average roughness height of approximately 0.75 cm. The original purpose of the lower wall roughness was to study effects of externally generated turbulence at the interface. However, the relative importance of this was found negligible in the cases studied, and further attempts to alter the roughness were not made.

A schematic diagram of the flow generation system is shown in figure 2.1.4. NaCl and filtered lab water are mixed in a 1300 L tank by means of a bubble plume emanating from the mixing tank floor. Ethanol and filtered lab water are mixed in a 1000 L tank using the method developed by Hannoun (1985) to match the index of refraction of the saline solution. The saline solution is pumped up from the 1300 L tank by a 1/3 HP pump through 1.9 cm diameter Tygon tubing to a constant head tank approximately 5 m above the flume floor. The saline solution flows from there through a valve and a precision flowmeter (F. & P. Co.) before entering the flume, as shown in figure 2.1.2. The alcohol-water solution is pumped up to a second constant head

tank, and flows through a valve and flowmeter before entering the fresh-water inlet, as shown in figure 2.1.3.

A two-layer counterflow is thus established in the flume, with ethanol-water solution flowing above index of refraction matched saline solution. The fluids exit the flume by either passing through the outlets shown in figures 2.1.2 and 2.1.3, or by flowing over the sharp-crested overflow weir which maintains a constant total depth of fluid.

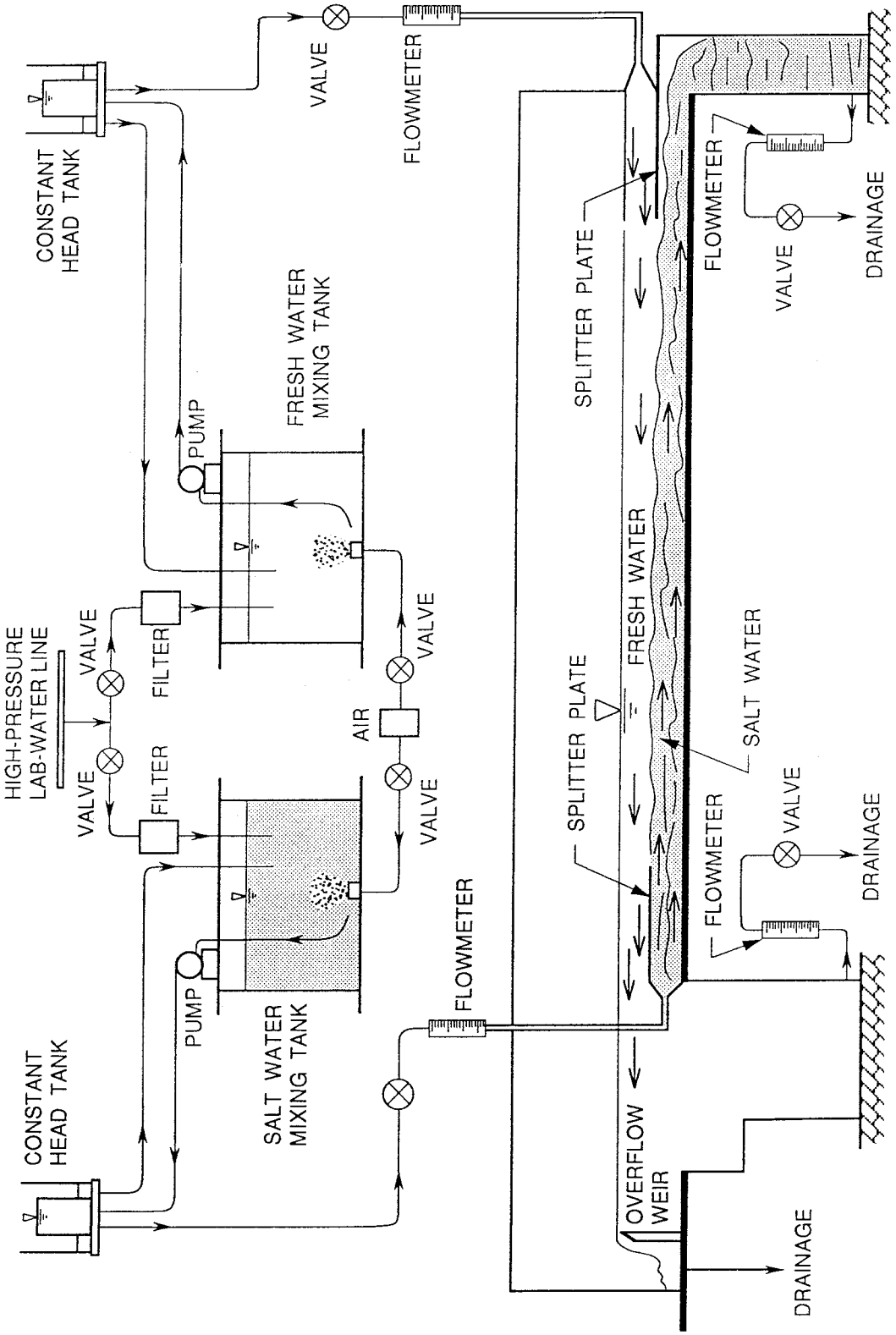

FIGURE 2.1.4. Schematic of flow generation system.

2.2. Laser-Based Diagnostics

2.2.1. LDV Operations

In this section details pertaining to the design and operation of the laboratory's two-component, reference-beam laser-Doppler velocimeter (LDV) are discussed. These include: fundamentals of Doppler frequency shifting and reference beam heterodyning, the configuration of the optical and signal processing equipment, the laser beam geometry, and errors inherent in the measurement technique. For further details concerning laser-Doppler velocimetry, see the comprehensive texts by Durst *et al.* (1981) and Drain (1980).

A laser-Doppler velocimeter essentially measures the Doppler frequency shift of light scattered by particles moving in the fluid. A schematic of light scattering by a particle is shown in figure 2.2.1.1. Here a monochromatic light source at point S emits light in the direction $\hat{\mathbf{e}}_1$ which is scattered by a particle, moving with velocity $\mathbf{u}$, from P toward an observer at O. The frequency of the light observed by the particle is

$$f_1 = f_0(1 - n\mathbf{u}\cdot\hat{\mathbf{e}}_1 / c),$$

where $\hat{\mathbf{e}}_1$ is a unit vector in the direction from S to P, f_0 is the frequency of the light in the source frame of reference, c is the speed of light in a vacuum, and n is the index of refraction of the medium in which the light propagates. The scattered light observed at O is of frequency

$$f_2 = f_1(1 - n\mathbf{u}\cdot\hat{\mathbf{e}}_2 / c)^{-1},$$

where $\hat{\mathbf{e}}_2$ is a unit vector in the direction from P to O. To order $(1/c)^2$,

$$f_2 = f_0(1 + n\mathbf{u}\cdot(\hat{\mathbf{e}}_2 - \hat{\mathbf{e}}_1) / c),$$

which may be written as $f_2=f_0+f_D$, where

$$f_D = \frac{2nU\sin(\theta/2)}{\lambda} \qquad (2.2.1.1)$$

is the Doppler frequency shift (Durst *et al.* 1981). Here U is the component of **u** in the direction normal to the bisectrice of $\hat{\mathbf{e}}_1$ and $\hat{\mathbf{e}}_2$ (as shown), θ is the angle between $\hat{\mathbf{e}}_1$ and $\hat{\mathbf{e}}_2$, and λ is the wavelength of the light in a vacuum.

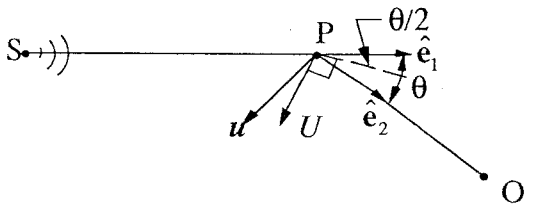

FIGURE 2.2.1.1. Geometry of light scattering by a moving particle.

In order to measure the Doppler frequency shift, two beams are heterodyned on a photodetector. If the scattered beam has electric field†

$$E_S = E_2(t)\cos(2\pi f_2 t + \phi_2),$$

† It is assumed that the light is linearly polarized; the electric field is thus treated as a scalar quantity.

and the reference beam has electric field

$$E_r = E_0 \cos(2\pi f_0 t + \phi_0),$$

then the output current is given by

$$i(t) \sim [E_0 \cos(2\pi f_0 t + \phi_0) + E_2(t) \cos(2\pi f_2 t + \phi_2)]^2$$

(Drain 1980).† Neglecting terms of high optical frequency (to which the photodetector cannot respond) this yields

$$i(t) \sim 1/2[E_0^2 + E_2^2(t)] + E_0 E_2(t) \cos[2\pi(f_0 - f_2)t + \phi_0 - \phi_2]. \qquad (2.2.1.2)$$

Hence the Doppler frequency shift may be determined by measuring the frequency of the second term in the RHS of (2.2.1.2).

The laboratory's LDV employs 2 reference beams and one scattering beam, arranged to measure the vertical and streamwise components of velocity. A brief description of the optical components used to generate the beams now follows.

Coherent, linearly polarized light of nominal power 15 mW and wavelength 632.8 nm exits the laser (Hughes model 3227H-PC), as shown in figure 2.2.1.2. The beam diameter at the exit is 0.8 mm (nominal, measured at the $1/e^2$ points) with divergence 1.1 mrad. The beam passes through a beam splitter which splits it into a reference beam (~ 5% power) and a scattering beam (~ 90% power). Each beam is then frequency shifted by approximately 40 MHz by passing through a Bragg cell (Coherent model 305, powered by Electronic Navigation Industries' model 300 LRF broad-band power amplifier). The frequencies of the scattering and reference beams are reduced by approximately 41.2028 MHz and 41.1141 MHz, respectively, resulting

† The sign ~ is used here to denote proportionality.

in a relative shift of approximately 88.7 KHz, the frequency of the reference beam being greater. (This is done to facilitate directional discrimination.) The reference beam then passes through a polarizing beam splitter cube which divides it into two beams of nearly equal power. The downward reflected beam is reflected through two 90° prisms, making it approximately parallel to the companion beam. Both reference beams then pass through 1° wedge prisms, making them approximately parallel to the scattering beam. At this point the polarization vectors of all three beams are aligned. (The scattering beam has passed through a half-wave plate.) The beams are then reflected through a front surface mirror and pass through a 400 mm focal length achromatic doublet, which focuses them at the center (spanwise) of the flume.

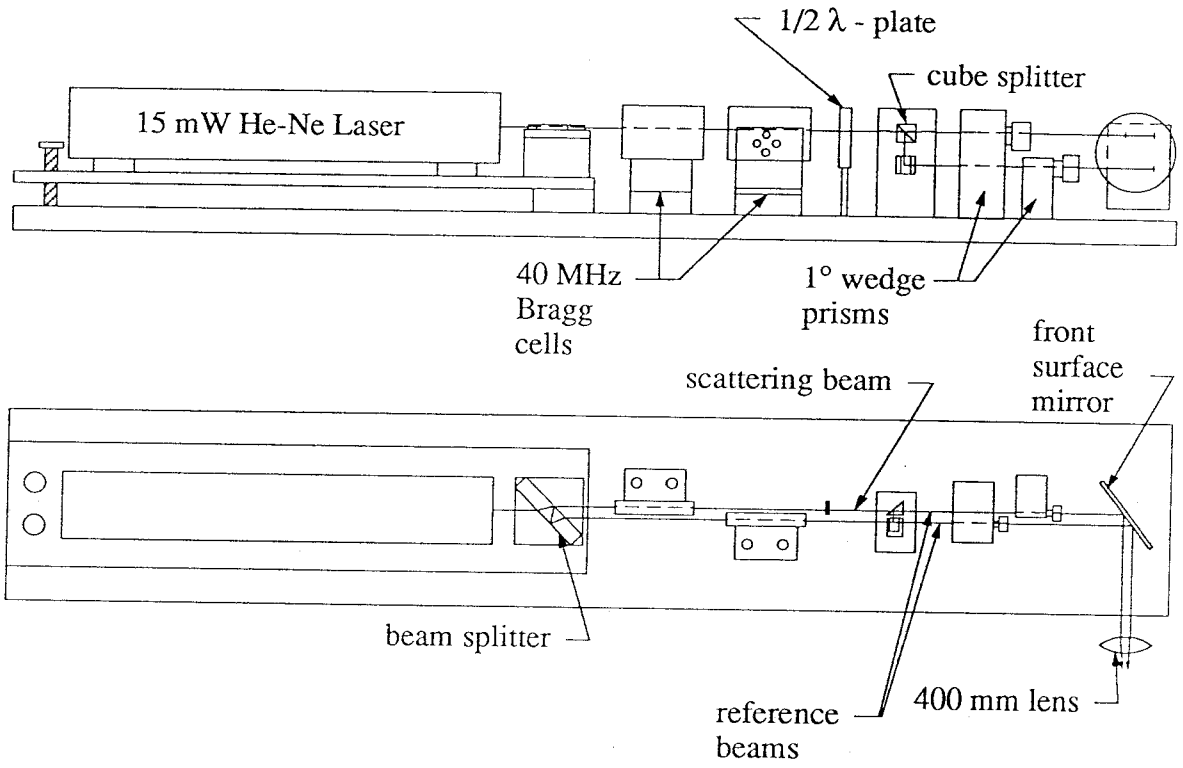

FIGURE 2.2.1.2. LDV transmitting optics. Side view is shown above and plan view below.

After passing through the flume, each reference beam is reflected by a front-surface mirror and passes through a 125 mm focal length plano-convex lens. From there each beam is focussed onto a 0.20 mm diameter pinhole, placed just in front of a fast-response silicon photodiode (EG&G model DT-25), as shown below.

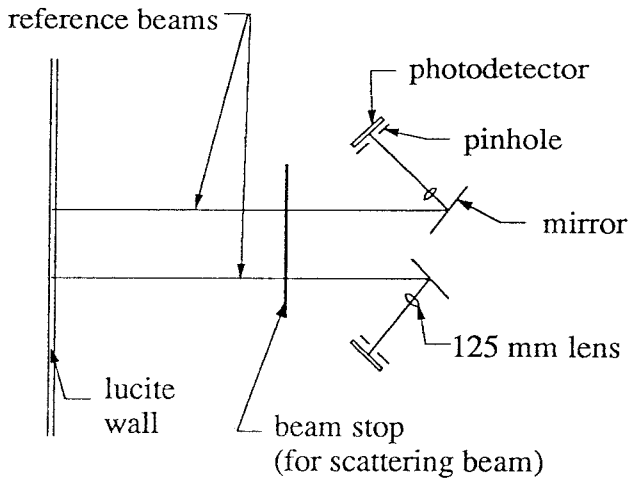

FIGURE 2.2.1.3. LDV receiving optics.

The transmitting and receiving optics are mounted on an instrument carriage designed by Rasi (1989). Figure 2.2.1.4 and 2.2.1.5 show, respectively, views of the carriage looking down the channel and from above. The transmitting and receiving optics' platforms move as a unit so that the entire depth of fluid (except very close to the floor or free surface) can be surveyed. The carriage is supported by roller bearings resting on precision rails extending the length of the flume, so the laser instrumentation can be moved to any position in the flume with relative ease. For further details pertaining to the instrument carriage see Rasi (1989).

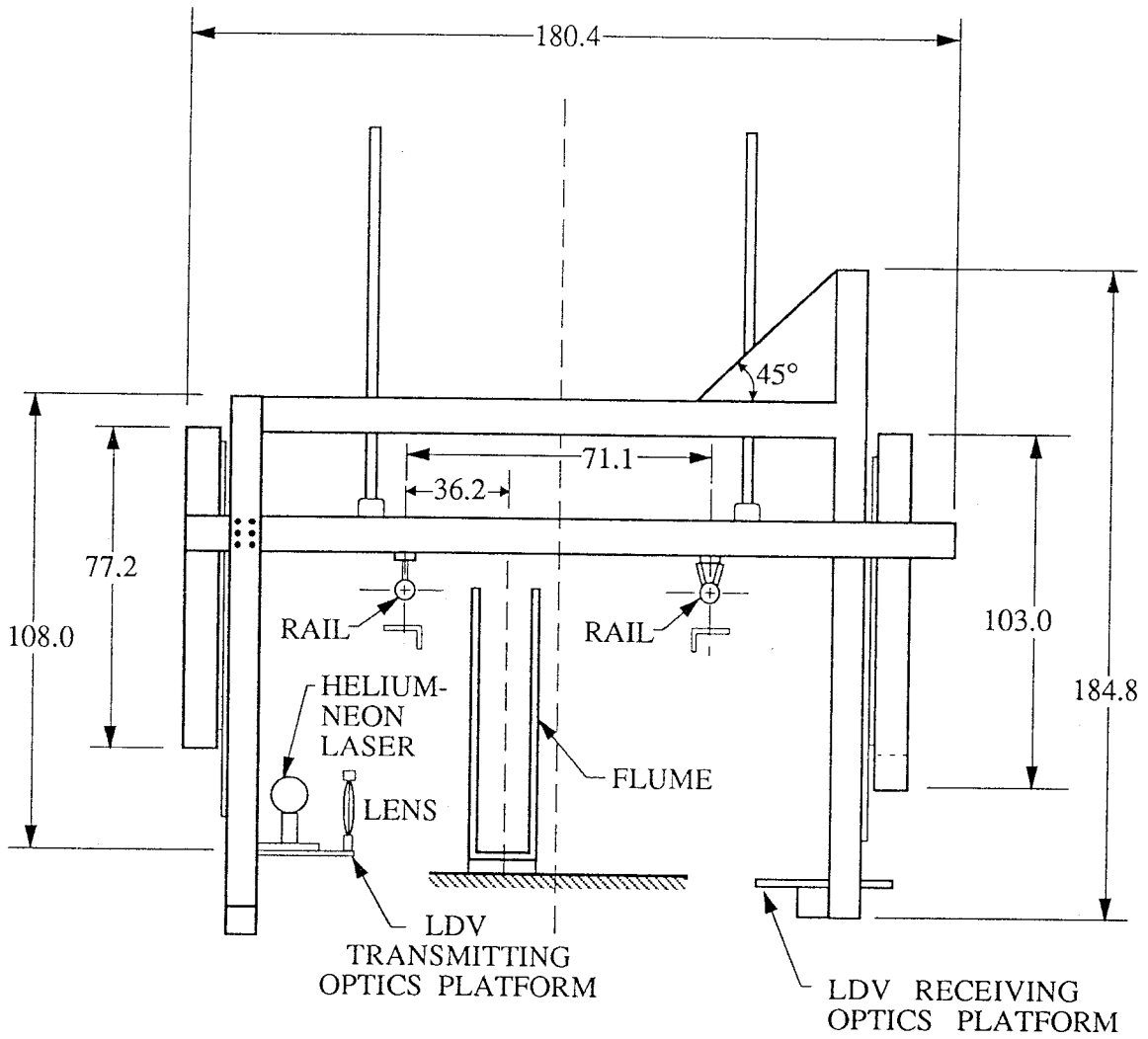

FIGURE 2.2.1.4. Instrument carriage: elevation.

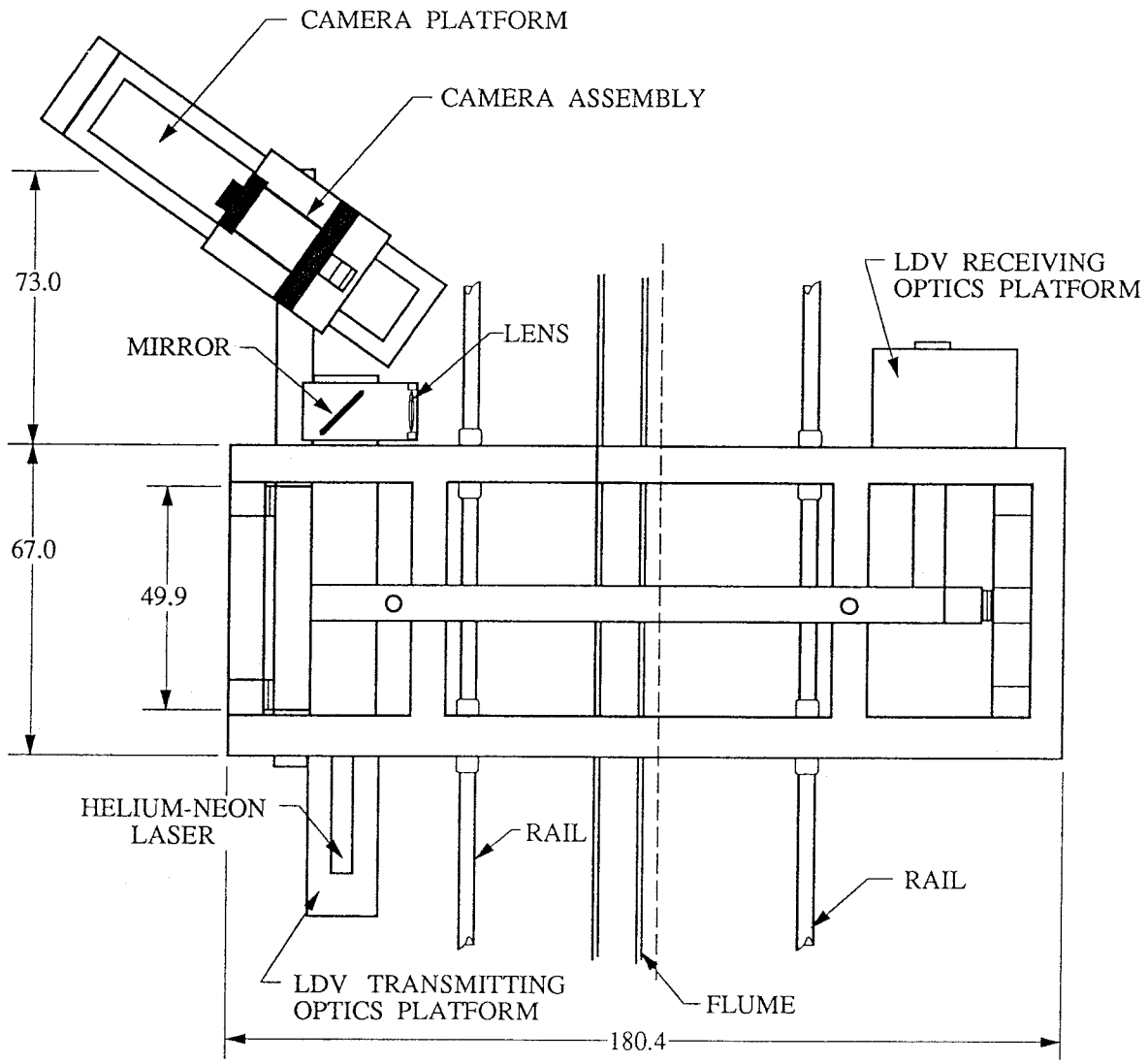

FIGURE 2.2.1.5. Instrument carriage: plan view.

Each of the signals from the silicon photodiodes is processed using a zero crossings-counter type signal processor (designed by Gartrell 1978), shown schematically in figure 2.2.1.6. An overview of the system now follows.

The pre-amplified signal from the photodiode is sent to the signal processor where it is further amplified and band-pass filtered using fourth-order Butterworth filters (Krohn-Hite model 3202). The lower and upper cut-off frequencies are 70 and 110 KHz, respectively, for the horizontal signal and 84 and 100 KHz, respectively, for the vertical signal. The filtered signal is then sent to the crossings counter, which measures the time taken for 24 zero crossings of the input signal. If 24 crossings are successfully timed while the signal is above a threshold (set externally), then the output from the timer is sent to the D/A converter.† The analog output from the D/A converter is then amplified, offset, and low-pass filtered using a fourth-order Butterworth filter (Krohn-Hite model 3202R). The cut-off frequency is set at 40 Hz to avoid aliasing of the discretely sampled signal. The amplification and offset are set to exploit as much of the range (-5V,+5V) of the Masscomp AD12FA A/D converter as possible, while ensuring that the output signal is not clipped. Finally, the filtered signal is sampled by the A/D converter and stored on the Masscomp 5450 disk. For further details of the processor logic see Gartrell (1977).

† The time between updates from the crossings counter is typically in the range 2-5 ms. This effectively sets an upper bound on the LDV sampling frequency.

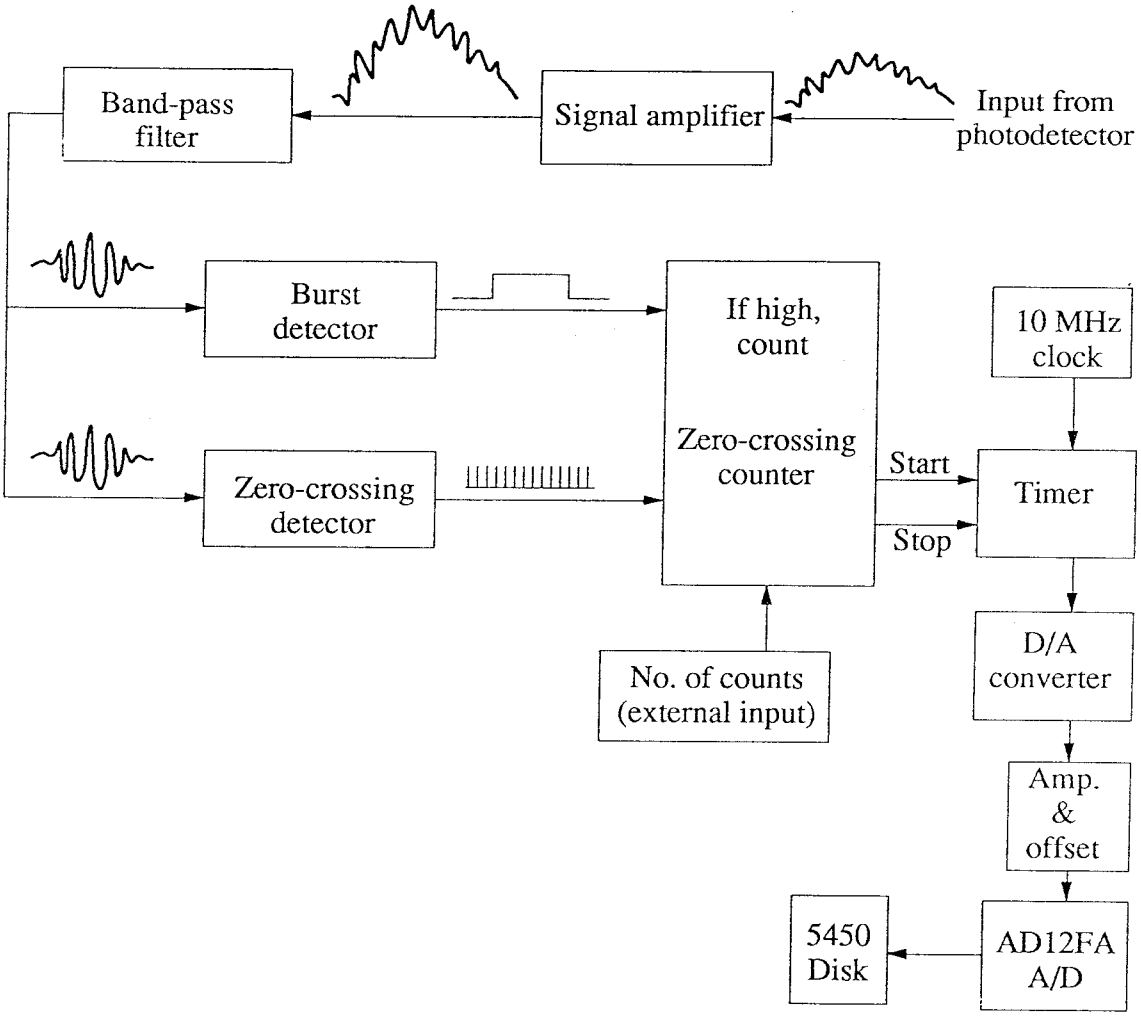

FIGURE 2.2.1.6. Schematic of the LDV signal processor.

The output voltage from the signal processor is related to the input signal frequency by

$$V=A+B/f_m, \qquad (2.2.1.3)$$

where f_m is the measured input signal frequency, V is the output voltage, and A and B are calibration coefficients. To determine A and B the signal processor is calibrated immediately before and after an experiment using a pure sine wave input from a signal generator. Ten input signals are used to calibrate the system, spanning the range of expected input signal frequencies. Typical values of A and B are 43.985 Volts and 3830.215 KHz-Volts, respectively, for the horizontal signal and 74.976 Volts and 6651.226 KHz-Volts, respectively, for the vertical signal. Variations in the calibration coefficients over the course of an experiment are found negligible.

In order to determine the velocity components three pairs of angles must be measured. First, the angles between the bisectrices of the reference beam-scattering beam pairs and the normal to the flume wall, θ_{off}, are measured (see figure 2.2.1.7). In all cases these are negligibly small (approximately 0.16 deg and 0.03 deg for the vertical and horizontal beams, respectively), so it may be assumed that the bisectrices are effectively normal to the flume wall. Second, the angles between the reference beams and the scattering beam are determined using the relation

$$\tan\theta = \frac{w_2 - w_1}{n_{fluid} L},$$

where w_1, w_2, and L are as shown in figure 2.2.1.7. Finally, the angles γ and β are measured (see figure 2.2.1.8). Here γ is the angle between the plane containing the vertical reference beam and the scattering beam and the plane normal to the flume

sidewall. β is the angle between the plane containing the horizontal reference beam and the scattering beam and the plane parallel to the flume floor.

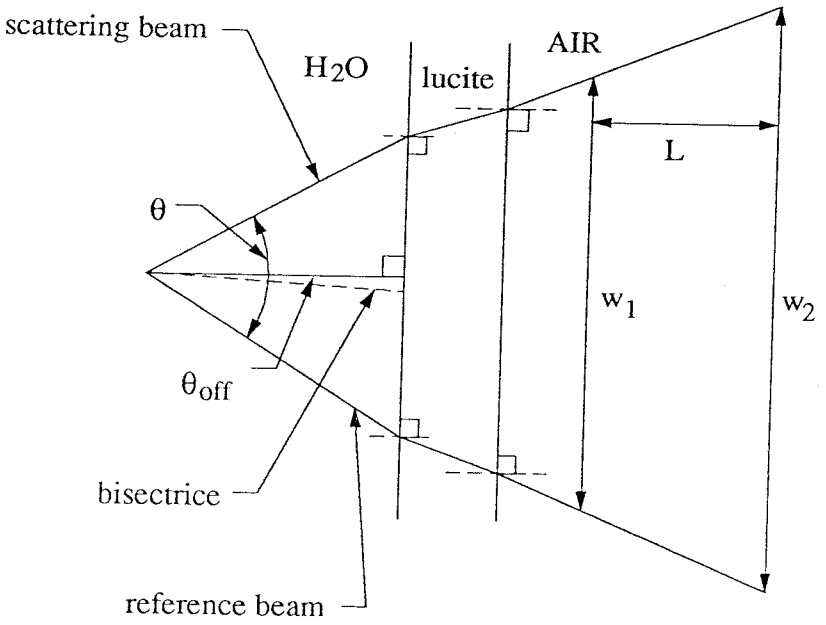

FIGURE 2.2.1.7. Laser beam geometry.

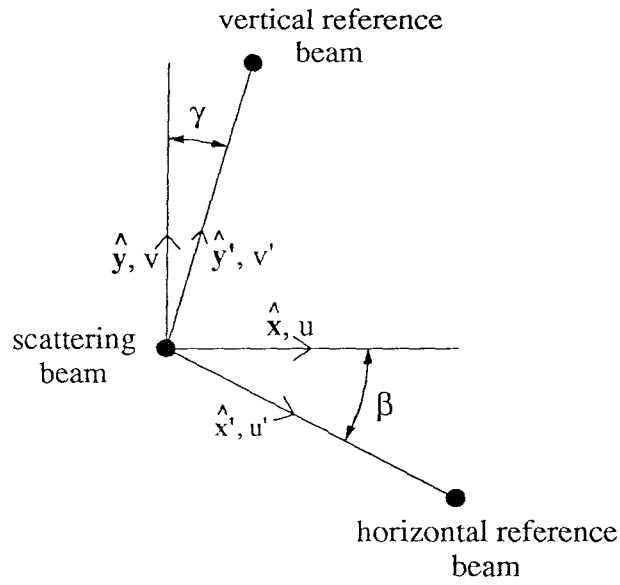

FIGURE 2.2.1.8. Scattering and reference beam positions.

Using measured values of θ_u (horizontal) and θ_v (vertical), estimates of the major and minor diameters, a and b, of the approximately ellipsoidal focal volume are made, using formulas from Durst *et al.* (1981). The focal volume effectively defines the (static) spatial resolution of the measurements. Values of a and b are given in table 2.2.1.1, along with values of θ, γ, β, and k', where f_D=k'U.

Velocities in the $\hat{\mathbf{x}}'$ and $\hat{\mathbf{y}}'$ directions (see figure 2.2.1.8) are determined using (2.2.1.1). Velocities in the $\hat{\mathbf{x}}$ (streamwise) and $\hat{\mathbf{y}}$ (vertical) directions are given by

$$u = \frac{u'\cos\gamma + v'\sin\beta}{[\cos\beta\cos\gamma + \sin\beta\sin\gamma]}, \tag{2.2.1.4}$$

and

$$v = \frac{-u'\sin\gamma + v'\cos\beta}{[\cos\beta\cos\gamma + \sin\beta\sin\gamma]}, \tag{2.2.1.5}$$

respectively, where

$$u' = \frac{\lambda f_{D_u}}{2n\sin(\theta_u/2)}, \tag{2.2.1.6}$$

and

$$v' = \frac{\lambda f_{D_v}}{2n\sin(\theta_v/2)}. \tag{2.2.1.7}$$

Note that f_D=F-f_m, where f_m is the frequency measured by the signal processor, and F is the relative frequency shift between the scattering and reference beams (due to the Bragg cell shift). Values of F are given in table 2.2.1.1.

	Experiment 1 and 4	Experiment 10 and 11	Experiment 13
θ_u (deg)	1.70	1.69	1.70
θ_v (deg)	1.89	1.90	1.89
γ (deg)	-1.36	-1.23	-0.94
β (deg)	0.82	0.70	1.14
F (KHz)	88.74	88.74	88.74
k'_u (Hz/cm/s)	625.1	621.5	625.1
k'_v (Hz/cm/s)	695.0	698.7	695.0
a_u (mm)	13.2	13.3	13.2
b_u (mm)	0.20	0.20	0.20
a_v (mm)	11.9	11.8	11.9
b_v (mm)	0.20	0.20	0.20

TABLE 2.2.1.1. LDV parameters.

Finally, errors associated with the measurement of u and v are estimated. It is first noted that LDV measures the velocity of particles in the fluid, not the velocity of fluid particles themselves. For small scattering particles it can be shown (Drain 1980) that particles essentially act as single-pole, low-pass filters to fluctuations in the fluid velocity with cut-off frequency

$$f_c = \frac{9\mu}{4\pi\rho_p a_p{}^2}. \qquad (2.2.1.8)$$

Here μ is the fluid viscosity, ρ_p is the particle density, and a_p is the radius of the (assumed) spherical particle. It is found that there are effectively no particles larger than about 5 μm (in radius) in the lab water (Gartrell 1979); the effective cut-off frequency is then about 30 KHz. This is much larger than any frequency resolvable by the LDV, so particle size poses no extra limitations on the system.

Using (2.2.1.1) and (2.2.1.4) to (2.2.1.7), and assuming θ, γ and β are small, the velocity components may be written as

$$u = \frac{\lambda(F - f_{m_u})}{n\theta_u} + \frac{\beta\lambda(F - f_{m_v})}{n\theta_v}, \qquad (2.2.1.9)$$

and

$$v = \frac{\lambda(F - f_{m_v})}{n\theta_v} - \frac{\gamma\lambda(F - f_{m_u})}{n\theta_u}. \qquad (2.2.1.10)$$

Hence errors in F, θ, γ, β, and f_m all contribute to the total error in u and v. Typical values of F, θ, γ, β, and f_m and their associated errors are given in table 2.2.1.2. The most important of these is the error in f_m, made up of three components: (1) ambiguity

in D/A conversion, (2) ambiguity in A/D conversion, and (3) noise on the input signal,† causing either an excess (high frequency noise) or deficiency (low frequency noise) of zero-crossings counted. For further details pertaining to these errors see Gartrell (1979).

Parameter	Typical value	Error	Units
F	88.74	0.02	KHz
θ_u	1.69	0.04	deg
θ_v	1.90	0.04	deg
γ	-1.23	0.25	deg
β	0.70	0.25	deg
f_m (horizontal)	85.63	(1) 0.02	KHz
		(2) 0.005	KHz
		(3) 0.131††	KHz
f_m (vertical)	88.67	(1) 0.02	KHz
		(2) 0.005	KHz
		(3) 0.070	KHz

TABLE 2.2.1.2. LDV parameter errors.

† The error due to (3) may be estimated by taking measurements in quiescent fluid.

†† This value (and that for the vertical component) varies by as much as 50%. The variation is due to changes in the signal quality with location in the flume.

For small θ, γ, and β, the difference between the measured value of u and its true value is given approximately as

$$\Delta u = \frac{\Delta f_{m_u}}{F - f_{m_u}} u + \frac{\Delta F}{F - f_{m_u}} u + \frac{\Delta \theta_u}{\theta_u} u + \Delta \beta v, \qquad (2.2.1.11)$$

and similarly for the vertical component

$$\Delta v = \frac{\Delta f_{m_v}}{F - f_{m_v}} v + \frac{\Delta F}{F - f_{m_v}} v + \frac{\Delta \theta_v}{\theta_v} v + \Delta \gamma u. \qquad (2.2.1.12)$$

It should be noted that ΔF, $\Delta\theta$, $\Delta\gamma$, and $\Delta\beta$ are fixed for a given experiment, while Δf_m is a random process.

Assuming that terms on the RHS of (2.2.1.11) and (2.2.1.12) are approximately independent Gaussian random variables, estimates of the standard deviations† of Δu and Δv may be made. This has been done for five different velocities and the results are given in table 2.2.1.3. It should be noted that these are *absolute* errors in *individual* measurements.

Of greater interest are errors†† in statistical quantities such as the sample mean and variance. The sample mean is given by

$$\bar{u} = \frac{1}{N} \sum_{i=1}^{N} u_i, \qquad (2.2.1.13)$$

where u_i is the i^{th} measured value of u, so the relative error in $\bar{u}$, for large N, is given approximately by

---

† The error in a single measurement of u is defined here as the standard deviation of Δu.

†† Errors discussed here are solely due to instrumentation effects; effects of finite sampling rate and sampling time on the convergence of estimates of statistical quantities are presented in §3.2.

$$\frac{\Delta\bar{u}}{\bar{u}} = A + B\frac{\bar{v}}{\bar{u}}, \qquad (2.2.1.14)$$

where

$$A = \frac{\Delta F}{(F - \bar{f}_m)} + \frac{\Delta\theta}{\theta},$$

and

$$B = \Delta\beta.$$

with similar results holding for $\bar{v}$.

The sample variance is given by

$$\sigma_u^2 = \frac{1}{N-1}\sum_{i=1}^{N}(u_i - \bar{u})^2, \qquad (2.2.1.15)$$

and typically the majority of the error in this arises from the first term in the RHS of (2.2.1.11). The expected value of the error is always positive and hence measured values of σ_u^2 are always greater than the true values. The error in σ_u^2 , for large N, is given approximately by

$$\Delta\sigma_u^2 = \left[\frac{\Delta f_{m_u}\lambda}{n\theta_u}\right]^2, \qquad (2.2.1.16)$$

with similar results holding for σ_v^2. Estimates of the errors in $\bar{u}$, $\bar{v}$, σ_u^2, and σ_v^2 are given in table 2.2.1.3.

	Error in:				Error in:		
$\overline{u}$ (cm/s)	u_i (cm/s)	$\overline{u}$ (cm/s)	σ_u^2 (cm^2/s^2)	$\overline{v}$ (cm/s)	v_i (cm/s)	$\overline{v}$ (cm/s)	σ_v^2 (cm^2/s^2)
1.0	0.21	0.04	0.045	0.1	0.10	0.03	0.010
3.0	0.22	0.08	0.045	0.3	0.11	0.03	0.010
5.0	0.24	0.13	0.045	0.5	0.11	0.04	0.010
7.0	0.27	0.17	0.045	0.7	0.11	0.04	0.010
10.0	0.32	0.25	0.045	1.0	0.11	0.06	0.010

TABLE 2.2.1.3. Estimates of the errors in instantaneous velocity, mean velocity and velocity variance.

2.2.2. LIF Operations

Laser-induced fluorescence (LIF), a quantitative measurement technique developed over the last 15 years, is employed in this study to investigate local mixing and transport between two streams of fluid. This technique essentially consists of exciting a fluorescent dye with a high powered laser, and measuring the intensity of the resulting fluorescence. The dye is pre-mixed with some fraction of fluid in the flow, and from measurements of the fluorescent light intensity, the scalar dye concentration may be determined. The LIF method has many attributes: it is non-intrusive, high-resolution (both spatially and temporally), and provides detailed information about the spatial structure of the flow. For further details about the history of LIF, see Papantoniou (1989).

The method employed successfully by Koochesfahani (1984), Papantoniou (1985) and more recently by Hannoun (1987) and Rasi (1989) is used in this work. A linear photodiode array is used in conjunction with an Argon-Ion laser to measure the spatial distribution of scalar concentration along a vertical line through the flow. Rhodamine 6G dye, pre-mixed with the lower layer fluid, acts as the tracer. When excited by laser light of wavelength 514.5 nm (green line) the dye emits light of wavelength approximately 570 nm (yellow). The fluoresced light is focussed onto an array of light-sensitive photo-diodes, and by sampling the photo-diode array rapidly in succession, detailed information about fluid mixing and transport at the interface may be obtained.

A schematic of the optical layout is shown in figure 2.2.2.1. Laser light of wavelength 514.5 nm, diameter 1.25 mm (at $1/e^2$ points) and divergence 0.69 mrad, exits the 2W Argon-Ion laser (Spectra Physics model 265). The TEM_{00} mode is selected so that the beam intensity is approximately Gaussian in the radial direction.

The laser is operated in the light-stabilized mode, maintaining a constant power output to within 2%. The beam is reflected through a series of front surface mirrors, passes through a beam reducer (100 mm and 20 mm focal length plano-convex lenses separated by the sum of their focal lengths), and is focussed to a waist near the two-fluid interface by an 800 mm focal length plano-convex lens. In order to avoid beam wobbling due to free surface waves, the beam passes through a thin Lucite window at the free surface.

The diameter of the beam at the focus effectively defines the spanwise spatial resolution of the measurements, while the confocal parameter (defined as the distance between the points at which the laser diameter is greater than that at the waist by a factor of $\sqrt{2}$), effectively defines the useful imaging section of the laser beam. Values of these are given in table 2.2.2.1, along with values of the unattenuated laser beam power, I_0, the dye attenuation coefficient, εC_0, and the vertical and longitudinal (static) spatial resolutions. (The Guassian beam formulas used in these estimates are taken from Siegman 1986.)

Experiment	I_0 (W)	εC_0 (m^{-1})	Beam waist (μm)	Confocal parameter (cm)	Spatial resolution (width x height) (μm x μm)
1	0.65	0.71	420	53.9	314 x 302
4	0.70	0.87	420	53.9	318 x 305
10	0.70	1.06	320	31.2	318 x 305
11	0.70	1.10	320	31.2	318 x 305
13	0.70	0.91	374	42.6	316 x 304

TABLE 2.2.2.1. LIF parameters.

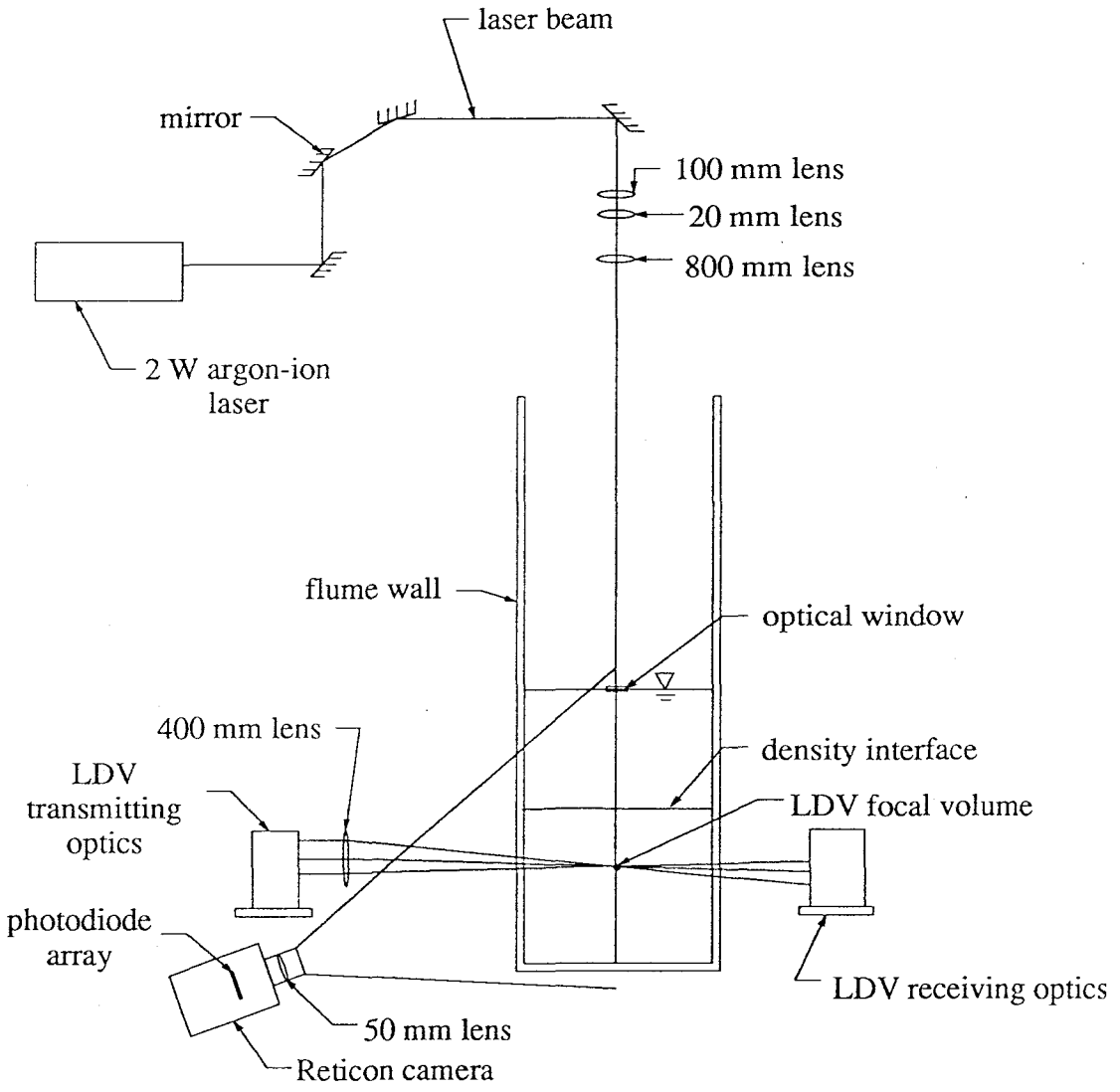

FIGURE 2.2.2.1. Schematic of LDV and LIF optical layouts.

To measure the intensity of fluoresced light, a section of the laser beam (always smaller than the confocal parameter) is focussed by a 50 mm f1.8 Nikon lens onto an array of 1024 light sensitive photodiodes (Reticon RL-1024 G), housed in a camera (EG & G Reticon LC 300A). An optical filter is placed in front of the lens which acts to block the green laser light and pass the yellow fluoresced light. The field of view of the optical system is determined by the distance from the camera lens to the laser beam, typically between 63 and 66 cm. Resulting values of (static) spatial resolution are given in table 2.2.2.1.

The LC 300A camera operates in much the same way as an ordinary camera with the photodiode array replacing the film. The photodiodes are in a single row with center-to-center spacing of 25 μm and aperture width 26 μm. Details of the electronic circuitry are given in the Reticon LC 300A manual (1981). The frequency of scan of the photodiodes (controlled by the computer clock) effectively defines the temporal resolution of the measurements, given in table 2.2.3.1.

The camera is mounted in a custom built assembly, designed to accurately align the array with the laser beam. The assembly consists of a gimbal mirror mount (Newport model 6520-6) and a precision rotation stage (Newport model 471-A) connected via an outer casing (see figure 2.2.2.2). The camera is positioned in the assembly with the array at the gimbal point so the array can be accurately aligned with the laser beam and a sharp focus can be achieved.

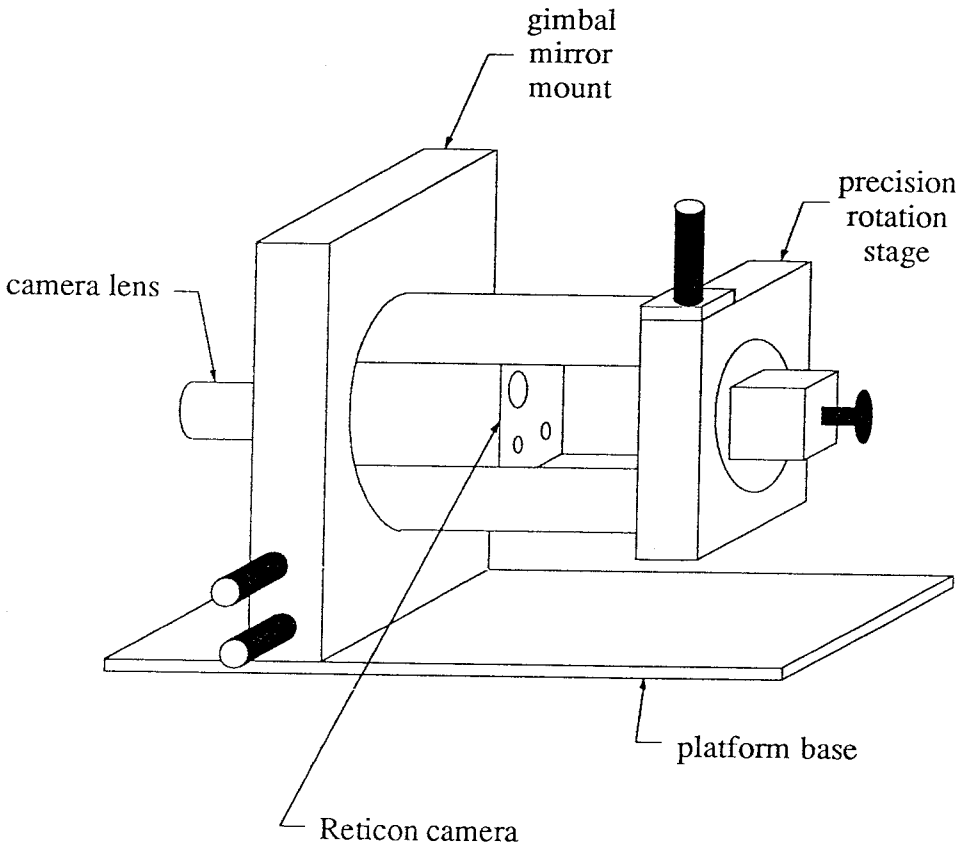

FIGURE 2.2.2.2. LIF camera assembly.

In practice, a thin Lucite sheet lined with dark horizontal bands spaced at 2.5 cm intervals is used to focus the beam onto the array. The sheet is placed just in front of the laser beam, and the array is aligned so that the drop in intensity near the uppermost and lowermost bands is as sharp as possible. The sheet is also used to measure the magnification ratio of the imaging system, determined by the number of pixels between low intensity regions (corresponding to dark bands on the sheet).

Photodiode readings are converted to dye concentrations using a method similar to that developed by Koochesfahani (1984). The method involves the use of an optical transfer function which corrects for: variable beam width, pixel response non-uniformity, beam attenuation by the dye, non-uniformity of the imaging system, and slight array misalignment with the laser beam. Following Koochesfahani, the photodiode output may be written approximately as

$$V_i = I_0 H_i e^{\left(-\varepsilon \int_0^{\xi_i} C(y)dy\right)} C_i + D_i, \qquad (2.2.2.1)$$

where V_i is the output from the i^{th} photodiode, I_0 is the laser beam intensity at the laser exit, C_i is the dye concentration at the location ξ_i (measured from the uppermost edge of the imaged region), D_i is the dark response, and H_i is the optical transfer function. H_i depends on the pixel sensitivity, the field of view, the line scan time, the solid angle over which light is collected, the local beam width, and ε, the dye absorption coefficient.

Before each experiment, a calibration is performed with experimental run solution. The transfer function is determined by

$$H_i = \frac{V_{ci} - D_i}{I_c e^{-\varepsilon C_0 \xi_i} C_0}, \qquad (2.2.2.2)$$

where V_{ci} is the average reading from the i^{th} pixel, and C_0 is the (uniform) dye concentration. In the experimental run the measured dye concentration is then given by

$$\frac{C_i}{C_0} = \frac{I_c}{I_0}\left[\frac{V_i - D_i}{V_{ci} - D_i}\right] e^{(-\varepsilon C_0 \int_0^{\xi_i} [1 - \frac{C(y)}{C_0}]dy)}. \qquad (2.2.2.3)$$

Approximating the integral in (2.2.2.3) by the sum

$$\Delta y \sum_{j=1}^{i-1} [1 - \frac{C_j}{C_0}] \qquad (2.2.2.4)$$

yields

$$\frac{C_i}{C_0} = \frac{I_c}{I_0}\left[\frac{V_i - D_i}{V_{ci} - D_i}\right] e^{[-\varepsilon C_0 \Delta y \sum_{j=1}^{i-1} (1 - \frac{C_j}{C_0})]}. \qquad (2.2.2.5)$$

Note that ε only appears in the combination εC_0 in (2.2.2.5); hence only the product εC_0 need be determined.

This is done by taking measurements of beam intensity at the entrance and exit of a Lucite box first filled with experimental run solution of concentration C_0 and then with pure water. This is done for ten different input intensities and the results are averaged to reduce measurement errors. εC_0 is then determined by

$$\varepsilon C_0 = \frac{1}{L_b} \ln\left[\frac{I_1 I'_2}{I_2 I'_1}\right], \qquad (2.2.2.6)$$

where I_1 and I_2 are the laser beam intensities entering and exiting, respectively, the box of length L_b with dyed solution, and I'_1 and I'_2 are beam intensities entering and exiting the box with pure water. Measured values of εC_0 are given in table 2.2.2.1.

For small εC_0, 2.2.2.5 may be written approximately as

$$\frac{C_i}{C_0} \cong \frac{I_c}{I_0}\frac{V_i - D_i}{V_{ci} - D_i}\left[1 - \varepsilon C_0 \Delta y \sum_{j=1}^{i-1}(1 - \frac{C_j}{C_0})\right]. \qquad (2.2.2.7)$$

Since the dye concentrations used typically result in beam attenuations < 20%, the second term in the square brackets in (2.2.2.7) is small and measurements are relatively insensitive to errors in εC_0 and Δy. The main sources of error are laser power fluctuations and electronic noise associated with photodiode circuitry. If the fluid near the floor is unmixed, corrections may be made for laser power fluctuations by normalizing (on a scan by scan basis) by near floor readings.

To validate the calibration and conversion procedures and to investigate the overall accuracy of the measurement technique, a test is performed. The array is first calibrated with a homogeneous solution of known dye concentration, C_0. The flume is then drained and refilled with a homogeneous solution of concentration approximately $0.45C_0$. Measurements are then made with the weaker solution and the flume is flushed and refilled with pure water. A final series of scans is then recorded to determine the dark noise level.

The results from the test are as follows. The rms difference between the time averaged individual pixel readings and the overall spatial average is about 2.5%. This may be attributed to non-linearities in the measurement system and possible fluctuations in pixel sensitivity. The rms fluctuations about the time average for

individual pixels is found to be between 1% and 2%, which may be attributed to electronic noise and laser power fluctuations. The error in the spatially averaged (measured) concentration is about 6%, which is accounted for by a shift in the laser power between the calibration and the test run.

2.2.3. Data Acquisition

A Masscomp SLS-5450-01 (Scientific Laboratory) computer system is used to sample and store the LDV and LIF signals. This system is based on a 68020 CPU with a 20 MHz clock. A 12 bit A/D converter is employed in the data acquisition which samples at up to approximately 350 KHz when data is continuously stored on the 142 MB diskdrive. Data processing, after the initial acquisition, is performed on a VAX3200 workstation. Timing parameters used in the experiments are given in table 2.2.3.1.

LIF parameters:	
Sampling frequency (pixel to pixel) (Khz)	50
Blanking period following each scan (μs)	800
Total line scan time (ms)	21.28
No. of sequential scans - calibration	1024
No. of sequential scans - run conditions	5120
Total sampling time (run) (sec)	108.9
LDV parameters:	
Sampling frequency (each channel) (Hz)	100
No. of samples (each channel)	16384
Sampling time (sec)	163.8

TABLE 2.2.3.1. Timing parameters for data acquisition.

2.3. Experimental Procedure

Before any experiments are run, the flowmeters used to regulate the flow are calibrated. Calibration is done in situ, over the full meter range. All flowmeters are found to behave linearly, with volumetric flowrates given by $Q = a_f R + b_f$. Here Q is the volumetric flowrate, R is the flowmeter reading, and a_f and b_f are calibration coefficients, given in table 2.3.1.

Flowmeter	a_f (cm^3/s)	b_f (cm^3/s)
Saline in	6.39	93.4
Saline out	4.05	34.1
Alcohol-water in	3.92	36.9
Alcohol-water out	6.66	9.0

TABLE 2.3.1. Flowmeter calibration coefficients.

The procedural steps followed in performing an experiment are now outlined. First the run solutions are prepared. NaCl is mixed with filtered lab water in the 1300 L tank and ethanol is mixed with filtered lab water in the 1000 L tank. The indices of refraction are matched to within 0.00005 (to avoid laser beam wobbling) using the procedure of Hannoun (1985) and the temperatures are matched to within 0.1 deg C (using ice). Sodium sulfite is then added (approximately 4 mg/L) to de-chlorinate the solutions (preventing the annihilation of Rhodamine dye by chlorine). An accurately

measured amount of Rhodamine 6G dye is then added to the saline solution and bubble plumes are run through both solutions for about 24 hours to eliminate any inhomogeneities. Dye concentrations between about 0.5×10^{-7} and 1×10^{-7} molar are used which minimizes laser beam attenuation, while still providing adequate fluorescent light to exploit the full range of the Reticon array.

Before an experiment is started, the density difference between the ethanol-water solution and the saline solution is determined. (The bubble plumes are shut off at least one hour prior to this to allow time for the fluids to de-gas.) Two precision 25 ml gravity flasks are filled with saline solution and are weighed using a precision mass balance. The flasks are then re-filled with alcohol-water solution and are weighed again. The normalized density difference is then determined by

$$\frac{\Delta\rho}{\rho} = \frac{M_S - M_W}{M_W - M_f}. \tag{2.3.1}$$

Here M_S is the mass of the flask filled with saline solution, M_W is the mass of the flask filled with alcohol-water solution and M_f is the dry flask mass. The difference between the measured values of $\Delta\rho/\rho$ (using each flask) is typically less than 0.00005. Following this, the lenses, mirror and flume walls are cleaned and the flume is filled with saline solution to a depth of 20 cm.

Next, the LDV and LIF equipment are positioned and the LDV is calibrated. The Ar-Ion laser is aligned so that is intersects the LDV focal volume in the (spanwise) center of the flume. The LDV angles (discussed in §2.2.1) are then measured and the position of the flume floor on the LDV carriage scale is recorded. Next, the dye attenuation coefficient, εC_0, is measured, as discussed in §2.2.2. The Ar-Ion laser power is then increased to about 0.8 W (single-line) and is allowed to stabilize for about 2 hours. After this, the LDV level detector and amplifier gain are

adjusted to maximize the signal quality and the signal processor is calibrated (as discussed in §2.2.1).

Following this, the LIF system is focussed and calibrated. First the focussing sheet is positioned just in front of the Ar-Ion beam and the beam is focused onto the Reticon array, as discussed in §2.2.2. Next, a series of array scans is recorded to determine the magnification ratio of the imaging system (ratio of object height in the plane of focus to the imaged object height in the plane of the array). The focusing sheet is then removed and a slight flow of saline solution is generated. This is done to avoid photo-bleaching and thermal blooming effects during calibration, as discussed by Koochesfahani (1984). The unattenuated laser beam power is then measured with a laser power meter (Newport model 815). Finally, a series of 1024 scans are recorded to determine the optical transfer function, as discussed in §2.2.2.

Following the LIF calibration, the experiment begins. Saline solution is drawn from the flume until the total depth of fluid is approximately 10 cm and ethanol-water solution is then slowly added until the total depth is 20 cm. The inlet and outlet flowrates of saline solution and alcohol-water solution are then slowly increased to their predetermined levels (chosen as discussed in §3.4) and the flow is allowed to equilibrate for 10 to 15 minutes. Typically the mean vertical position of the interface at positions along the flume is stationary after only a couple of minutes; 10 to 15 minutes are allowed for any small-scale imbalances to be rectified.

Once equilibrium is achieved, a series of 5120 LIF array scans are recorded. Following this, LDV measurements are made at a number of positions along the vertical beam path until the reservoir fluids are spent. (Effective run times are typically about 20 minutes.)

Once the reservoir fluids are exhausted, the flume is drained and flushed out with chlorinated water (removing any residual dye). The flume is then refilled with filtered lab water and a series of 1024 array scans are recorded to determine the background noise level. The unattenuated laser power is then remeasured and the LDV signal processor is re-calibrated. Following this, the LDV and LIF data are transmitted to a VAXstation 3200 for further processing.

2.4. Parameter Settings

A variety of internal flow configurations may be realized in the flume depending upon the choice of control parameters. The parameters that govern the overall flow structure are: the difference between the reservoir fluid densities, $\Delta\rho_0$; the rate of inflow of alcohol-water solution, Q_1; the rate of inflow of saline solution, Q_2; the alcohol-water solution withdrawal rate (from the outlet behind the saline solution inlet), Q_3; and the saline solution withdrawal rate, Q_4.

If the flowrates are large enough, internal hydraulic jumps can occur in the channel. These are typically regions of increased turbulence and mixing and are undesirable inasmuch as they tend to obscure interfacial mixing in more slowly varying regions (and may preclude a local equilibrium analysis).

In idealized two-layer flow, internal hydraulic jumps separate regions of sub-critical and super-critical flow. These are given, respectively, by

$$F_1^2+F_2^2<1, \tag{2.4.1}$$

and

$$F_1^2+F_2^2>1, \tag{2.4.2}$$

where

$$F^2=\frac{U^2}{\sqrt{d\Delta b}}, \tag{2.4.3}$$

is the layer internal Froude number (Armi, 1986). Here d is the single layer depth, Δb is the buoyancy difference between the layers, and U is the layer velocity. To avoid

these internal 'shocks', parameters are chosen which result in sub-critical flow throughout.

The governing parameters chosen for 5 experiments are given in table 2.4.1. Here $\Delta b = g\Delta\rho/\rho$ is the buoyancy difference between the reservoir fluids, Q_1 to Q_4 are the flowrates (per unit span) previously discussed, Q_5 is the rate of flow (per unit span) over the weir, H is the total depth of fluid, l_1 is the distance from the measurement site to the upper layer entrance splitter tip, and l_2 is the distance from the measurement site to the lower layer entrance splitter tip.

Expt	Δb (cm/s^2)	Q_1 (cm^2/s)	Q_2 (cm^2/s)	Q_3 (cm^2/s)	Q_4 (cm^2/s)	Q_5 (cm^2/s)	H (cm)	l_1 (cm)	l_2 (cm)
1	18.81	38.97	36.82	18.88	42.29	14.62	19.25	49	338
4	13.22	39.95	38.74	22.21	41.07	15.41	19.25	49	338
10	12.77	39.75	38.74	20.21	41.07	17.21	19.25	357	30
11	7.48	26.42	38.74	9.56	41.07	14.52	19.25	357	30
13	18.95	39.75	38.74	21.55	40.67	16.27	19.25	168	219

TABLE 2.4.1. Flow parameter settings.

CHAPTER 3

EXPERIMENTAL RESULTS

3.1. Governing Parameters

Results from five experiments are presented in this chapter. Local governing parameters from these are given in table 3.1.1. Here d is the total depth of the lower layer; h (concentration 'boundary layer' thickness) is the distance from the mean interface position, $\overline{\eta}$ (defined in §3.3), to the location above (or below) the interface where the probability of finding fluid differing in concentration from that of the local mean by greater than $.01C_0$ is 0.02;† U is the ratio of the volumetric flowrate to cross-sectional area;†† u_i is the mean horizontal velocity at the interface, estimated by linear interpolation; h_s (maximum velocity gradient thickness) is defined by

$$h_s = \frac{(U_0 - U_1)}{(\partial U / \partial y)_{max}},$$

where $(\partial U / \partial y)_{max}$ is the maximum mean velocity gradient at the interface; Ri_s (mean shear Richardson number) is defined by

$$Ri_s = \frac{\Delta b h_s}{(U_0 - U_1)^2}; \qquad (3.1.1)$$

and Ri (layer Richardson number) is defined by (1.1.1), with the mean layer velocity replacing the free stream velocity. (This is necessary as accurate estimates of

† Physically this is a measure of the level to which scalar is transported vertically by turbulent motions. A number of alternative measures of h are considered, including momentum thickness, displacement thickness, and thickness based on mean or rms concentration. Unfortunately, the sparsity of velocity data precludes estimates of h based on velocity. After some exploration, it is found that a definition of h based on concentration probability is the least sensitive to measurement errors. It is also robust, in the sense that it is relatively insensitive to small changes in probability or concentration deviation threshold.

†† In the upper layer $U_1=Q_1/(H-d)$ and in the lower layer $U_0=Q_4/d$.

maximum layer velocity could not be determined. This does, however, introduce some uncertainty in Ri, since the ratio of layer maximum to mean velocity depends on the relative widths of the boundary layers.)

EXP	d (cm)	h_0 (cm)	h_1 (cm)	h_s (cm)	U_0 (cm/s)	U_1 (cm/s)	u_i (cm/s)	Ri_0	Ri_1	Ri_s
1	6.17	4.14	4.66	2.93	6.89	-2.97	3.34	6.19	2.20	0.57
4	7.10	-†	4.77	1.55	5.73	-3.29	1.22	-	3.10	0.25
10	10.57	6.12	4.45	2.22	3.89	-4.59	-0.04	5.09	2.75	0.40
11	11.83	4.78	3.20	1.17	3.47	-3.56	0.78	4.95	1.27	0.18
13	8.13	4.84	4.31	1.80	4.99	-3.58	1.98	10.13	2.64	0.46

TABLE 3.1.1. Local governing parameters.

† The lower layer in experiment 4 is non-turbulent; hence h_0 and Ri_0 are undefined.

3.2 Velocity Measurements

Raw LDV signals are processed, as discussed in §2.2.1, to yield vertical and horizontal components of fluid velocity at a number of locations along the LIF laser beam path. Results from LDV measurements consist of profiles of mean streamwise velocity, u, profiles of vertical and horizontal rms velocities, u' and v', and horizontal and vertical velocity power spectral densities. Accurate estimates of Reynolds stress, $-\rho\overline{u'v'}$, cannot be determined due to the large size of the LDV focal volume compared with the size of the energy containing eddies. (The span of the focal volume is typically 1.2 to 1.3 cm; energy containing eddies are presumably some fraction of the concentration boundary layer thickness which ranges from about 3 to 6 cm.)

Noise levels encountered in the LDV signals are non-negligible so that some filtering is necessary. Noise spikes, typically spanning one to two time steps, are encountered in some of the velocity data sets (attributed to laser and photodiode noise) which are removed essentially by drawing a straight line across their base. More troublesome, however, is broad-band (white) noise. In measuring the Doppler shifted frequency, broad-band noise is manifested as a random sampling error, approximately independent of the magnitude of the velocity. Since the level of turbulent fluctuations is typically low in the low-speed flows studied, relatively large errors, ranging from 2% to 30%, are introduced in estimates of rms velocities (see table 2.2.1.3).

In order to obtain best possible estimates of velocity fluctuations, Wiener filtering is employed to 'optimally' remove noise from the data. This is done using an algorithm suggested by Press *et al.* (1989). It involves estimating the power spectral

density of the unfiltered data, E(f), estimating the noise spectrum, N(f),† and calculating the optimal filter, $\Phi(f) \sim [1-|N(f)|^2/|E(f)|^2]$. (The filter is optimal in the sense that the mean square deviation between the measured and uncorrupted signal is minimized.) The product of the optimal filter and the Fourier transform of the input signal gives the optimally filtered signal (when transformed back to the time domain).

The statistical convergence is typically 1% to 3% for u and 3% to 8% for u' and v'. (Here convergence is defined as the difference between the statistical estimate using the entire record and that using only the first half of the record divided by the value using the entire record.) Typical approach to convergence for u, u', and v' is shown in figures 3.2.1, 3.2.2 and 3.2.3, respectively. Plotted are values of statistics taken over increasingly longer time intervals: [0, T/(65-N)], where T is the total sample time and N=1 ,..., 64.

† In all cases this is done by locating the noise 'floor', $|N(f)|^2$, from power spectral density estimates and assuming $|N(f)|^2 \sim$ constant for all f.

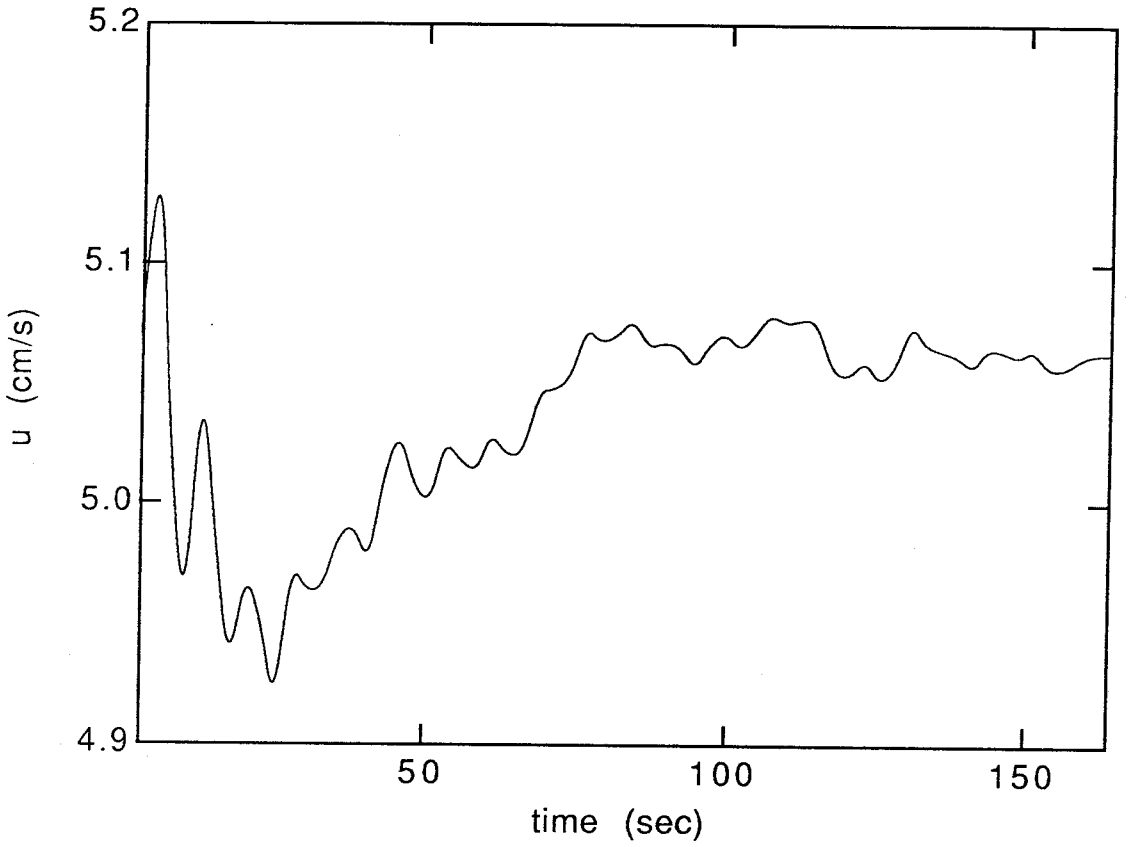

FIGURE 3.2.1. Convergence of mean streamwise velocity. Measurements are from experiment 13 at $(\overline{\eta}-y)/h_0=0.49$. (Here y is the vertical co-ordinate.)

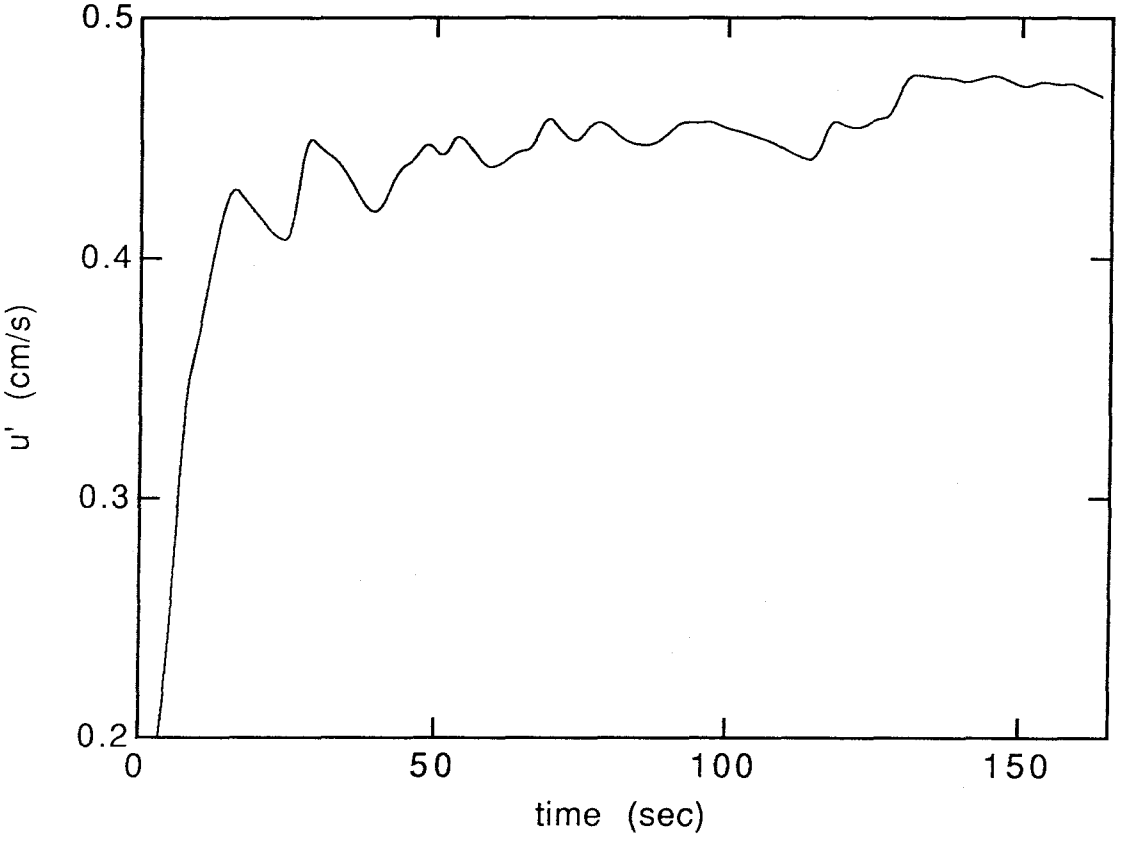

FIGURE 3.2.2. Convergence of rms streamwise velocity. Measurements are from experiment 13 at $(\overline{\eta}\text{-}y)/h_0=0.49$.

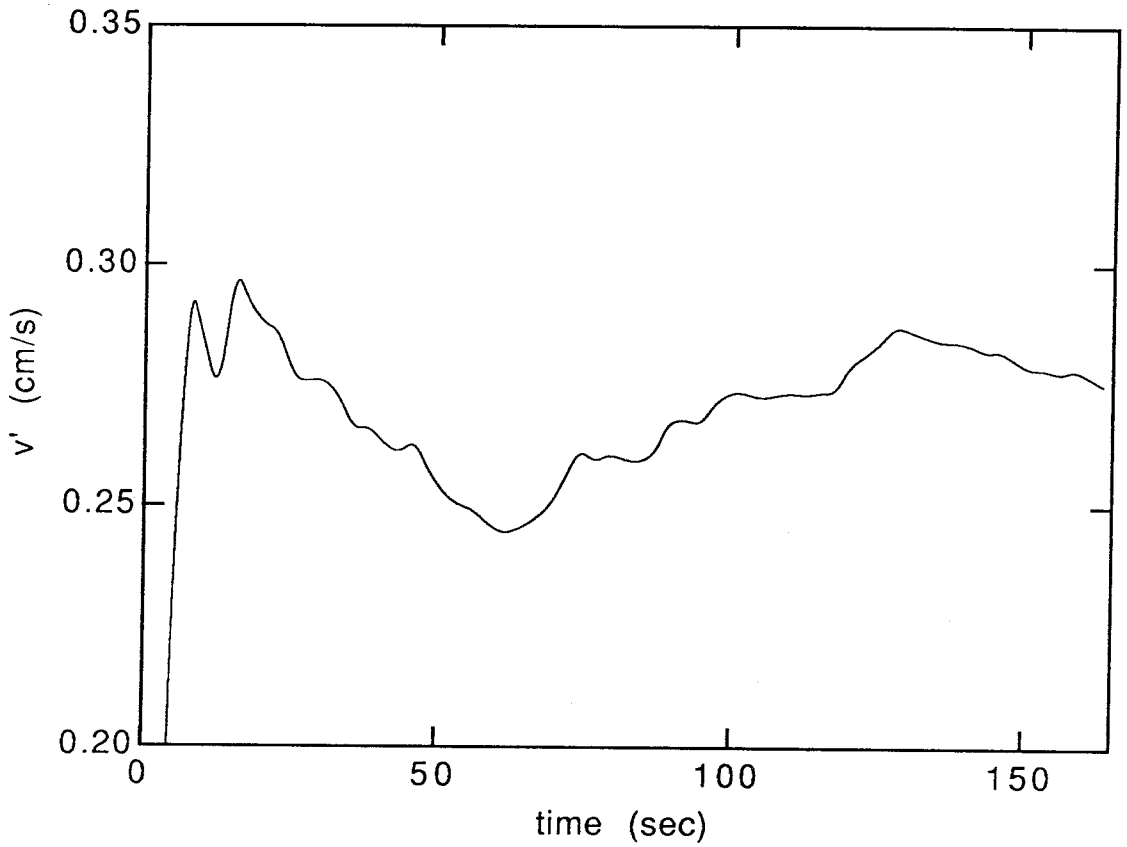

FIGURE 3.2.3. Convergence of rms vertical velocity. Measurements are from experiment 13 at $(\overline{\eta}-y)/h_0=0.49$.

Profiles of mean streamwise velocity, u, normalized by the difference between the mean layer velocity and the velocity at the interface are shown in figures 3.2.4 and 3.2.5 with error bars on several representative data points. Here normalized velocity error is due primarily to uncertainty in u_i, estimated as $(\delta/4)(\partial U/\partial y)_{max}$, where δ is the density interface thickness. Positional error is primarily due to uncertainty in h, estimated as the mean distance imaged by 10 pixels (typically ~ 0.25 cm). In these figures y is the vertical co-ordinate. Profiles of rms streamwise and vertical velocity, u' and v', are shown in figures 3.2.6 through 3.2.9.

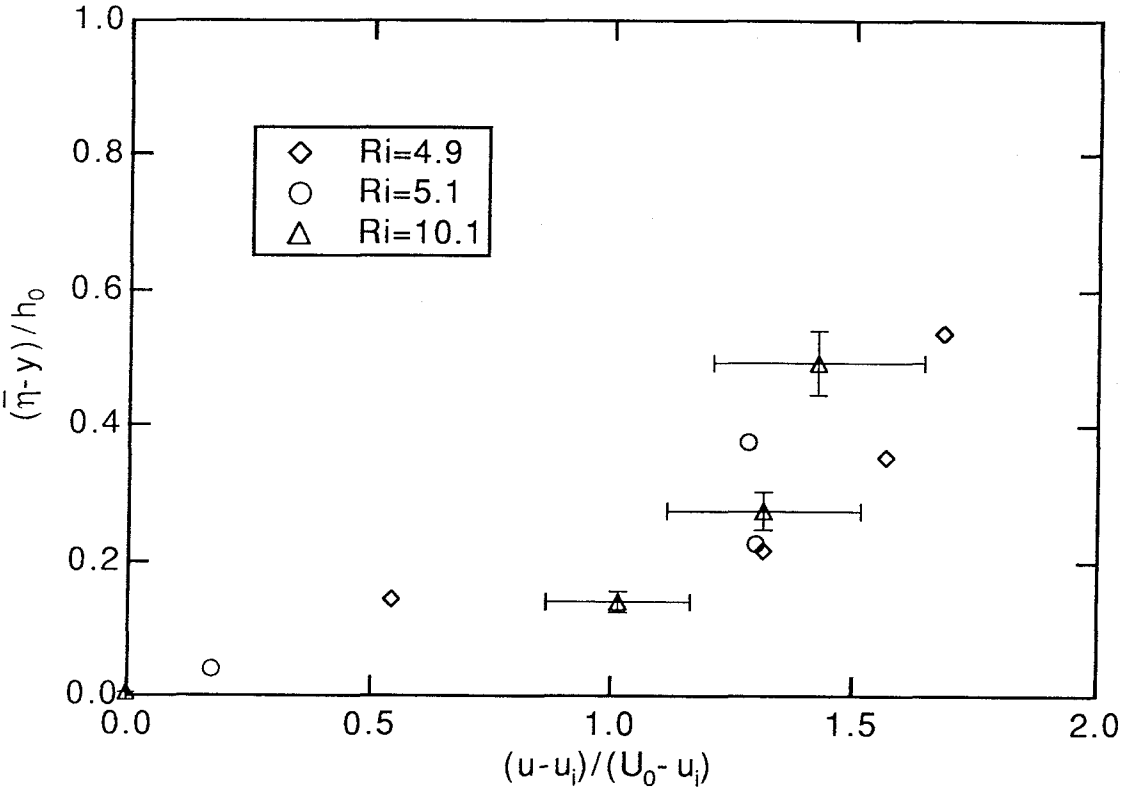

FIGURE 3.2.4. Mean streamwise velocity. Values are from the lower layer.

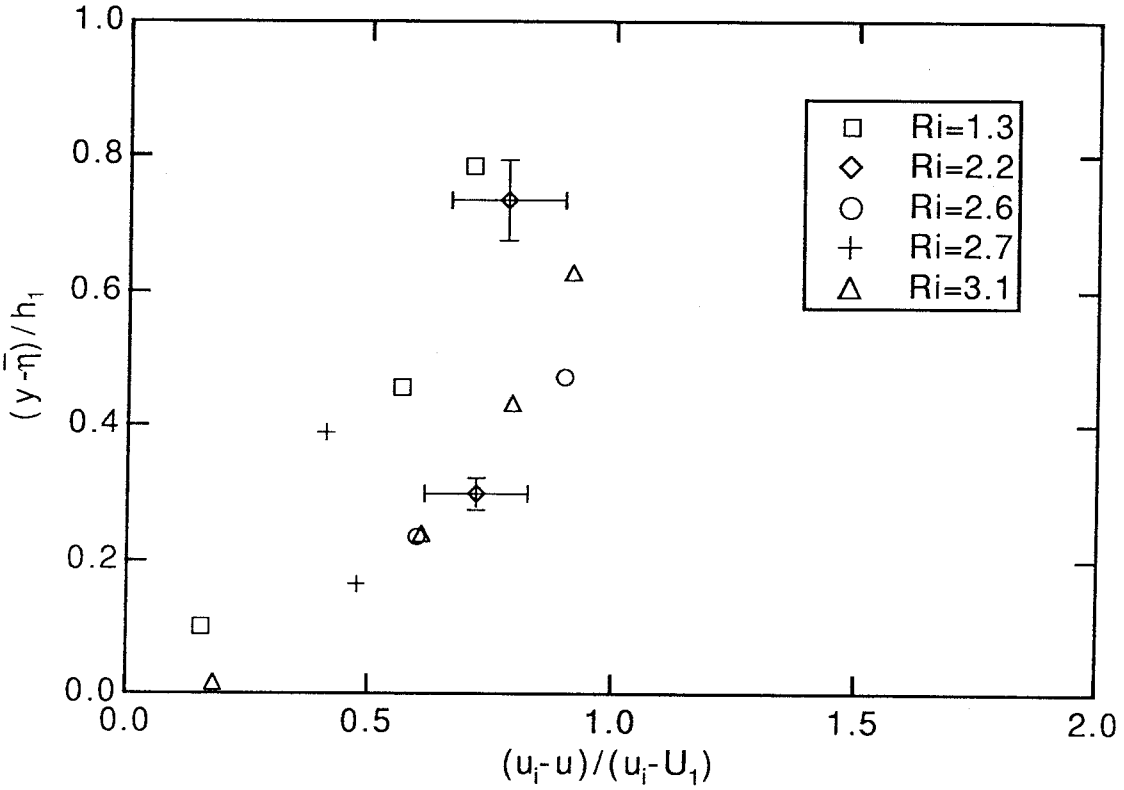

FIGURE 3.2.5. Mean streamwise velocity. Values are from the upper layer.

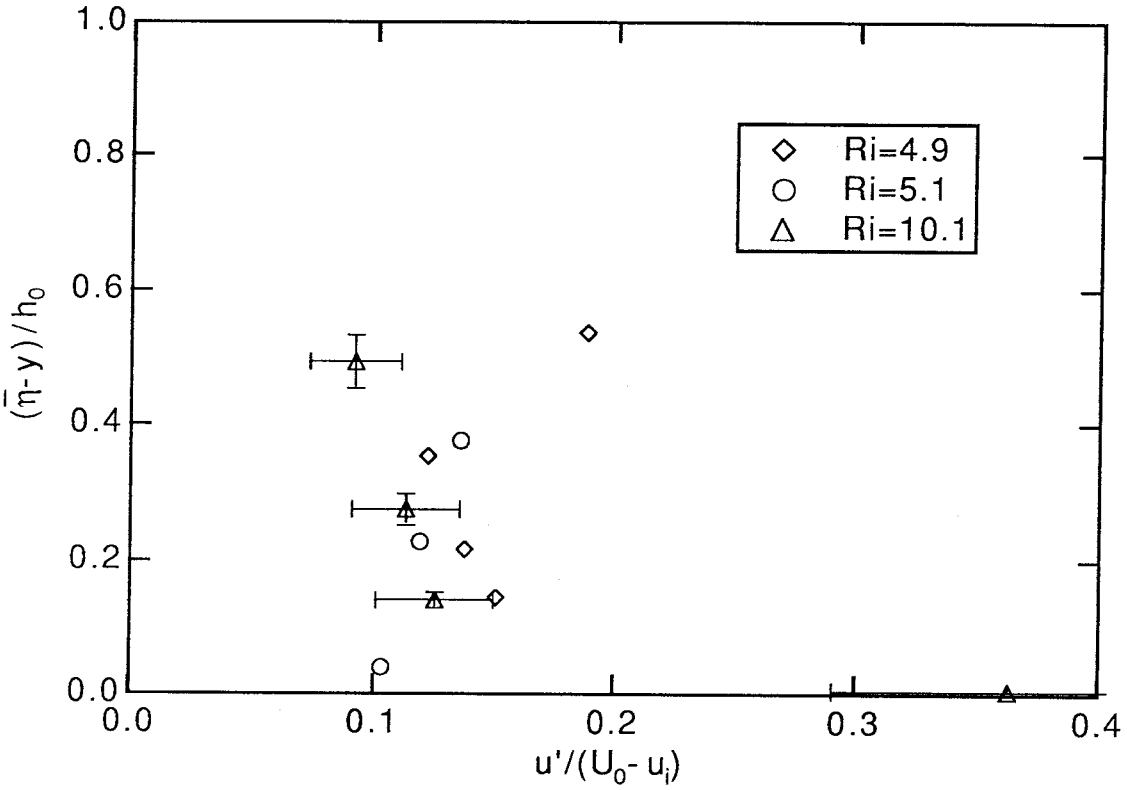

FIGURE 3.2.6. Rms streamwise velocity. Values are from the lower layer.

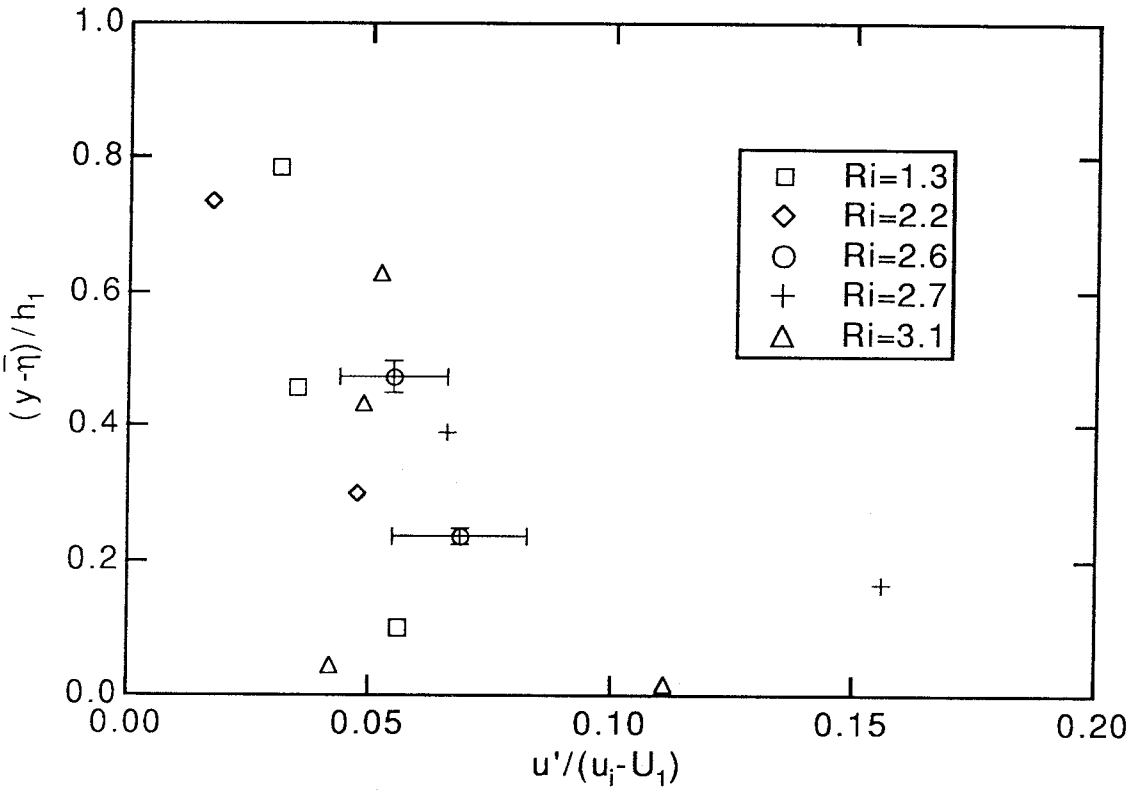

FIGURE 3.2.7. Rms streamwise velocity. Values are from the upper layer.

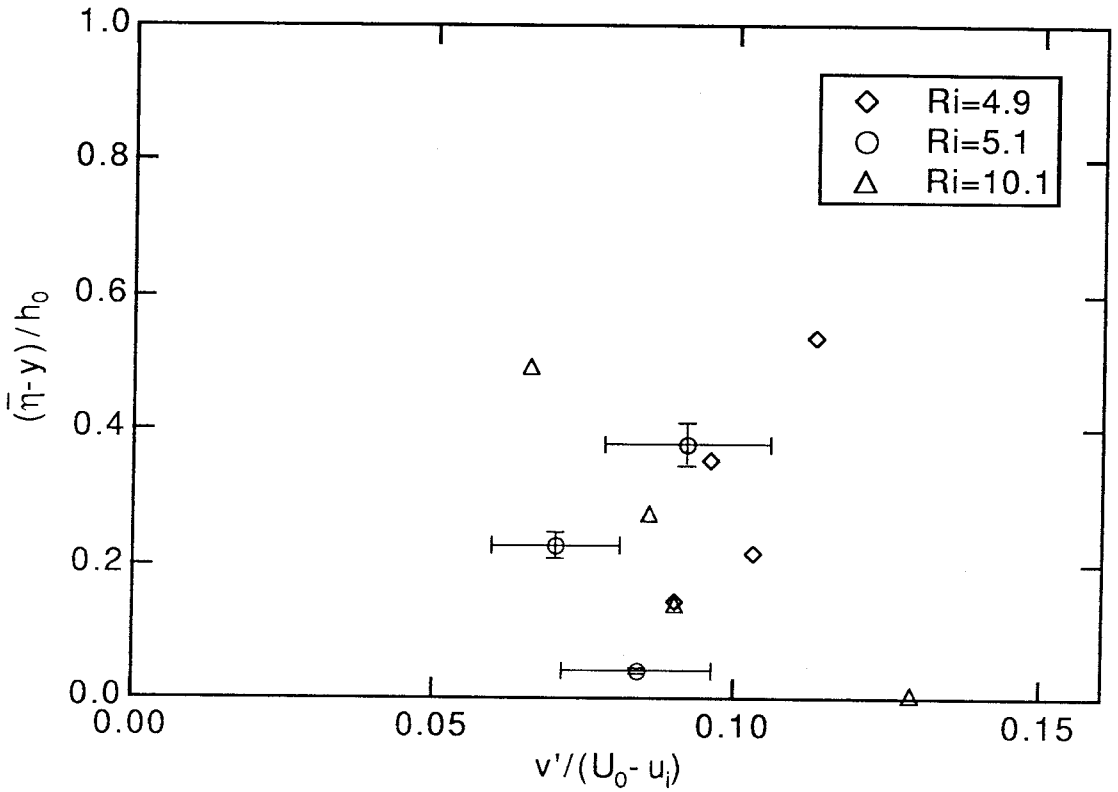

FIGURE 3.2.8. Rms vertical velocity. Values are from the lower layer.

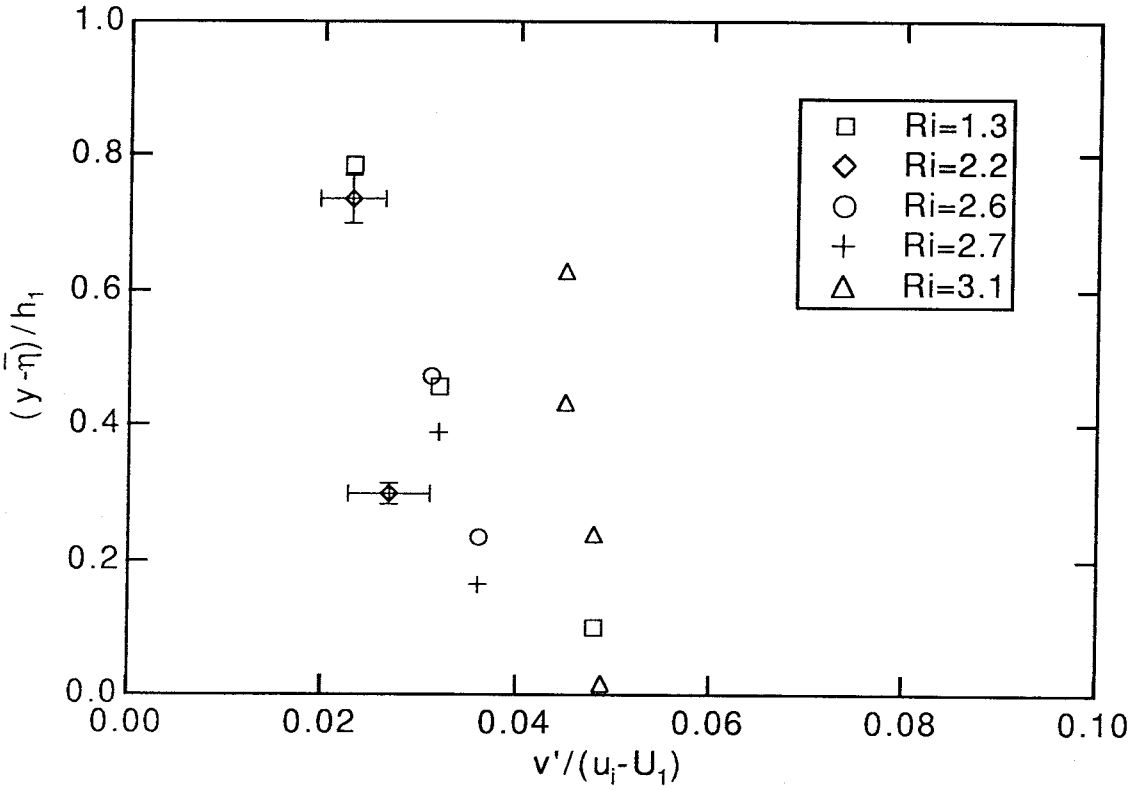

FIGURE 3.2.9. Rms vertical velocity. Values are from the upper layer.

Estimates of streamwise and vertical velocity power spectral densities are shown in figures 3.2.10 through 3.2.13. Spectral estimates are determined using a slightly modified version of a method suggested by Press *et al.* (1989).

The data are initially read in as overlapping segments of length 2048 points (overlap is 1024 points) and a least squares linear fit is subtracted from each segment to remove any trends. Each segment is then multiplied by a Parzen (triangular) window to minimize leakage of spectral power to neighboring frequency bins and an FFT is performed. Finally, the squares of the frequency components from the segments are appropriately averaged. Overlapping data segments and averaging in this way reduces the spectral variance per data point by a factor of about 11.

The streamwise velocity power spectral density is defined such that

$$\overline{u'^2} = \int_0^\infty E_u(f)df, \tag{3.2.1}$$

where E_u is the power spectral density and f is the frequency. The vertical velocity power spectral density is similarly defined. Shown in figures 3.2.10 to 3.2.13 are normalized spectra, Eu/u'^2h, plotted versus normalized frequency, fh/u. Here u is the magnitude of the local mean streamwise velocity and u' is the local rms velocity.

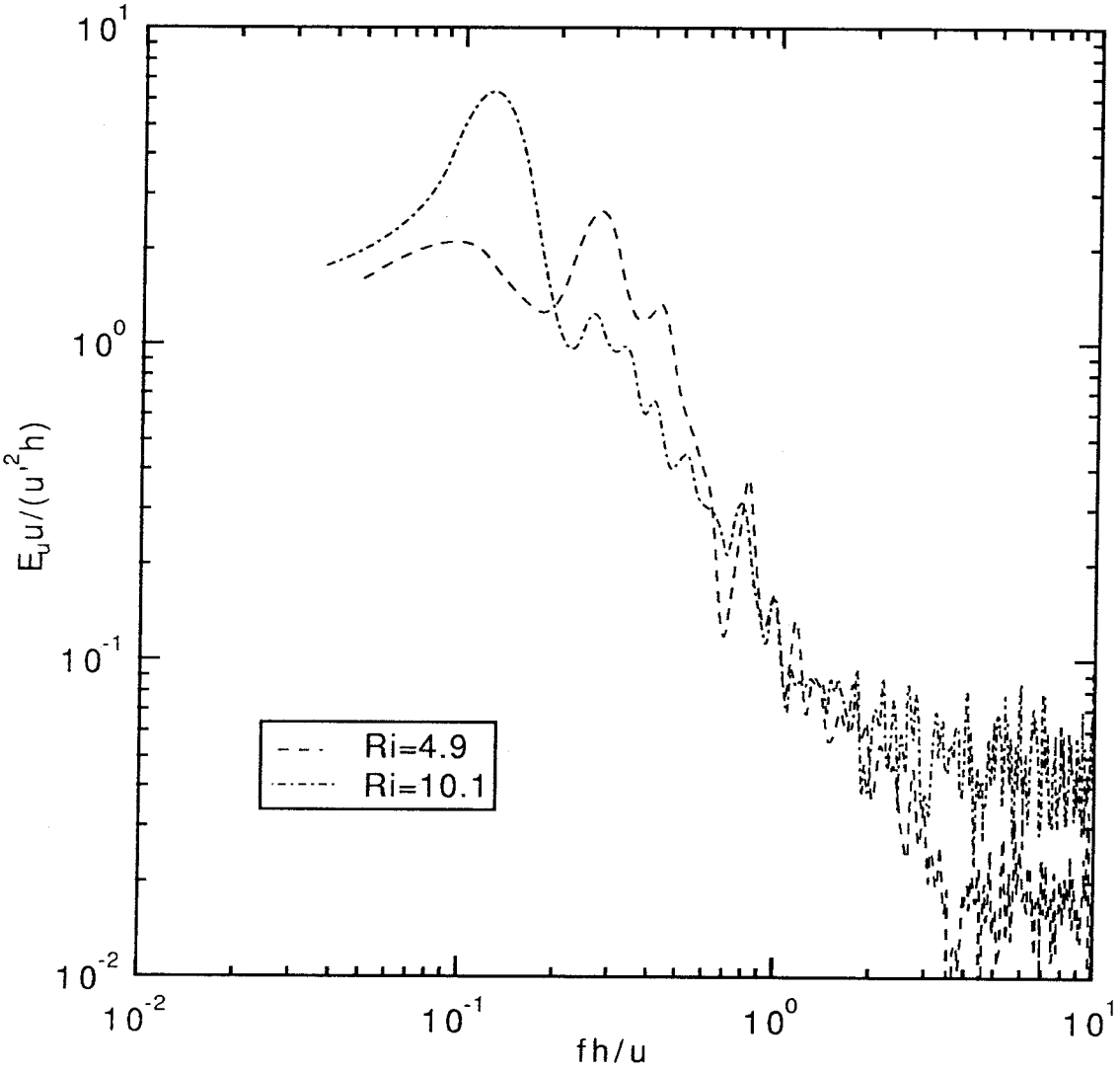

FIGURE 3.2.10. Power spectral density estimates for streamwise velocity. Estimates are from the lower layer near $(\overline{\eta}-y)/h_0=0.45$.

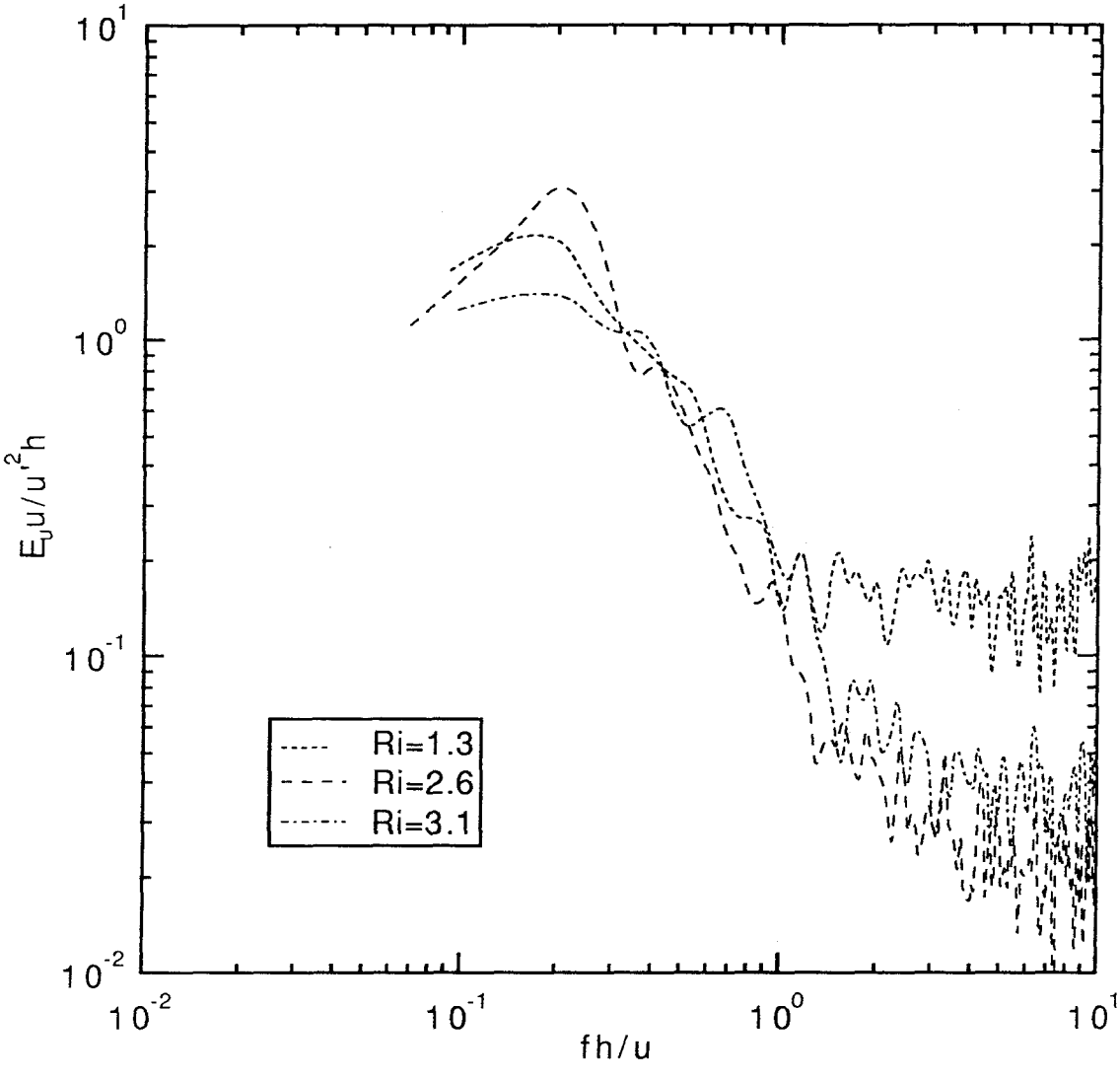

FIGURE 3.2.11. Power spectral density estimates for streamwise velocity. Estimates are from the upper layer near $(y-\overline{\eta})/h_1=0.41$.

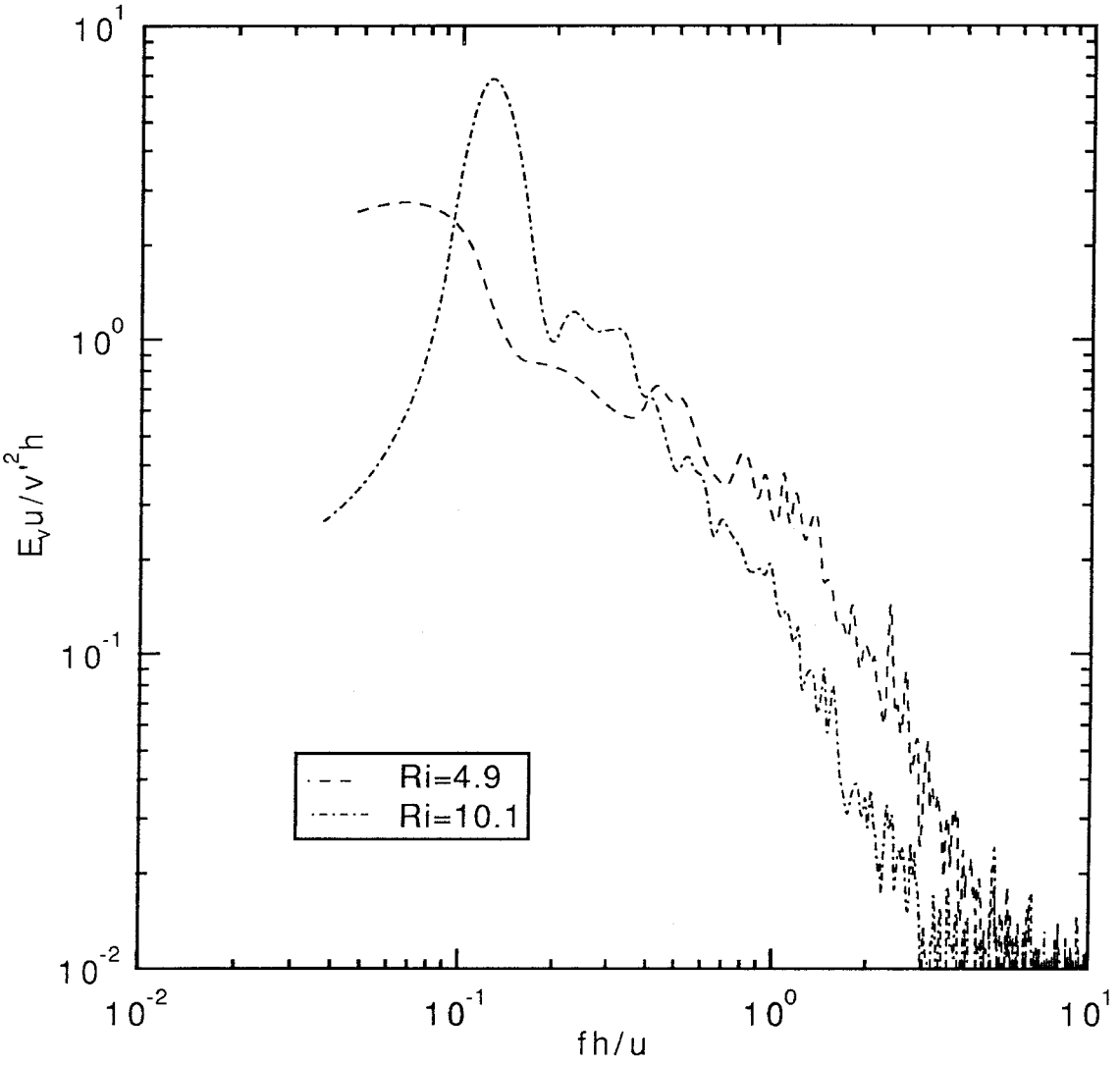

FIGURE 3.2.12. Power spectral density estimates for vertical velocity. Estimates are from the lower layer near $(\overline{\eta}\text{-}y)/h_0=0.45$.

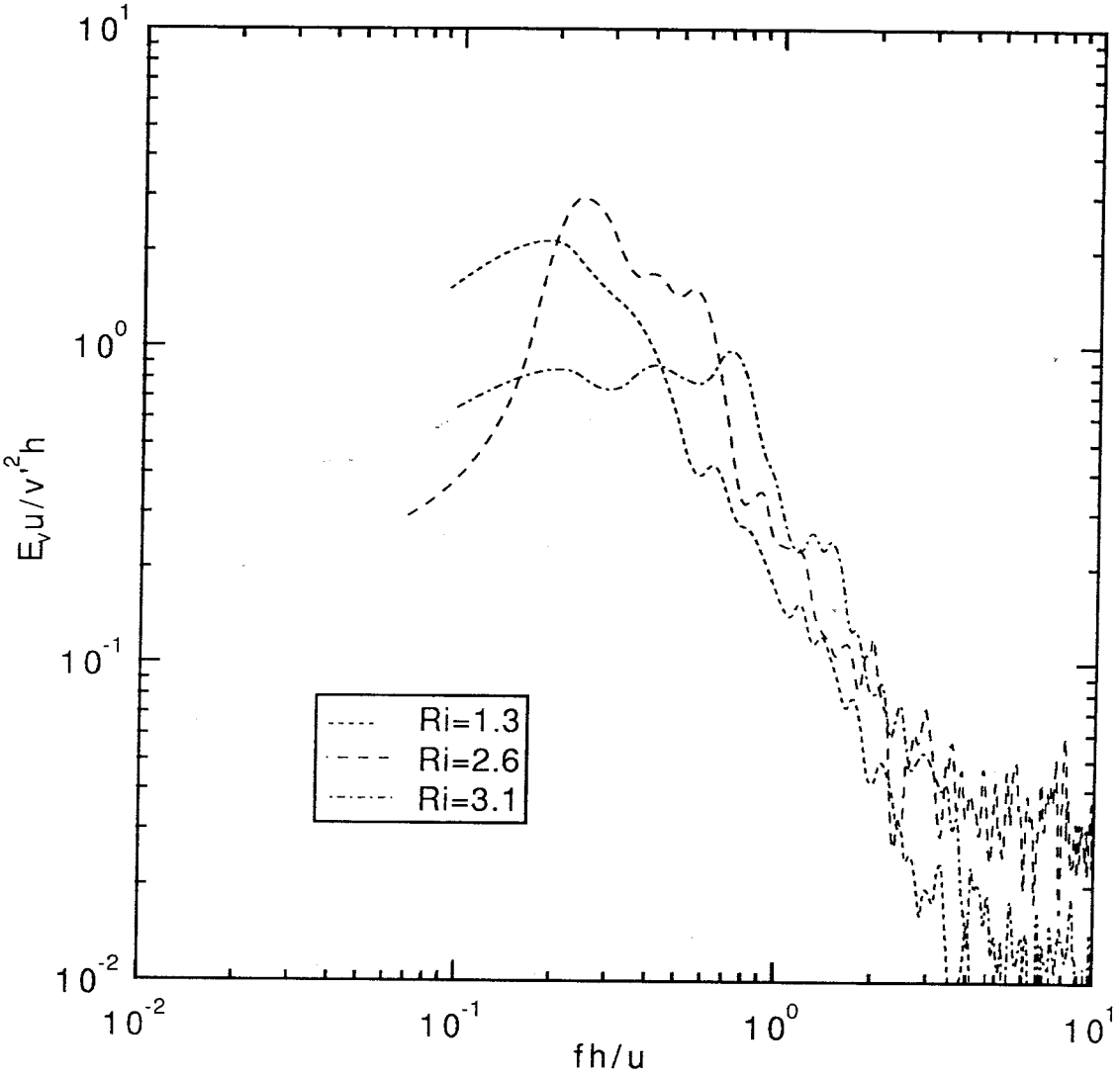

FIGURE 3.2.13. Power spectral density estimates for vertical velocity. Estimates are from the upper layer near $(y-\overline{\eta})/h_1=0.41$.

3.3 Concentration Measurements

Raw photodiode readings are processed to yield values of tracer dye concentration, c(y,t), as discussed in §2.2.2. Each array scan is normalized by the concentration close to the floor to correct for laser fluctuations (typically 1% to 2%). This is justified since in all cases the fluid close to the floor is, to a very good approximation, pure unmixed lower layer fluid. (In all cases deviations in concentration from pure unmixed fluid near the floor are nearly undetectable.)

Statistical convergence for mean and rms concentrations is typically 1% to 2% and 3% to 5%, respectively, as defined in §3.2. Typical approach to convergence for $\bar{c}$ and c' is shown in figures 3.3.1 and 3.3.2.

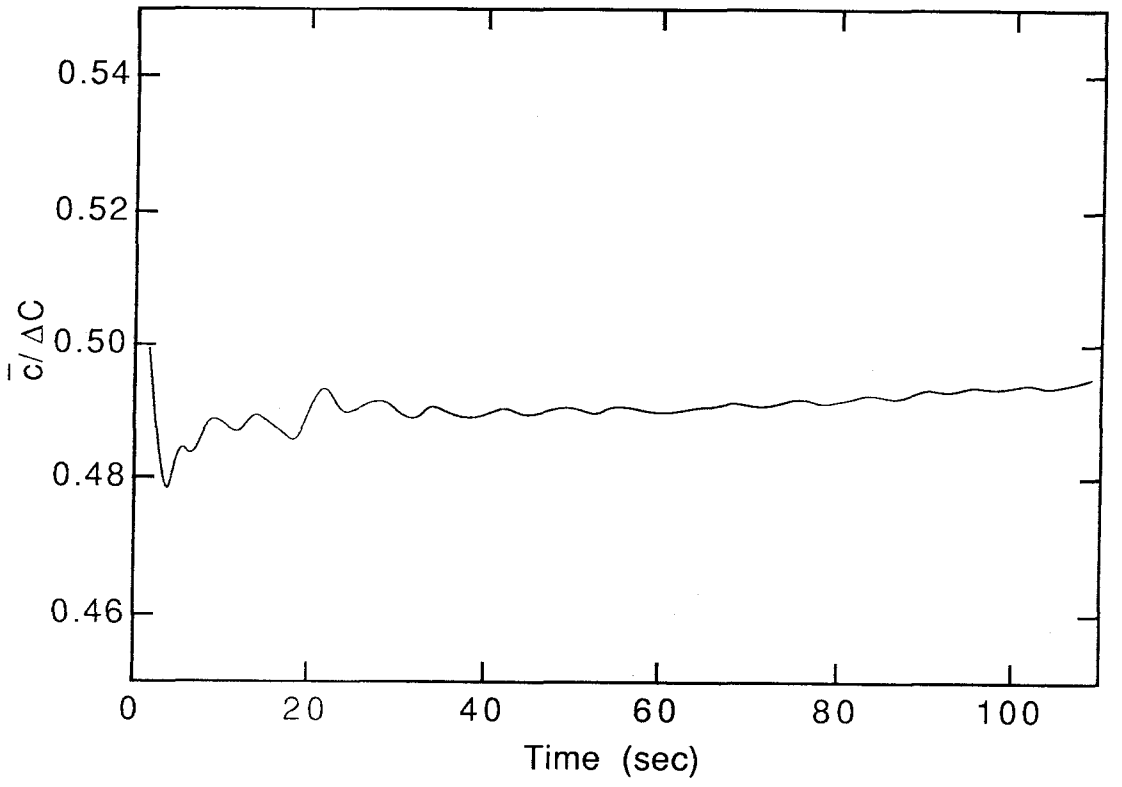

FIGURE 3.3.1. Convergence of mean concentration, $\bar{c}$, from experiment 13. Measurements are taken at the mean interface position.

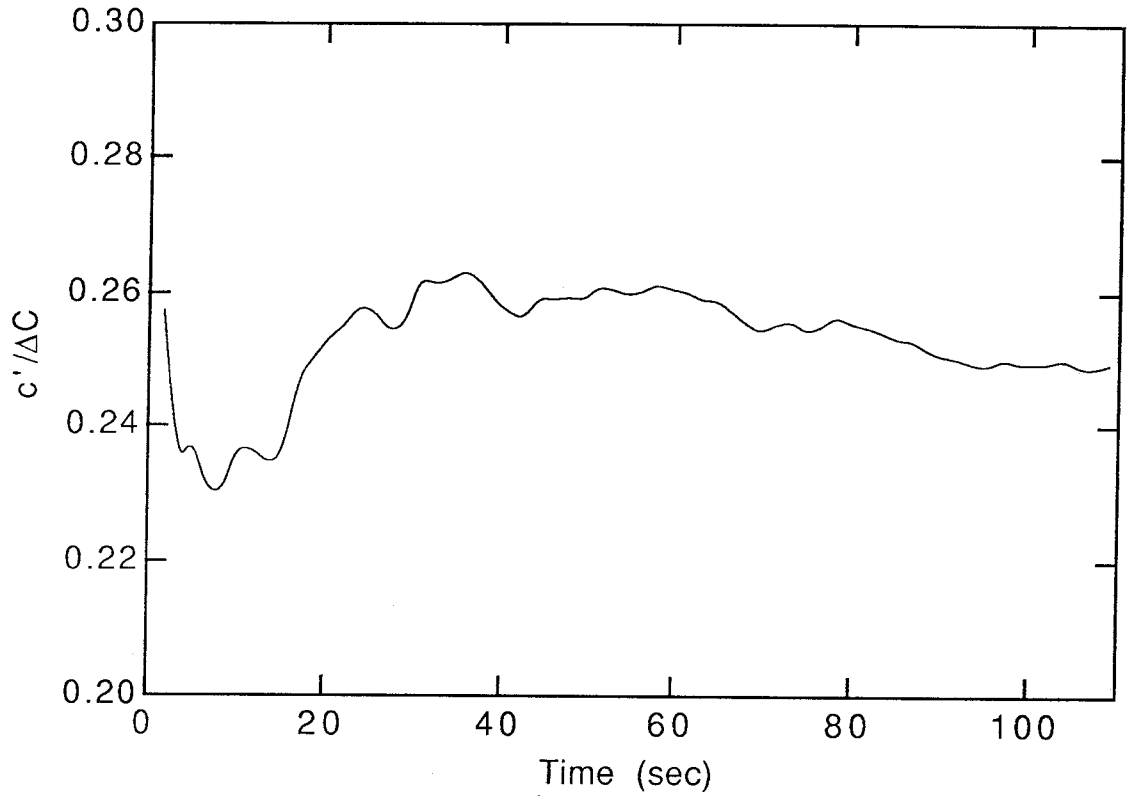

Figure 3.3.2. Convergence of rms concentration, c', from experiment 13. Measurements are taken at the mean interface position.

False color images of concentration in t-y space are shown in figures 3.3.3 through 3.3.8. Here t is time and y is vertical position (zero references are taken arbitrarily). Images are created using a VAXstation 3200 with a 1024 x 864, 8-plane (256 color) graphics monitor. In each of these figures time increases from left to right with reference scales as shown. Using a Taylor type hypothesis the t-axis in these images may be viewed locally as x/u, where u is the local convection velocity (which varies in the vertical), and x is distance in the horizontal.

In figures 3.3.3, 3.3.4, and 3.3.5 the point at which u=0 is displaced approximately 0.8 cm, 0.4 cm, and 0.4 cm, respectively, above the mean position of the interface. Below the point of zero velocity the flow may be viewed locally as moving from right to left with vorticity in the clockwise sense; above the point of zero velocity the flow may also be viewed locally as moving from right to left, but with vorticity in the counter-clockwise sense.

Figures 3.3.3 to 3.3.5 show concentration evolution over 1024 array scans from 3 different experiments. Figures 3.3.6, 3.3.7, and 3.3.8 show, respectively, a close-up of a wave-breaking event, a K-H instability, and intense K-H shear instabilities.

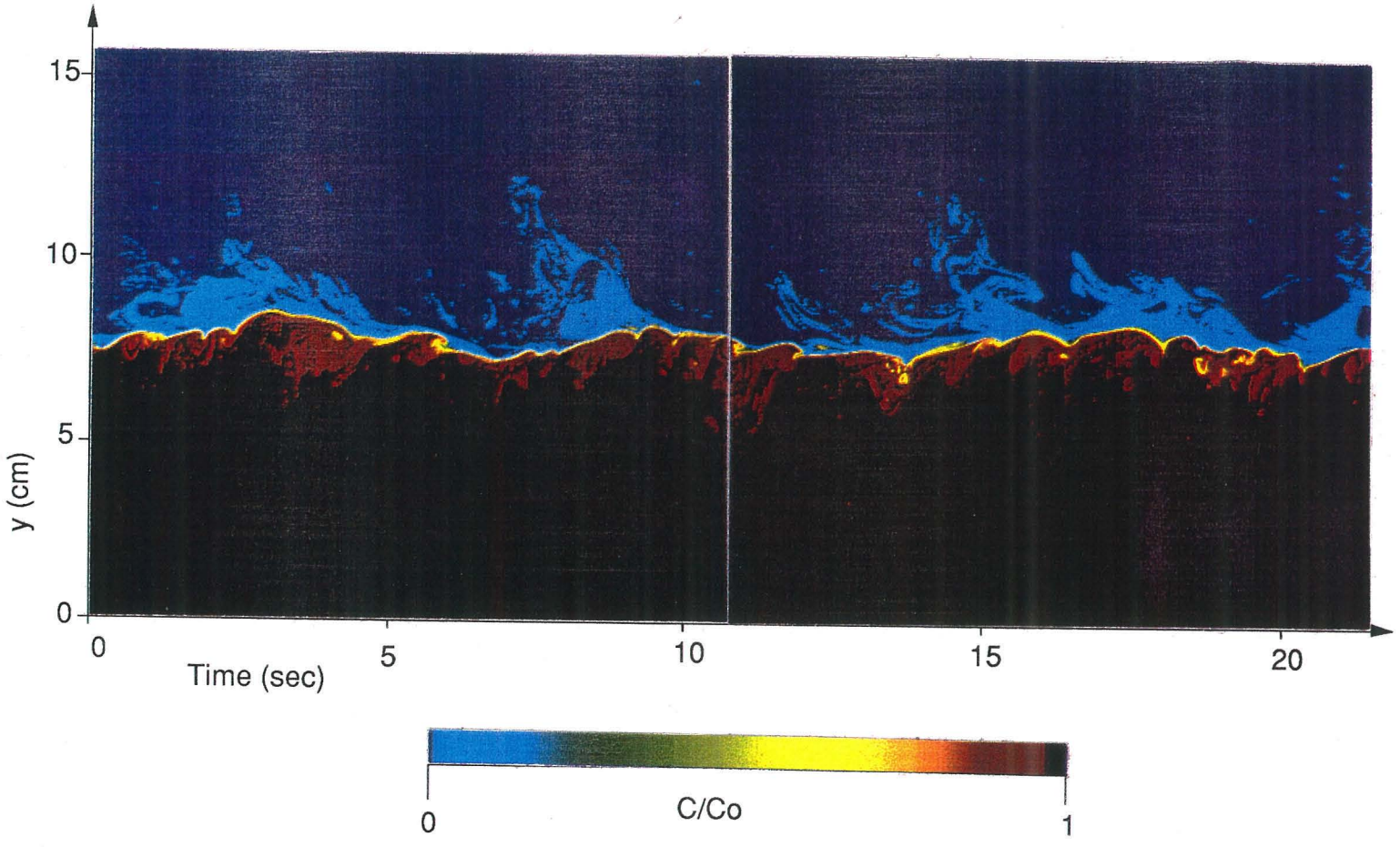

FIGURE 3.3.3. False colour image of concentration from experiment 13 (Ris=0.46). The zero velocity point is displaced approximately 0.8 cm above the mean interface position.

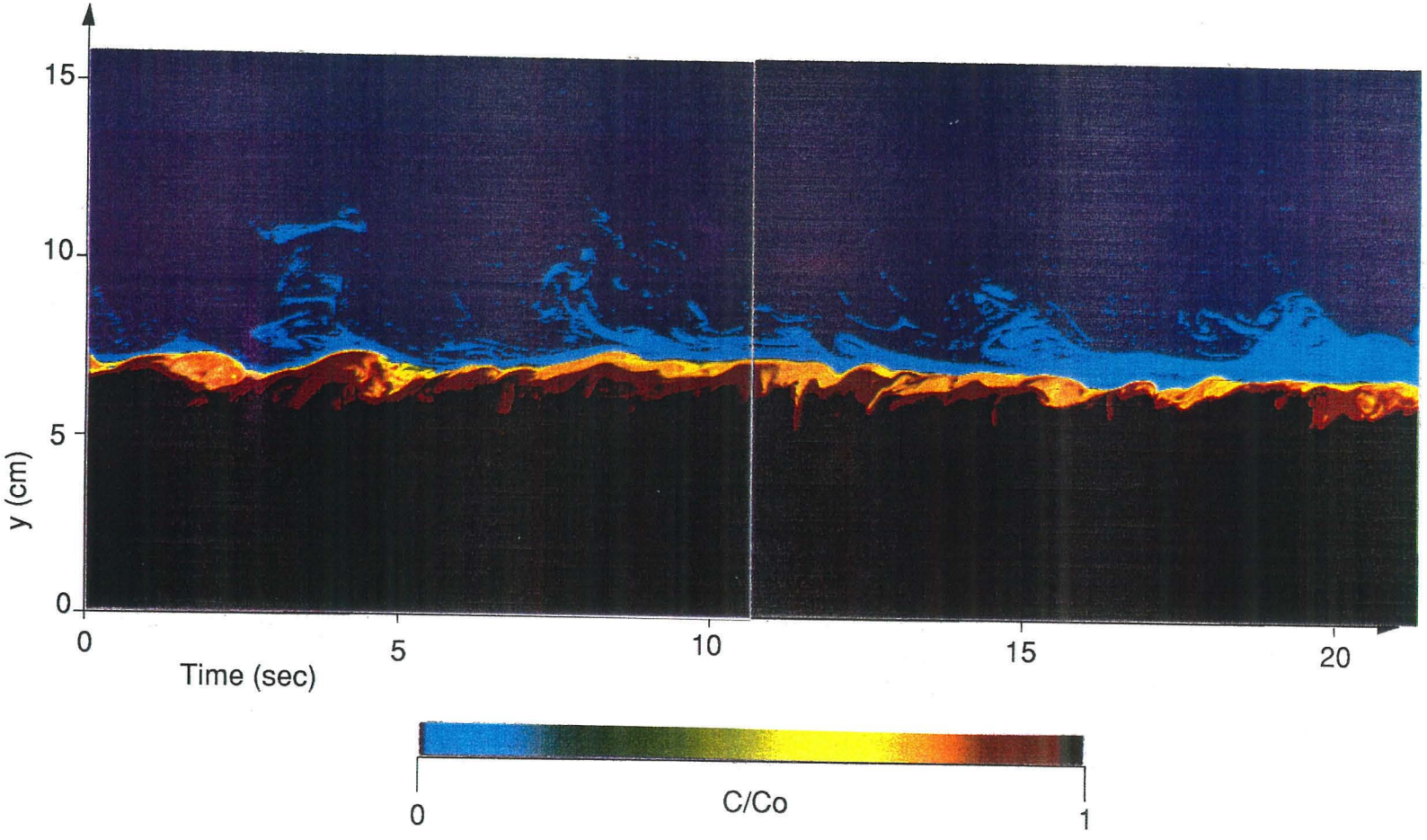

FIGURE 3.3.4. False colour image of concentration from experiment 4 (Ris=0.26). The zero velocity point is displaced approximately 0.4 cm above the mean interface position.

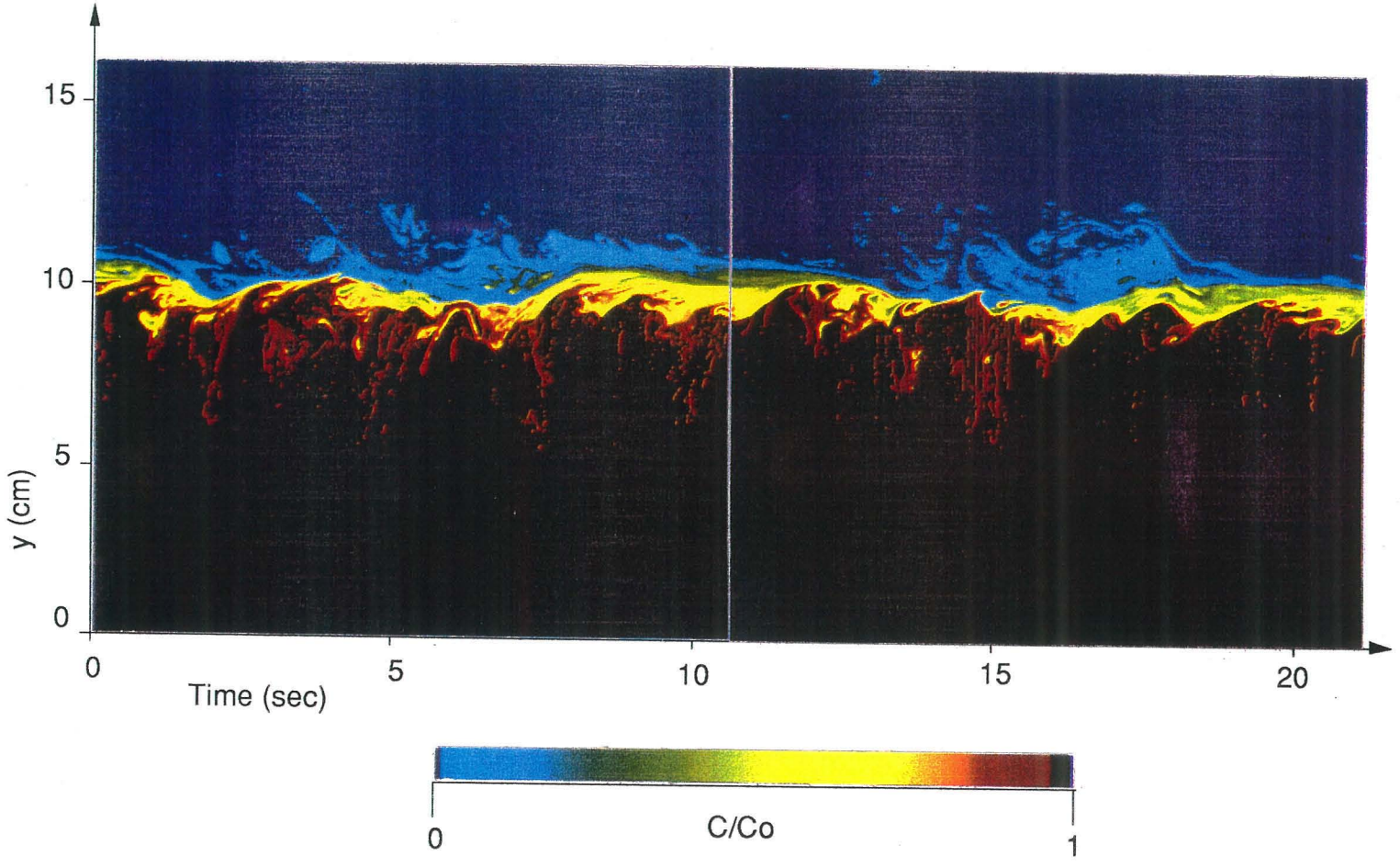

FIGURE 3.3.5. False colour image of concentration from experiment 11 (Ris=0.17). The zero velocity point is displaced approximately 0.4 cm above the mean interface position.

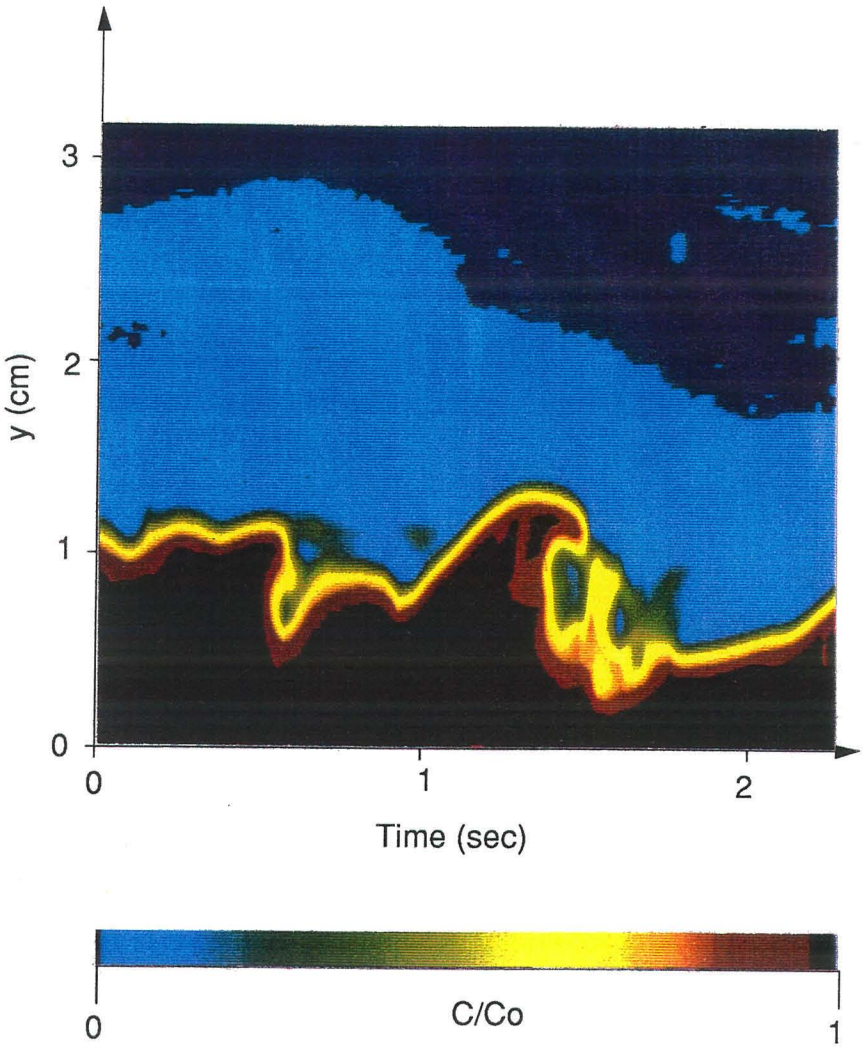

FIGURE 3.3.6. False colour image of a wave breaking event from experiment 1 (Ri_S=0.57). The zero velocity point is displaced approximately 1.0 cm above the mean interface position.

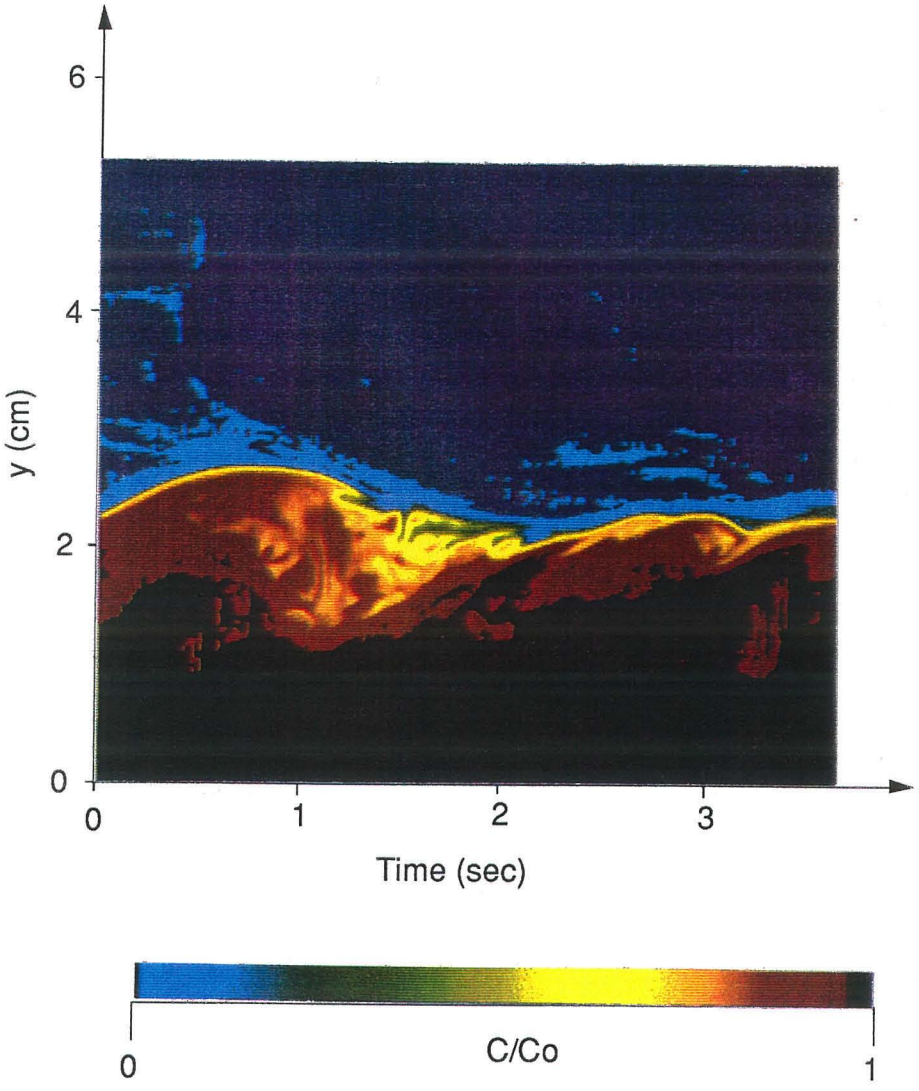

FIGURE 3.3.7. False colour image of a large scale Kelvin-Helmholtz instability from experiment 4. The zero velocity point is displaced approximately 0.4 cm above the mean interface position.

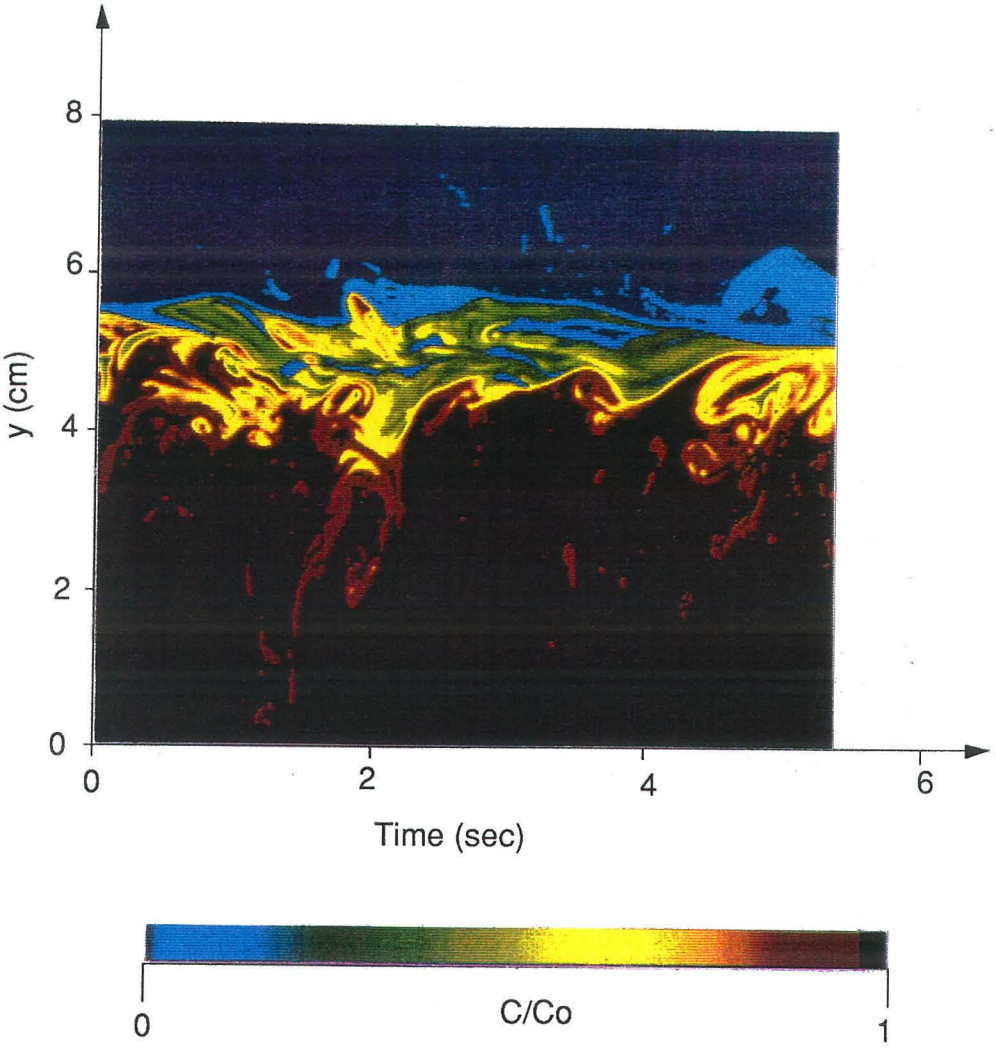

FIGURE 3.3.8. False colour image of intense shear instabilities from experiment 11. The zero velocity point is displaced approximately 0.4 cm above the mean interface position.

Profiles of mean concentration, $\overline{c}$, in the upper layer are shown in figure 3.3.9. Here (and in following figures) concentration is measured in a frame of reference moving with the interface to filter out effects of interfacial waves. In figure 3.3.1 profiles are shown in the upper half of the concentration boundary layer where it is assumed that variations in mean concentration are due to turbulent scalar transport. In almost all cases this region lies well above the region of influence of local interfacial instabilities.

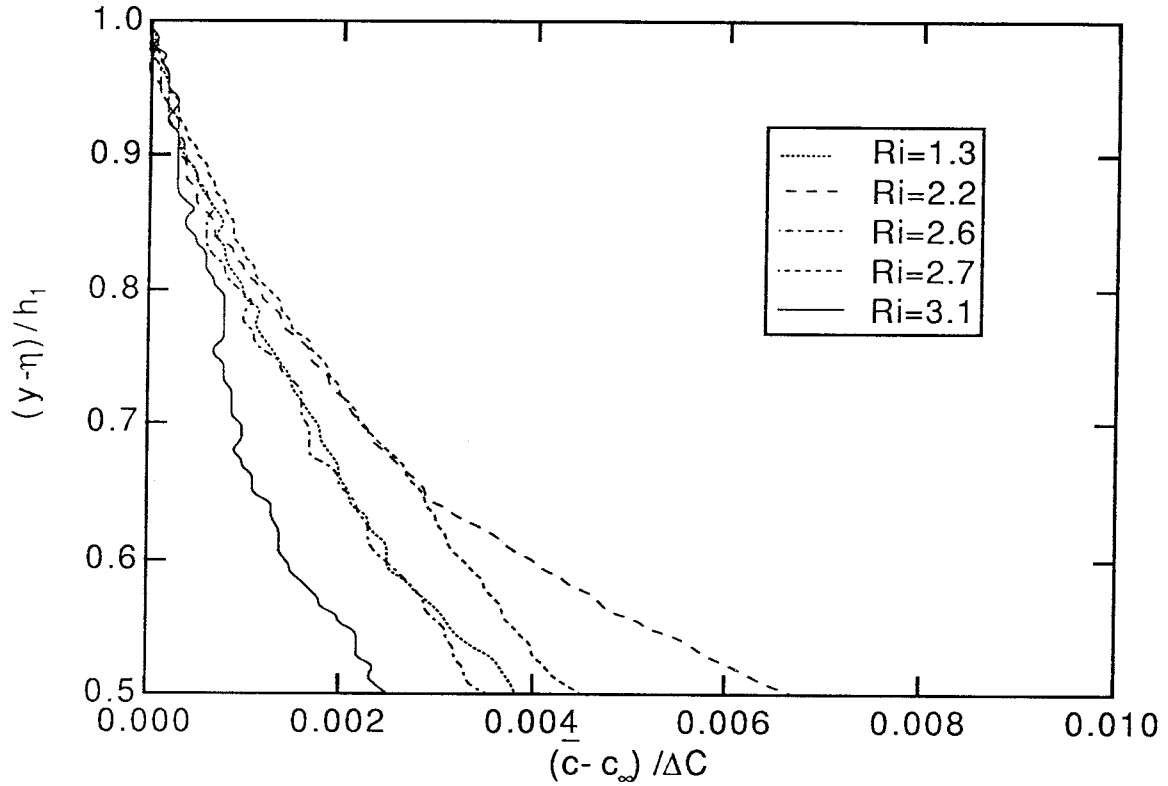

FIGURE 3.3.9. Mean concentration in a frame of reference moving with the interface. Values are from the upper layer. Here ΔC is the difference in mean concentration between the layers and c_∞ is the mean concentration at the outer edge of the layer.

In figures 3.3.10 and 3.3.11 mean concentration near the interface is shown versus normalized distance from the interface. Here distance is normalized by the interface half-width, δ_0 or δ_1, defined as the vertical distance between η and the point below (above) η where c first rises (falls) above (below) $0.9\Delta C$ ($0.1\Delta C$). Near the interface, interfacial instabilities strongly influence the form of the mean concentration profile. In figure 3.3.12 a typical instantaneous profile is shown superposed on the corresponding mean profile.

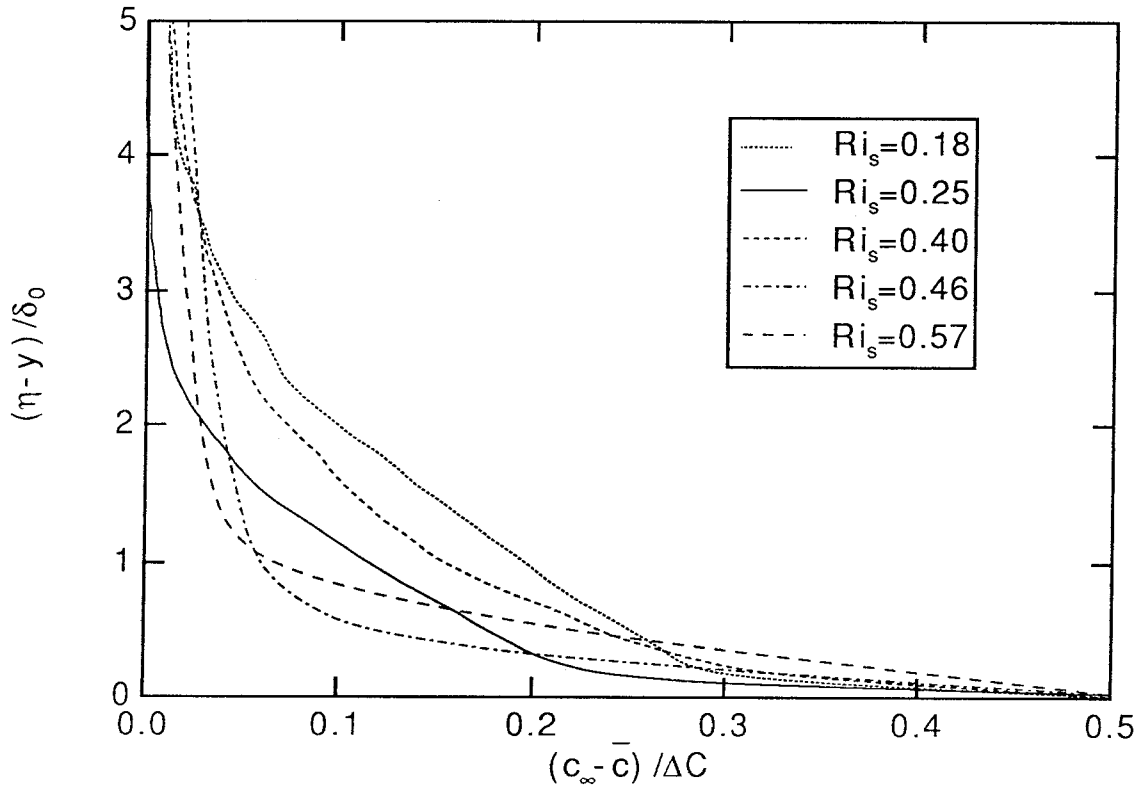

FIGURE 3.3.10. Mean concentration in a frame of reference moving with the interface. Values are from the lower layer.

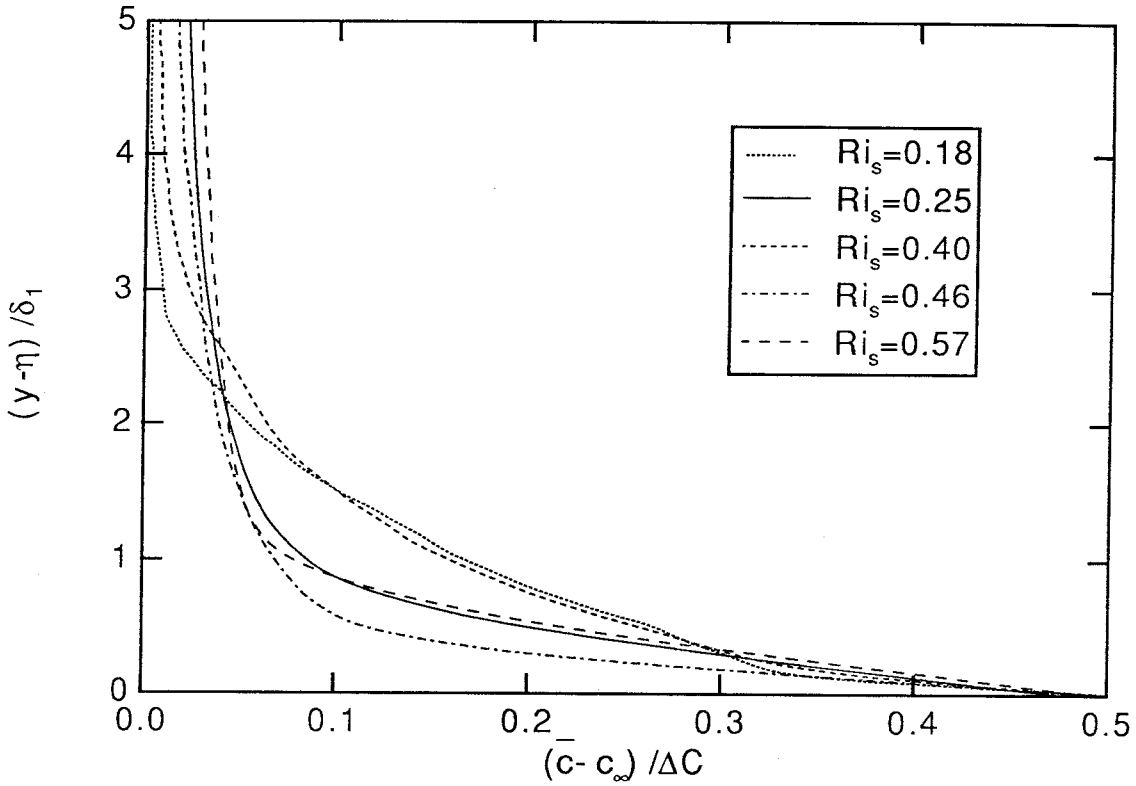

FIGURE 3.3.11. Mean concentration in a frame of reference moving with the interface. Values are from the upper layer.

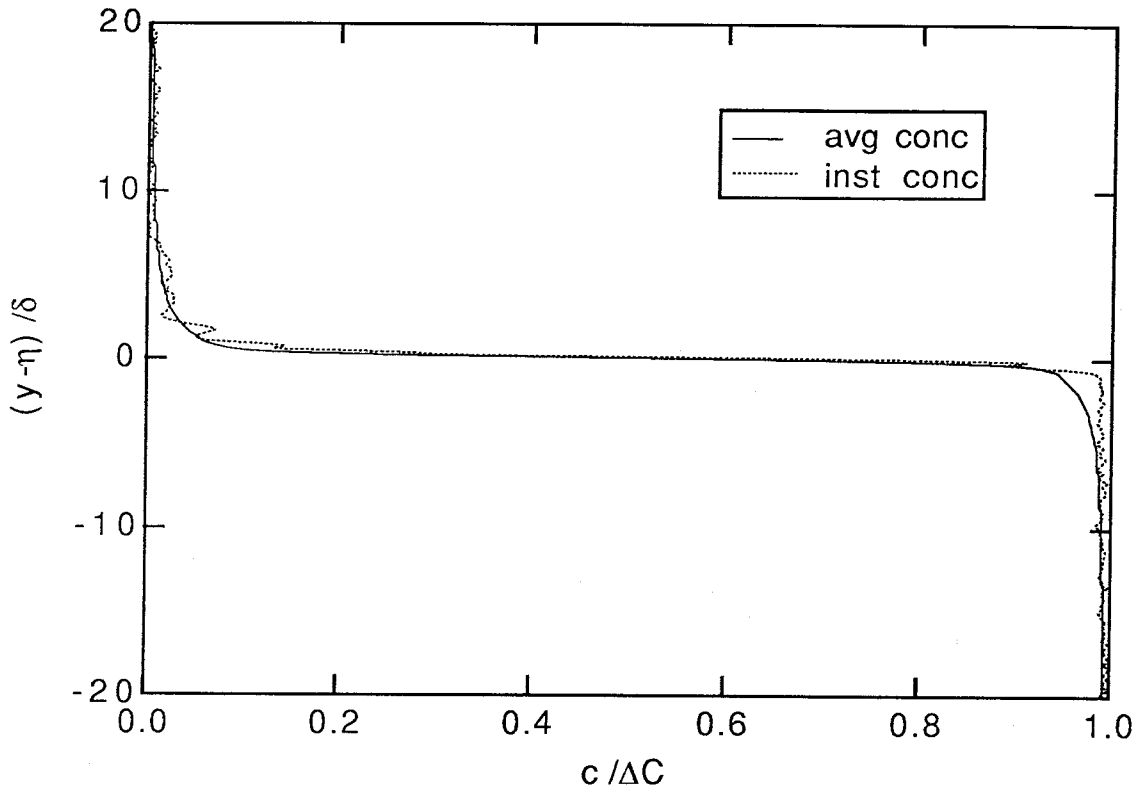

FIGURE 3.3.12. Typical instantaneous concentration profile superposed on the corresponding mean profile. Values are taken from experiment 13.

Profiles of rms concentration fluctuations in the upper half of the upper layer are shown in figure 3.3.13. Here it is assumed that fluctuations are due to turbulent scalar transport (and not interfacial instabilities). The average noise level shown in figure 3.3.13 is based on measured values of c' in an equivalent homogeneous layer.

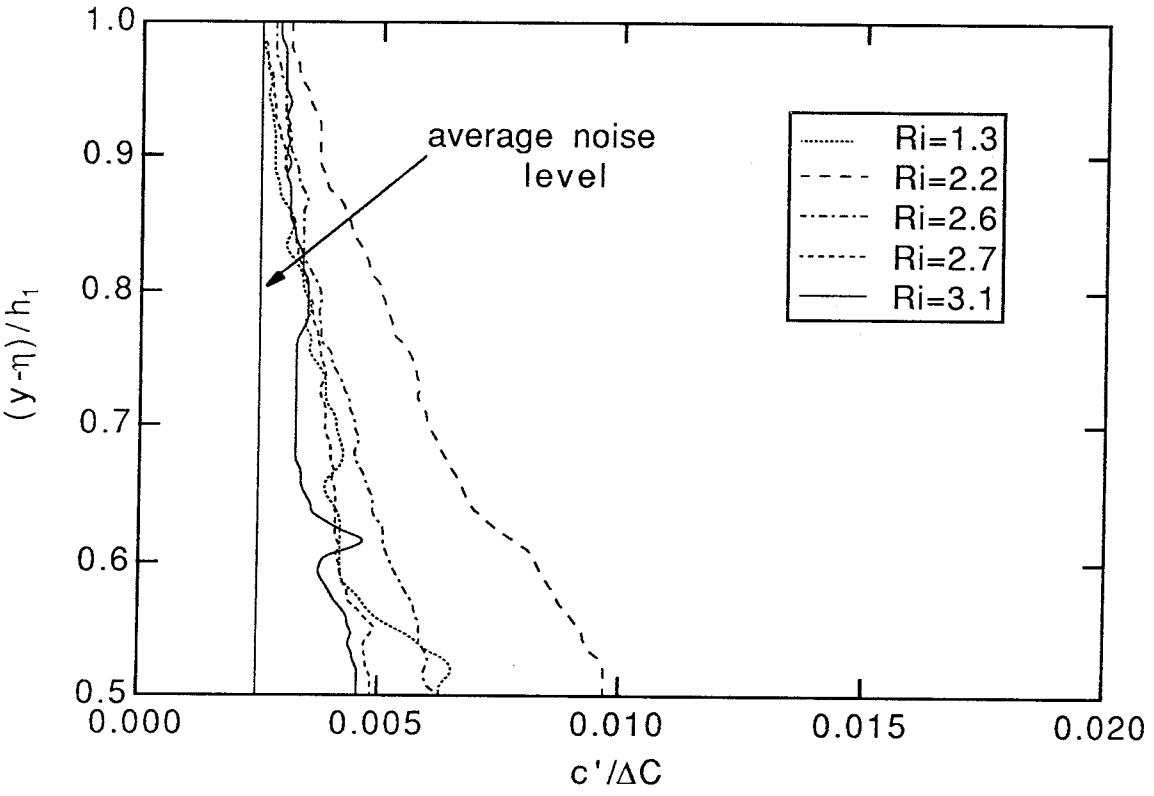

FIGURE 3.3.13. Rms concentration in a frame of reference moving with the interface. Values are from the upper layer.

In figures 3.3.14 and 3.3.15 rms concentration fluctuations near the interface are shown. Here relatively large fluctuations are due primarily to interfacial instabilities.

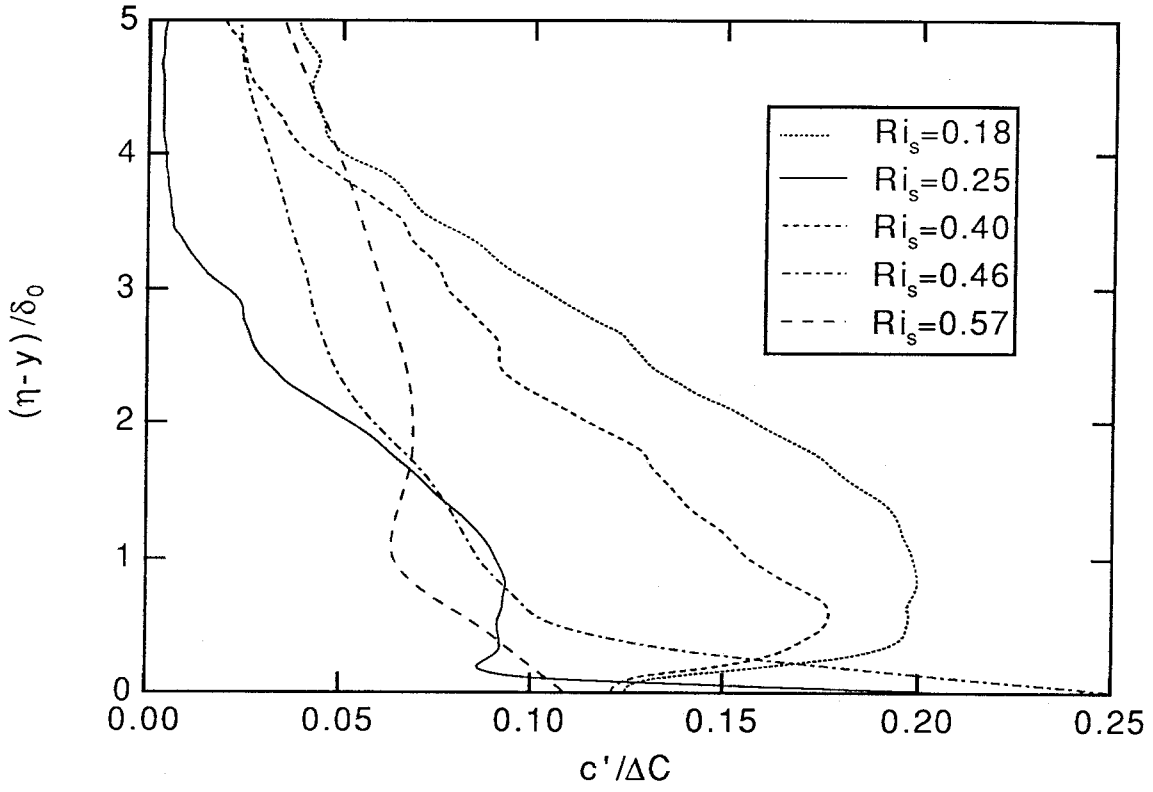

FIGURE 3.3.14. Rms concentration in a frame of reference moving with the interface. Values are from the lower layer.

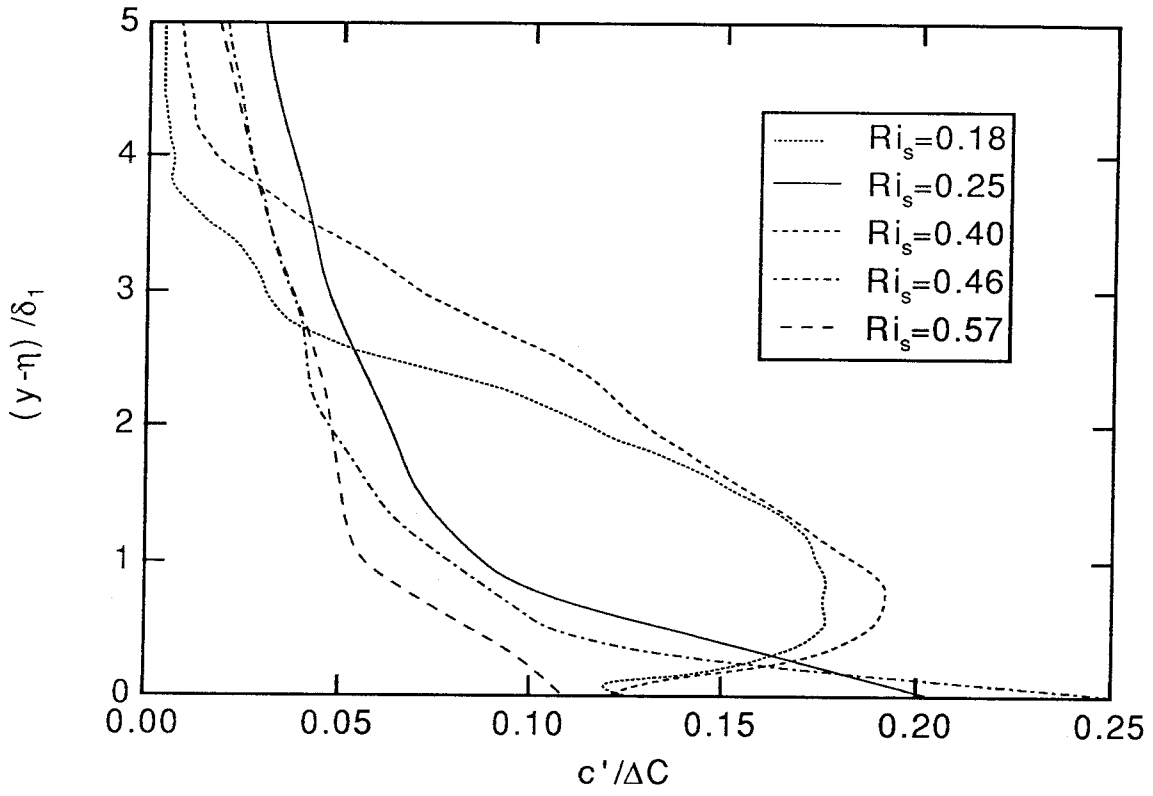

FIGURE 3.3.15. Rms concentration in a frame of reference moving with the interface. Values are from the upper layer.

A portion of a typical concentration-time trace is shown in figure 3.3.16. Here concentration is measured at the center of the upper layer and time is normalized by the large-scale time, U_1/h_1. The section from $tU_1/h_1=18.1$ to $tU_1/h_1=36.2$ corresponds to the false color image segment shown in figure 3.3.3.

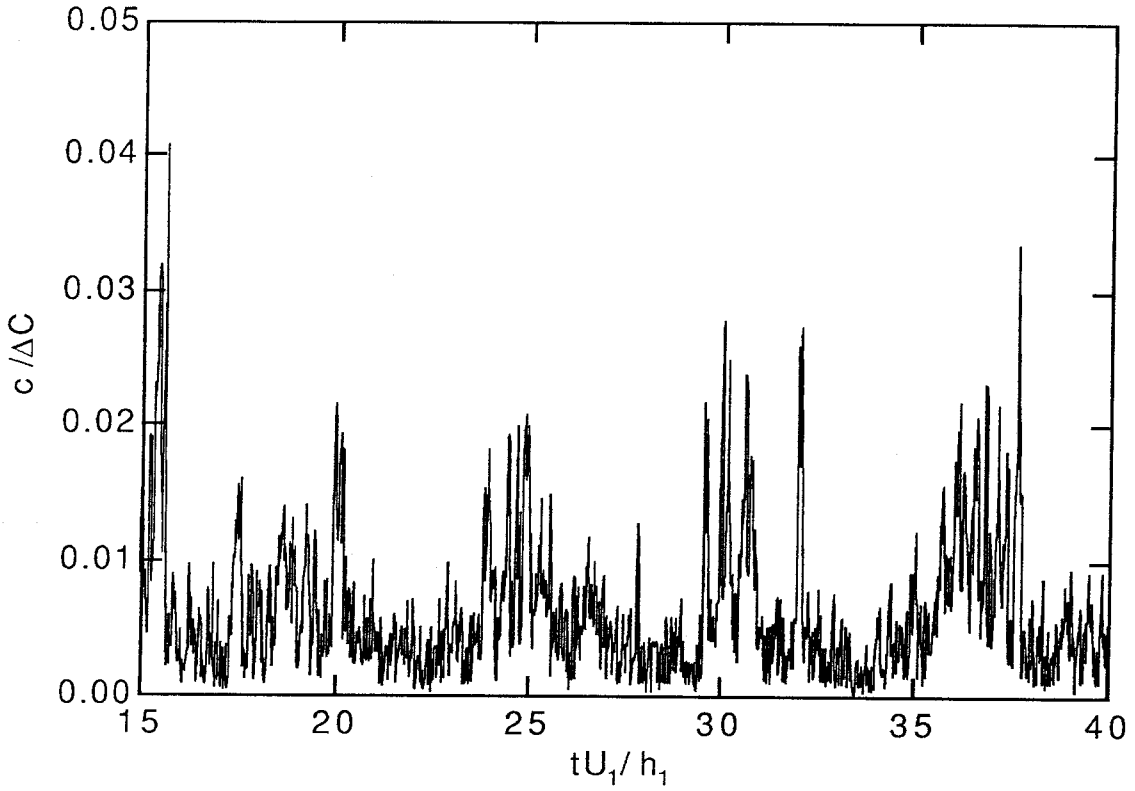

FIGURE 3.3.16. Concentration fluctuations at $(y-\eta)/h_1=0.5$ from experiment 13.

Probability distribution functions of dye concentration anomaly are shown in figures 3.3.17 and 3.3.18 (strictly speaking these are plots of 1-P, where P is the traditional probability distribution function). Plotted is the probability of finding fluid of concentration greater than the local mean concentration by an amount Γ. Measurements are taken a distance h/2 from the interface (in a frame of reference moving with the interface).

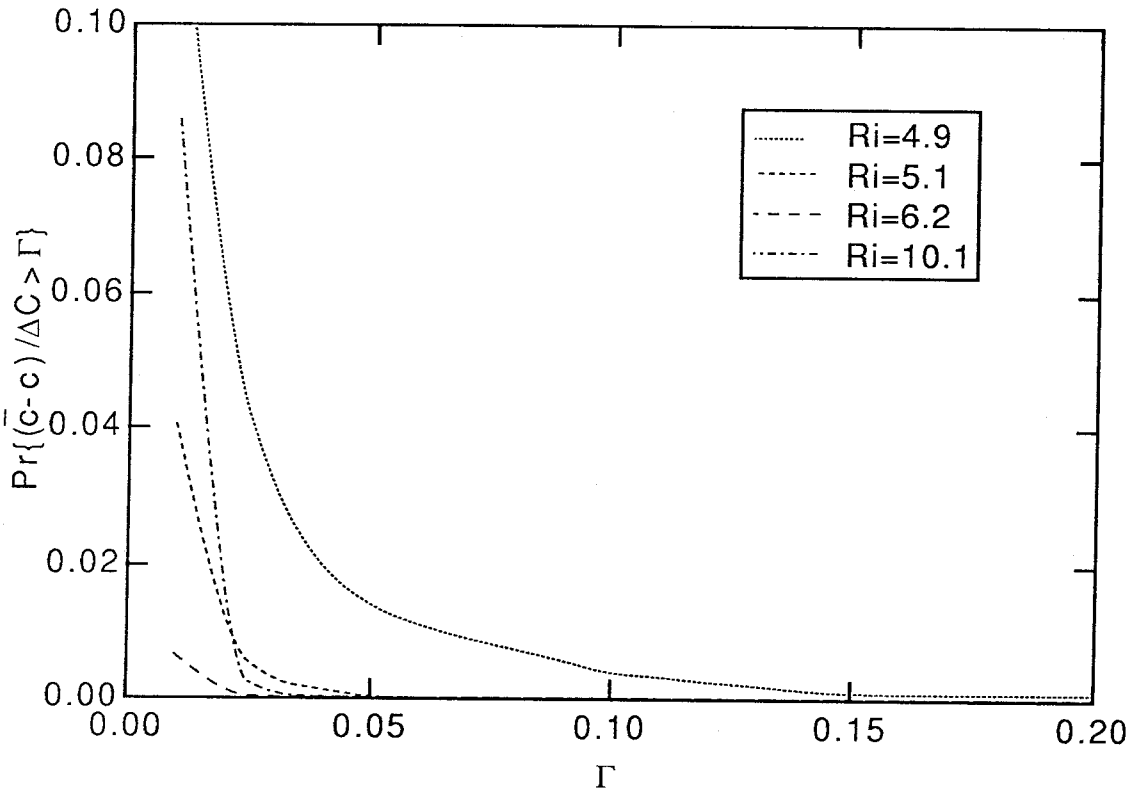

FIGURE 3.3.17. Probability distribution function of concentration anomaly. Measurements are taken below the interface at $(\eta\text{-}y)/h_0=0.5$.

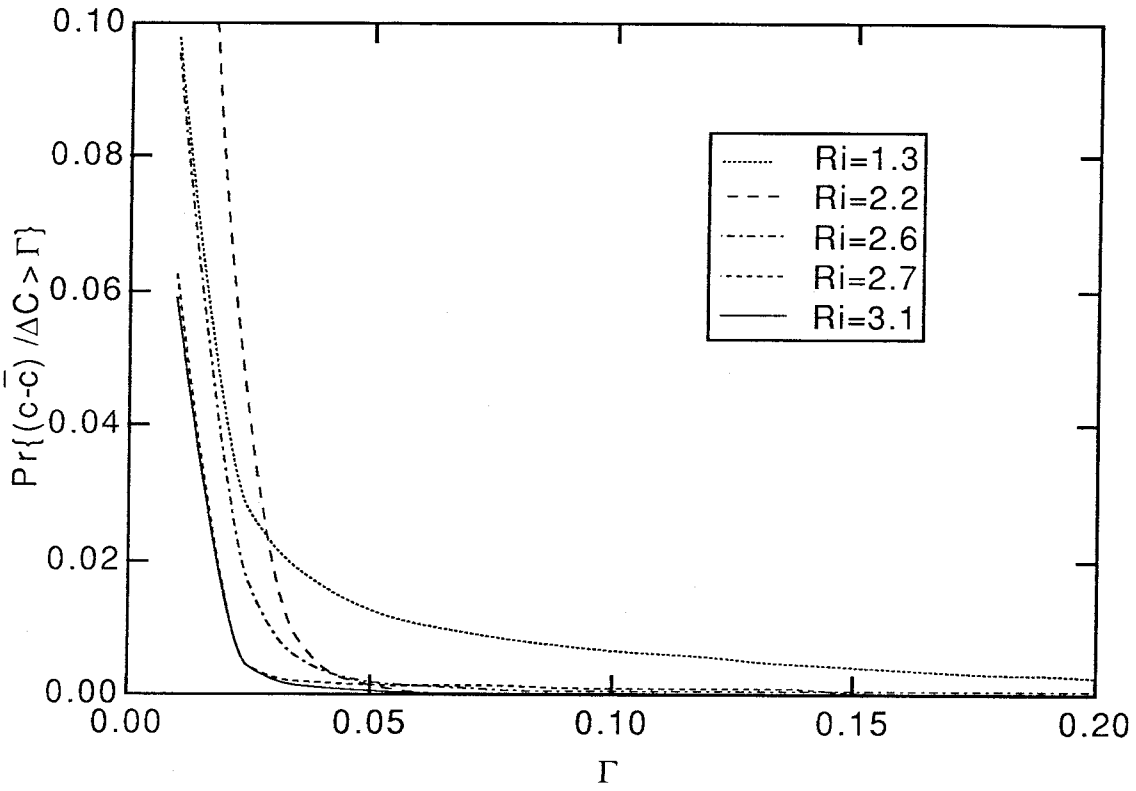

FIGURE 3.3.18. Probability distribution function of concentration anomaly. Measurements are taken above the interface at $(y-\eta)/h_1=0.5$.

The maximum (normalized) concentration anomaly is defined here as the concentration, Γ_m, for which

$$\Pr\left\{\frac{|c-\bar{c}|}{\Delta C}\right\} > \Gamma_m = K, \tag{3.3.1}$$

at $|y-\eta|/h=0.5$. I.e. the probability of finding concentration anomaly, $|c-\bar{c}|/\Delta C$, in excess of Γ_m is K, the probability threshold. Figure 3.3.19 shows Γ_m as a function of Ri for K=0.01. Error bars shown indicate maximum probable deviations from measured values. (There is some arbitrariness in the selection of K; however, variations in K do not significantly alter the nature of the results so long as K is sufficiently small.)

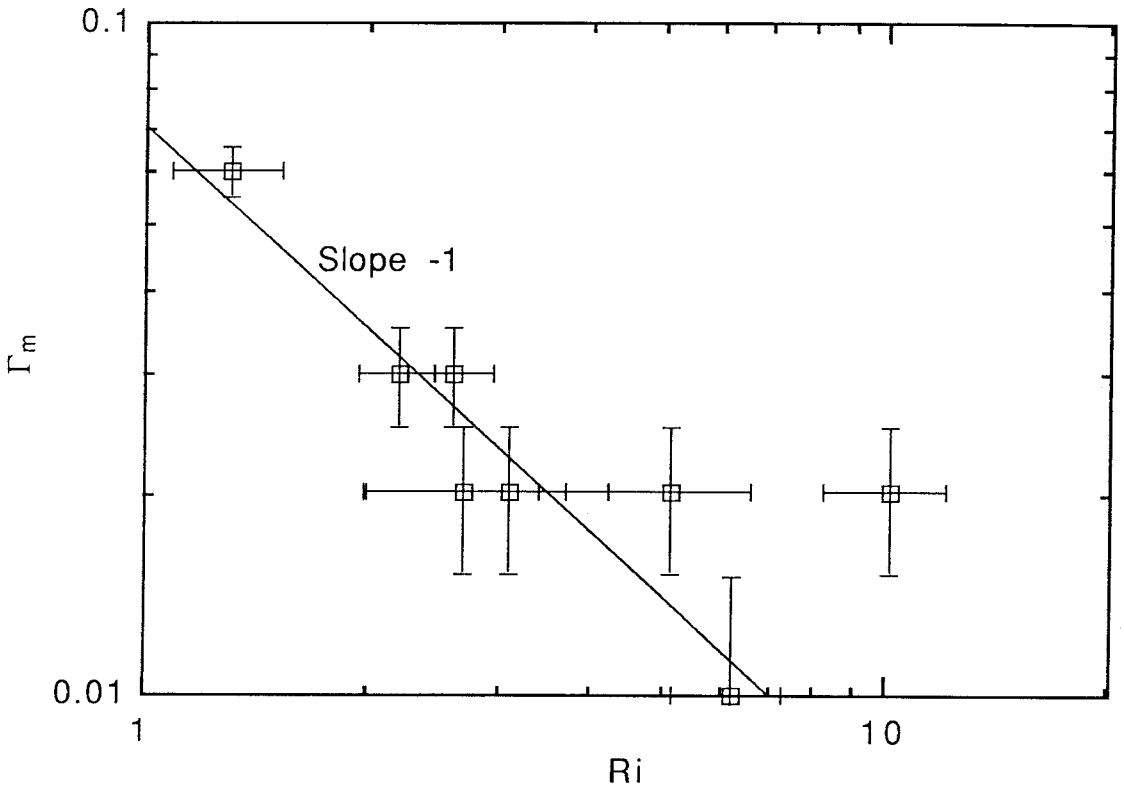

FIGURE 3.3.19. Maximum concentration anomaly. Here the probability threshold, K, is 0.01.

Power spectral density estimates for concentration fluctuations are shown in figure 3.3.20. These are determined as discussed in §3.2, except here the data are read in as overlapping segments of length 1024, rather than 2048 points. The concentration power spectral density is defined such that

$$\frac{\overline{c'^2}}{(\Delta C)^2} = \int_0^\infty E_c(f)df, \tag{3.3.2}$$

where E_c is the concentration power spectral density and f is the frequency. In figure 3.3.20 normalized spectra, $E_c u/c'^2 h$, are plotted versus normalized frequency, fh/u. Here u is the local mean streamwise velocity and c' is the (normalized) local rms concentration.

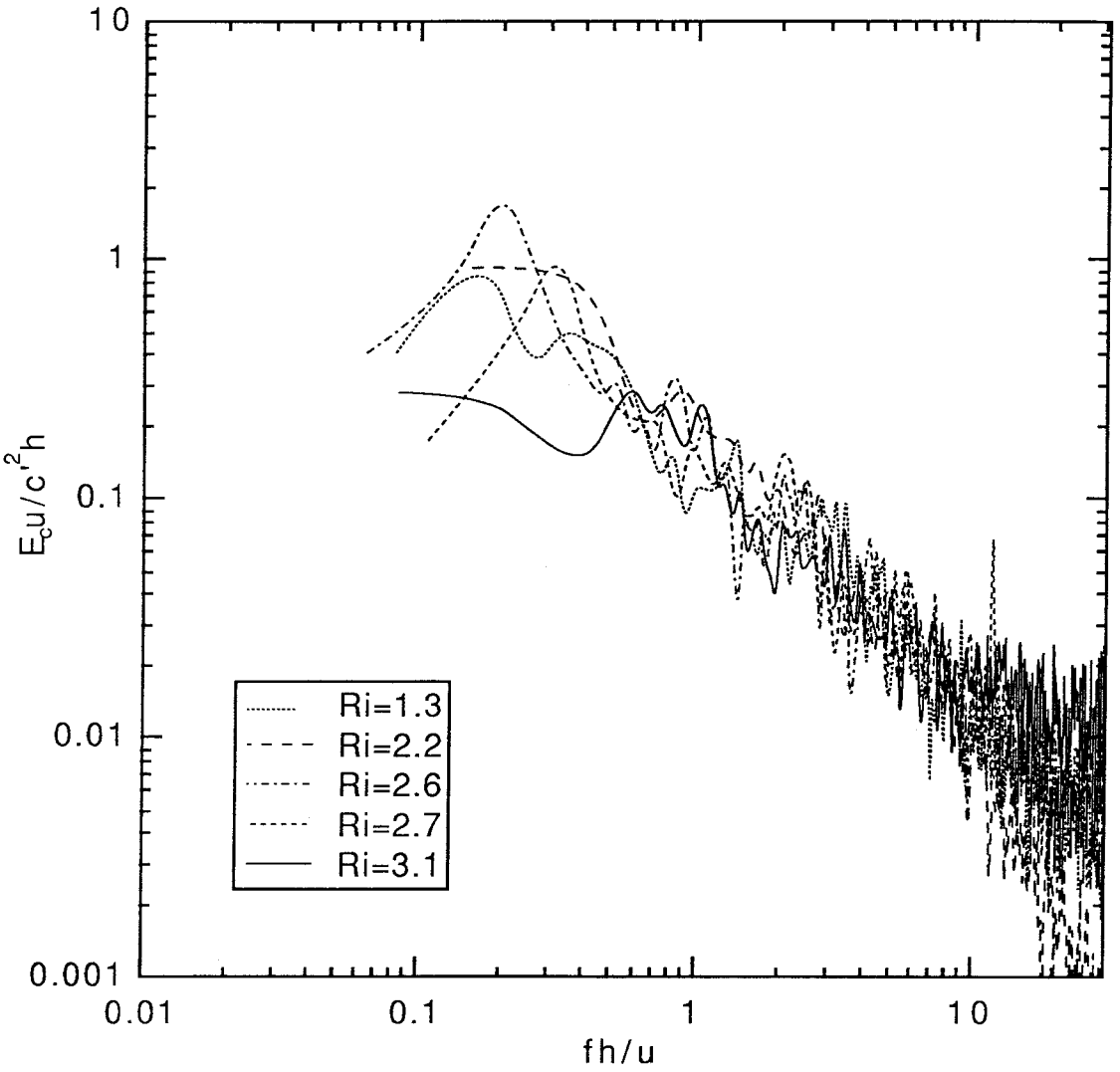

FIGURE 3.3.20. Power spectral density estimates for concentration.

Estimates are from the upper layer at $(\eta\text{-}y)/h_0=0.5$.

In figure 3.3.21 estimates of interfacial displacement power spectral density are shown, determined as for c'. Here the displacement power spectral density is defined such that

$$\overline{\eta'^2} = \int_0^\infty \Phi_\eta(f)df, \tag{3.3.3}$$

where η is the interface position and Φ_η is the power spectral density.

The interface position, $\eta(t)$, is defined as the vertical position where the concentration crosses the 50% threshold. I.e.

$$c(\eta(t) - \Delta y, t) \geq 0.5\Delta C, \tag{3.3.4}$$

and

$$c(\eta(t) + \Delta y, t) \leq 0.5\Delta C, \tag{3.3.5}$$

where Δy is the vertical distance between regions imaged by successive pixels. This, in itself, does not define $\eta(t)$ uniquely; in regions of mutivaluedness the following procedure is used. If η is single-valued at time t_0, then at time $t_0+\Delta t$ if $c(\eta(t_0),t_0+\Delta t) < 0.5\Delta C$ then $\eta(t_0+\Delta t)$ is the first position below $\eta(t_0)$ where c crosses the 50% threshold; if $c(\eta(t_0),t_0+\Delta t) > 0.5\Delta C$ then $\eta(t_0+\Delta t)$ is the first position above $\eta(t_0)$ where c crosses the 50% threshold.

Spectra are plotted for frequencies up to 2 Hz; beyond this, measurements are limited by spatial resolution of the imaging system.

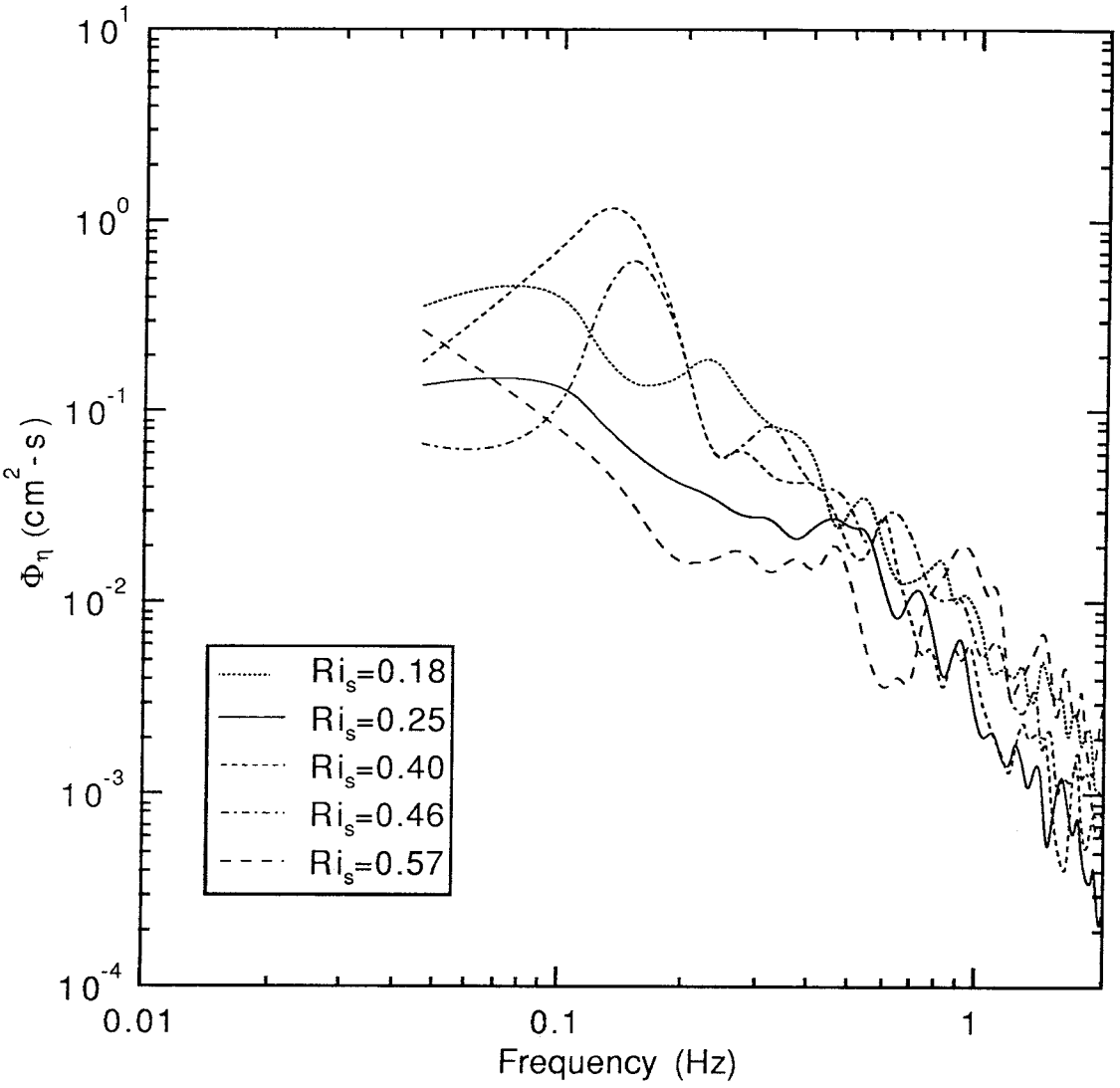

FIGURE 3.3.21. Power spectral density estimates for interfacial displacement.

Mean interfacial thicknesses, $\overline{\delta}$, are shown in figure 3.3.22. The interfacial thickness, $\delta(t)$, is defined as the vertical distance between the point below $\eta(t)$ where c first rises above $0.9\Delta C$ and the point above $\eta(t)$ where c first drops below $0.1\Delta C$.

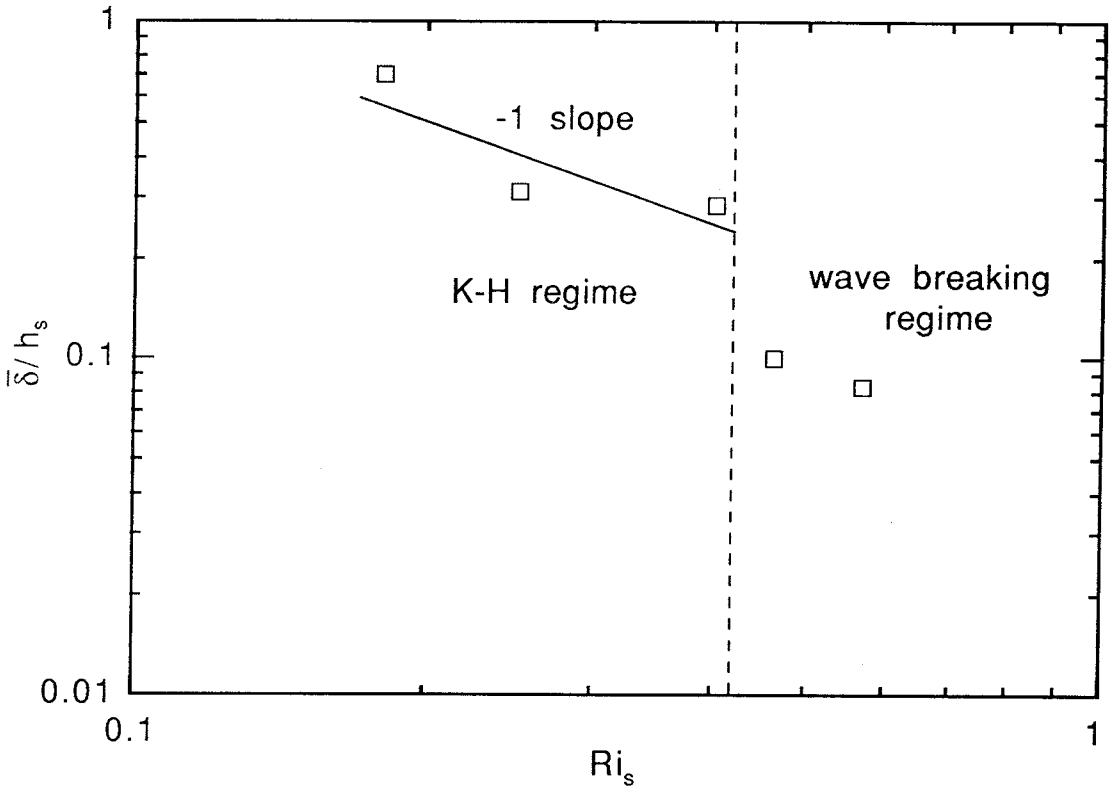

FIGURE 3.3.22. Mean interfacial thickness.

Finally, estimates of Ri_g in the interface are shown in figure 3.3.23 as a function of Ri_s. Here Ri_g is the mean gradient Richardson number defined as

$$Ri_g = \frac{N^2}{(\partial u / \partial z)^2}, \tag{3.3.6}$$

where

$$N = \left[\frac{-g}{\rho_1} \frac{\partial \overline{\rho}}{\partial z} \right]^{1/2} \tag{3.3.7}$$

is the Brunt-Väisälä frequency.

In the interface Ri_g may be approximated as

$$Ri_g \cong \frac{\Delta b h_s^2}{\overline{\delta}(\Delta U)^2}, \tag{3.3.8}$$

where $\Delta U=(U_0-U_1)$.

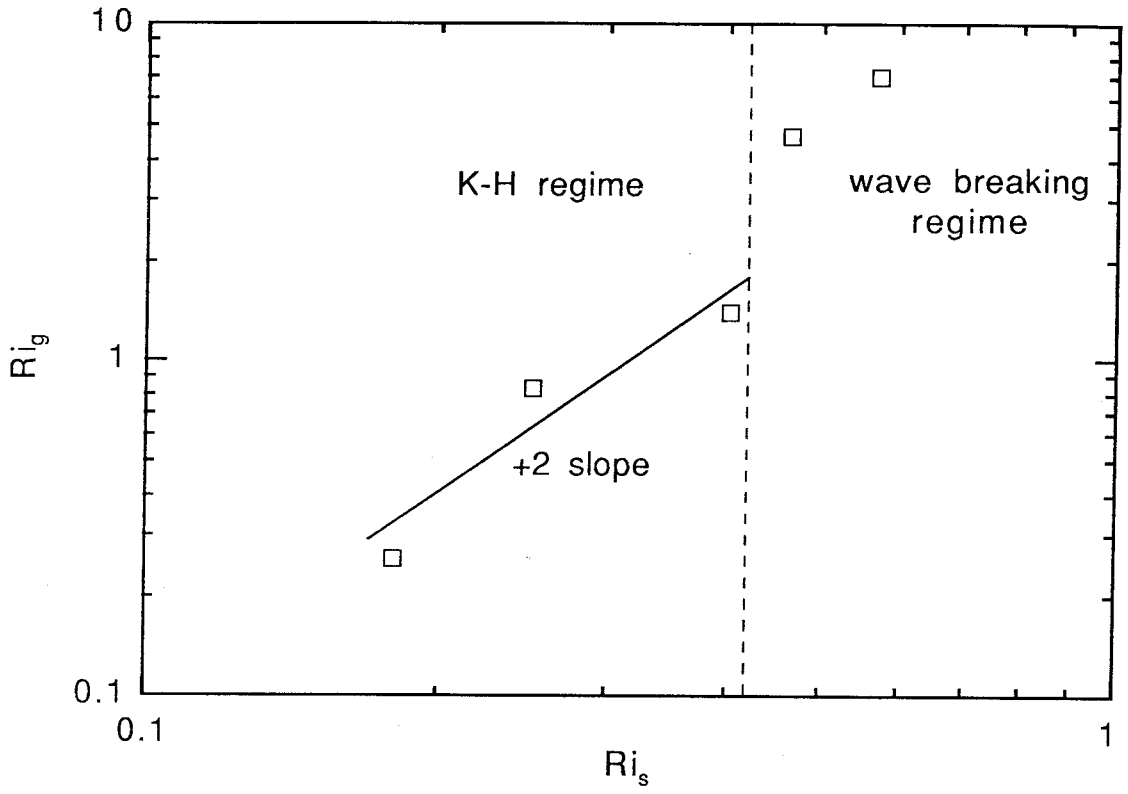

FIGURE 3.3.23. Mean gradient Richardson number in the interface.

CHAPTER 4

DISCUSSION OF RESULTS

4.1. Velocity Measurements

Motivated by the 'law of the wall' (see Clauser 1956) for turbulent flow over a rigid surface, Csanady (1978) suggests an analogous 'law of the interface' for turbulent flow over a sharp density interface with scaling

$$\frac{u - u_i}{u_*} = f(\frac{yu_*}{\nu_e}), \tag{4.1.1}$$

in a region very close to the interface, and

$$\frac{U - u}{u_*} = g(\frac{y}{h}), \tag{4.1.2}$$

some distance away. Here y is the distance from the interface, $u_*=\sqrt{\tau_i/\rho}$ is the interfacial shear velocity (τ_i is the interfacial stress), U is the free stream velocity, h is the boundary layer thickness, and ν_e is an 'effective viscosity' at the interface representing the transfer of momentum by both molecular diffusion and sheared interfacial waves.

The velocity data from this study have been cast in the forms (4.1.1) and (4.1.2), but difficulty in obtaining accurate estimates of u_* and the relative sparsity of data points has limited the analysis (a proper investigation of 4.1.1 and 4.1.2 requires considerably more data than obtained here). Crudely speaking though, the results are not inconsistent with a logarithmic profile near the interface, as suggested in the analysis of Csanady. The individual velocity profiles, however, do not collapse on a

single curve as in the 'law of the wall'. Csanady suggests that the 'effective roughness' in this case should depend on the interfacial wave field.

In the 'law of the interface' it is tacitly assumed that the buoyancy flux has negligible effect on the form of the velocity profile. To investigate this, appeal is made to results from Monin & Yaglom (1971) for the problem of a horizontally homogeneous boundary layer in the presence of a stabilizing heat flux. If the density interface is approximated as a rigid surface across which there is a stabilizing buoyancy flux, then Monin & Yaglom's analysis suggests that the influence of buoyancy should be small when $y/L \ll 1$. Here y is the distance from the interface, and L is the Monin-Obukhov length, given by

$$L = \frac{u_*^3}{kg\overline{\rho' v'}/\rho} \tag{4.1.1}$$

(k is the von-Kármán constant). Using results from Lofquist (1960), estimates of h/L in the experiments studied have been made; it is found that h/L ranges from about .05 to 0.3, which may not be small enough to completely neglect the effects of the buoyancy flux. However, an investigation of this is outside the scope of this study and henceforth it is assumed that any such effects are secondary insofar as mixing and transport at the interface are concerned.

Shown in figures 3.2.4 and 3.2.5 are profiles of mean velocity, normalized by U. Here U is not the preferred scaling velocity, but accurate estimates of u_* or U_{max} (the layer maximum velocity) could not be obtained. Since the ratio U_{max}/U is (presumably) higher in the lower layer than in the upper layer (the bottom layer has an additional boundary layer at the lower wall), normalized profiles above and below the interface cannot be directly compared. This is evidenced by the consistently higher values of normalized velocity below the interface than above. Viewing each layer

separately, the data collapse (within experimental error) is reasonable and no obvious trends with Ri are observed.

Rms velocity fluctuations are shown in figures 3.2.6 to 3.2.9, normalized by U. Normalized fluctuations are consistently greater below the interface then above, which may be attributed to the difference in U_{max}/U mentioned previously. (The lower wall boundary layer, however, does not appear to significantly influence velocity fluctuations near the interface; in figures 3.2.6 and 3.2.8 there is no discernable increase in velocity fluctuations at Ri=10.1, 219 cm downstream of the lower layer inlet, over those at Ri=5.1 and Ri=4.9, 30 cm downstream of the inlet.) Within the accuracy of the data, there appears to be an increase in u' and, to a lesser degree, in v' as the interface is approached, in qualitative agreement with the results of Grass (1971) for flow over a roughened floor in free surface channel flow.

The large increase in u' and v' in figures 3.2.6 and 3.2.8 immediately at the interface, however, is attributed to interfacial waves. It should be borne in mind that turbulent fluctuations and fluctuations induced by interfacial waves both contribute to rms velocities in figures 3.2.6 to 3.2.9. Ideally, if a spectral gap exists between the energy containing interfacial waves and the turbulence, and if the waves and turbulence are statistically independent, then effective filtering can be employed to separate them (Lumley & Panofsky, 1964). Although the lowest mode seiching motions (f ~ .01 Hz to .1 Hz) may be separated from turbulent fluctuations, higher frequency interfacial waves (presumably generated by turbulent eddy impacts on the interface) have frequencies comparable to those of the turbulent fluctuations, making their separation difficult.

To estimate the contribution to the velocity variance from wave-induced fluctuations, results from Phillips (1966) for the case of two irrotational, homogeneous

layers separated by a sharp interface may be used. Phillips' results may be assumed approximately valid away from the interface, insofar as estimates of magnitudes of velocity fluctuations are concerned, if the zone of high shear is confined to a small region about the interface.

In his analysis, Phillips finds that lowest mode waves of wavelength significantly greater than the thickness of the interface are dispersive with frequency

$$\omega^2 = \Delta b k[\coth kd + \coth k(H-d)]^{-1}. \qquad (4.1.4)$$

Here k is the wave number, d is the upper layer depth, H-d is the lower layer depth, and Δb is the buoyancy difference. The resultant amplitudes of velocity fluctuations induced by a single-frequency wave are shown in figures 4.1.1 and 4.1.2 at five different wave frequencies. Typically, the lowest frequency interfacial waves resolved in the experiments have wavenumber about kd=0.5 so that, assuming most of the wave energy is in low frequency waves, estimates of wave-induced fluctuations a distance h/2 above the interface give $u'/(u_i-U_1) \sim 0.02$ to 0.04 and $v'/(u_i-U_1) \sim 0.01$ to 0.02. Based on these estimates, measured velocity fluctuations in figures 3.2.6 to 3.2.9 would be reduced by about 10% to 15% in the absence of interfacial wave activity. However, immediately at the interface, contributions from high frequency waves may be considerable, as evidenced in figures 3.2.6 and 3.2.8.

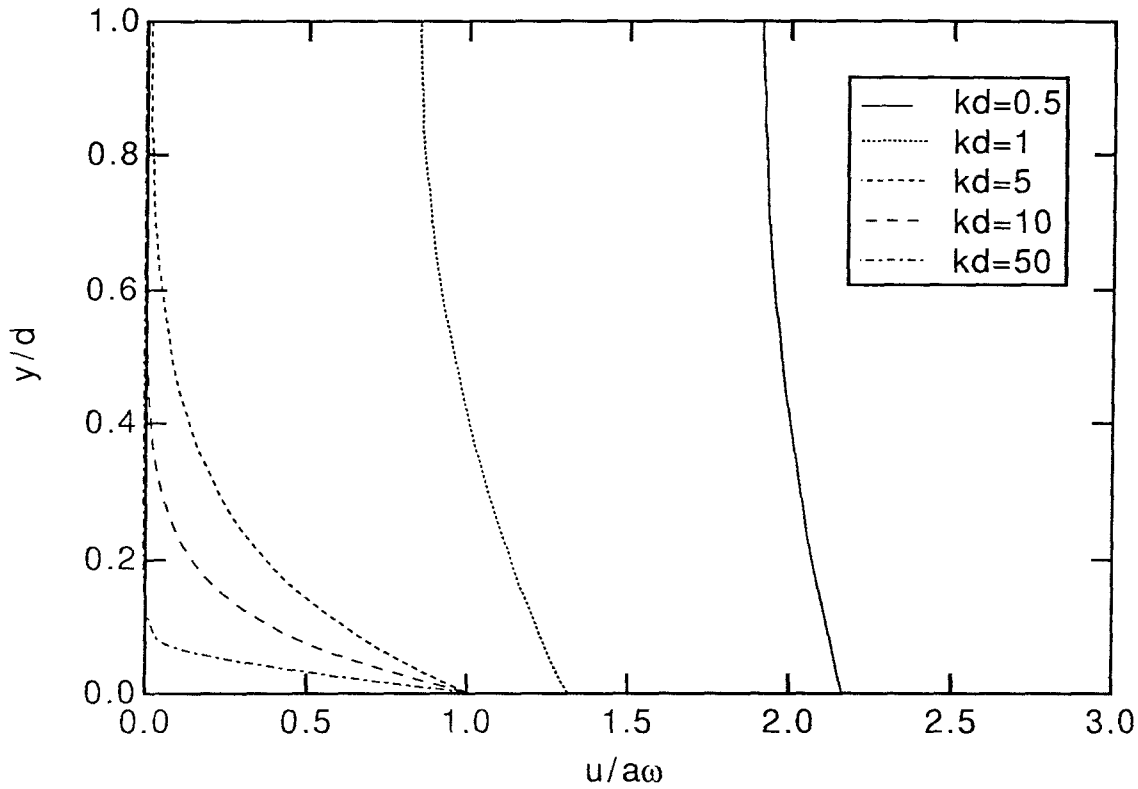

FIGURE 4.1.1. Horizontal velocity fluctuations induced by a single frequency interfacial wave.

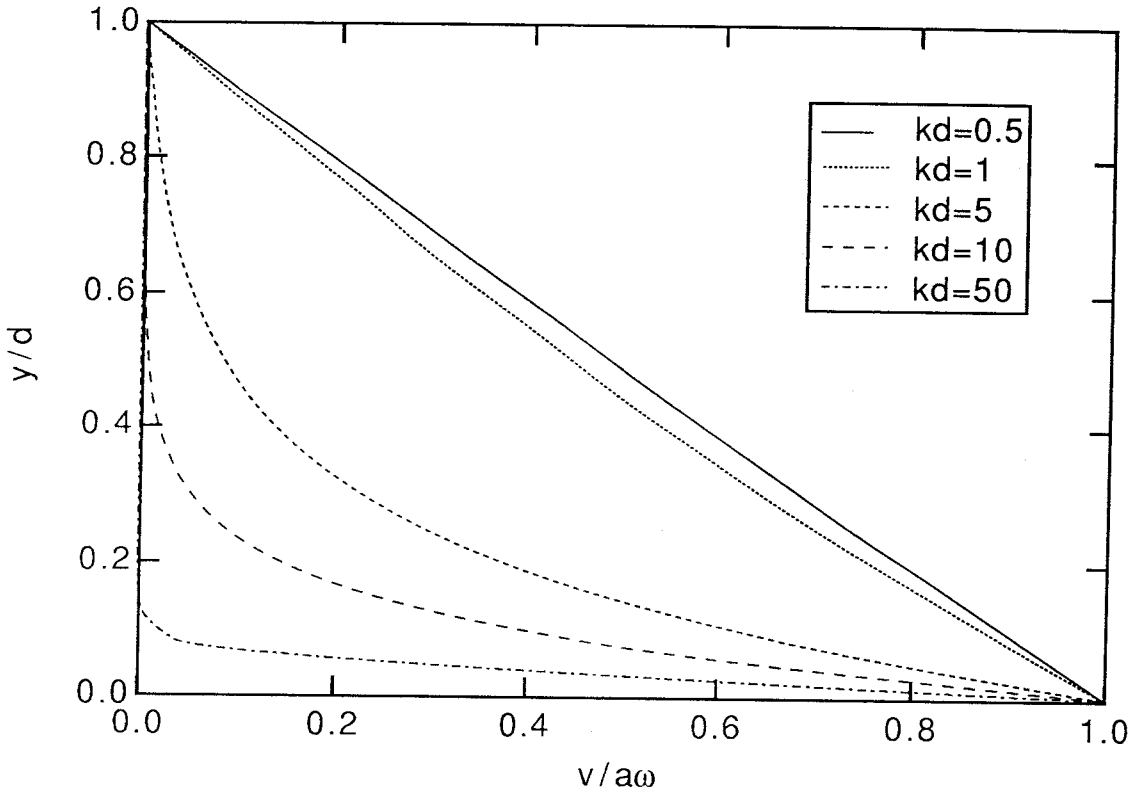

FIGURE 4.1.2. Vertical velocity fluctuations induced by a single frequency interfacial wave.

In figures 3.2.10 to 3.2.13 inertial (large-scale) scaling is used to normalize the velocity spectra. The lowest frequency oscillations (fh/u of order 10^{-1}) in the spectra are believed due to interfacial wave induced fluctuations. (The lowest frequency oscillations in the flume, however, are not resolved; the period of the lowest mode seiching motion in the flume is typically about 100 seconds, estimated using results from Turner 1973 for an idealized two-layer narrow channel, which is about 5 times greater than the longest period oscillations resolved.) Higher frequency fluctuations in the spectra are believed due to both waves and turbulence. The existence of an inertial subrange is unlikely in these spectra as Reynolds numbers are relatively small† (Tennekes & Lumley 1972); and, in light of the relatively high noise floor, any suggestion of such would be highly speculative.

† Although Re is relatively small, turbulent flow is expected. In a similar flow, Keulegan (1949) finds that the flow becomes turbulent (except at the interface) for Re greater than about 1800 (based on the mean layer velocity and total layer depth); similarly determined Reynolds numbers in this study are typically several times greater than this. Larger Reynolds numbers are of course desirable, but necessitate a larger facility.

4.2. Concentration Measurements

False color images of concentration such as those shown in figures 3.3.3 to 3.3.8 provide valuable insight into mixing and transport at the interface. Through the study of such images a number of features are found common to all of the flows. These are first detailed and following this, observed variations in interfacial mixing are discussed.

In each of the 5 experiments, entrainment of fluid appears to be due to large-scale eddies which scour fluid from the interface into adjacent layers.† Once in an adjacent layer, interfacial fluid becomes permanently incorporated through the combined action of turbulent straining (stretching marked fluid into thin strands) and molecular diffusion. If the scoured fluid is too heavy, though, it appears to fall back to the interface (is not incorporated), resulting in an interfacial disturbance. In no experiment is it observed that pure unmixed fluid is entrained directly from one layer to the other; it is always fluid from the interface of intermediate concentration and density that is entrained.

Rough estimates show that the length (in time) of a scouring 'event' is typically $\sim \tau_L$ to $2\tau_L$ and the time between events is typically $\sim 5\tau_L$ to $10\tau_L$, independent of Ri. Here $\tau_L = h/U$ is the large scale time. Also, in all cases, scouring events appear to be uncorrelated (in time) with the occurrence of local interfacial instabilities.

---

† In figures 3.3.3 to 3.3.5 scouring events are more clearly observed above the interface than below. This is an artifact of the asymmetric color thresholding and not a manifestation of a physical asymmetry. A component of noise in the concentration measurements (due to photodiodes, amplifiers, etc.) is proportional to the signal, so that absolute errors above the interface are considerably less than those below. Since it is the difference between the instantaneous concentration and the local mean that is of interest, the relative error in measuring these small deviations is much smaller above the interface than below. Asymmetric color thresholding is employed so that noise in the lower layer is not unduly highlighted.

Balancing the sharpening action of scouring eddies is production (local mixing) by interfacial instabilities and molecular diffusion. The dominant thickening mechanism is found to depend on the mean shear Richardson number, Ri_S. When Ri_S is below about 0.4 to 0.45, large-scale K-H instabilities are observed at the interface. When Ri_S is greater than this, K-H instabilities are no longer observed and interfacial wave breaking appears to dominate the thickening process. The local (in time) variation in interface thickness may be attributed to the random nature of the local scouring events and interfacial instabilities.

In figure 3.3.4 (Ri_S=0.25), K-H instabilities at various stages of growth can be clearly seen (in figure 3.3.7 a close-up of one of these in its initial stages of growth is shown). In figure 3.3.5 (Ri_S=0.17), more intense and more frequently occurring K-H type shear instabilities are observed (a close-up of the more intense mixing region is shown in figure 3.3.8). At Ri_S=0.40 (not shown) K-H instabilities are also observed. The K-H instabilities in these experiments appear to be cyclically generated: they form, roll-up into billows, grow, and collapse, and after some period of time they form again. The evolution of the K-H instabilities and their cyclic nature is discussed in §5.1.

In figure 3.3.4 K-H billows are markedly asymmetric with respect to the density interface. In this case, billows form almost entirely below the center of the interface and the upper half of the interface remains remarkably sharp. Such asymmetries can be induced by a displacement between the density interface and the region of maximum shear (Lawrence, Browand & Redekopp 1991). In experiment 4 such an asymmetry likely exists since the flow beneath the interface is non-turbulent.

In figure 3.3.3 (Ri_S=0.46) K-H instabilities are no longer observed; the dominant thickening mechanism now appears to be interfacial wave breaking, as

discussed in §5.1. At Ri_S=0.57 wave breaking also dominates interfacial mixing (a close-up of a wave breaking event at Ri_S=0.57 is shown in figure 3.3.6).

The examination of false color images has aided the extraction of quantitative information from concentration measurements. Quantitative results shown in figures 3.3.9 to 3.3.23 are now discussed.

Profiles of normalized concentration anomaly, $|c - c_\infty| / \Delta C$, away from the interface are shown in figure 3.3.9. On dimensional grounds (assuming buoyancy effects away from the interface are small) it may be expected that

$$\frac{|c - c_\infty|}{\Delta C} = \frac{u_e}{u*} f\left[\frac{y - \eta}{h}\right], \tag{4.2.1}$$

where $u*$ is the interfacial shear velocity. If (4.2.1) is valid then profiles in figure 3.3.9 suggest $u_e/u*$ does not depend simply on Ri. The model developed in §5 suggests in this case that entrainment depends on combinations of parameters from both layers. If it is assumed that $u*$ is proportional (approximately) to $|U - u_i|$ then concentration profiles in figure 3.3.9 are in qualitative agreement with estimates for entrainment based on the model results (except for the case of experiment 11 in which $u*/|U - u_i|$ may be increased due to greater surface deformations).

Profiles of mean concentration near the interface are shown in figures 3.3.10 and 3.3.11. In figure 3.3.10 the zone of rapidly varying concentration is confined to a region about one interfacial half-width from the interface for Ri_S=0.46 and 0.57 (wave breaking dominated mixing), and to a region 3 to 4 interfacial half-widths from the interface for Ri_S=0.18, 0.25 and 0.40 (K-H dominated mixing). In the former case, wave breaking events have relatively small vertical scale and occur relatively infrequently so that broadening of mean concentration profiles is minimal. In the latter

case, K-H instabilities have a larger vertical scale and result in greater variations in interfacial thickness. In comparing profiles in figures 3.3.10 and 3.3.11, asymmetries are observed which may be attributed to a displacement between the center of the density interface and the location of maximum shear.

Since concentration is measured in a frame of reference moving with the interface, profile spreading due to interfacial waves is avoided. However, local interfacial instabilities and eddy scouring can result in instantaneous profiles somewhat different from their corresponding mean profiles, as seen in figure 3.3.12.

Figure 3.3.13 shows profiles of rms concentration fluctuations away from the interface. Here concentration fluctuations are presumably due to strands of interfacial fluid convecting in nearly homogeneous unmixed fluid, as observed in figures 3.3.3 to 3.3.5. Drawing further conclusions from these profiles is difficult due to the relatively high noise levels.

Profiles of rms concentration fluctuations near the interface are shown in figures 3.3.14 and 3.3.15. Note the markedly different profile forms in figure 3.3.14 for Ri_S=0.18, 0.25 and 0.40 (K-H regime) compared with those for Ri_S=0.46 and 0.57 (wave breaking regime). The off-axis maxima in the former case are considerably greater than those in the latter, as are the fluctuations out to about 4 interfacial half-widths from the interface. Concentration fluctuations are relatively low, however, at Ri_S=0.25 compared with those at Ri_S=0.18 and 0.40, which may be attributed to the absence of eddy scouring beneath the interface at Ri_S=0.25 (experiment 4). Relatively high values of c' in the interface are manifestations of the limited spatial resolution there. When the interface is very sharp, the highest concentration gradient region may span only 3 to 4 pixels so there is some variability in the concentration at $y=\eta$. c' measured in a frame of reference moving with the interface is therefore artificially high

there. In comparing figures 3.3.14 and 3.3.15, there are asymmetries in the rms profiles which may be attributed to velocity profile asymmetries (with respect to the density interface) and differences in the intensity of eddy scouring from above and below.

Figure 3.3.16 shows a typical concentration-time trace, measured a distance h/2 above the interface. Here eddy scouring events are manifested as regions of relatively high fluctuations in concentration, typically spanning 1 to 2 large-scale times, and spaced by about 5 to 7 large scale times. During a scouring event, the concentration signal is highly intermittent; regions of scoured fluid of intermediate concentration are interspersed between regions of nearly pure unmixed upper layer fluid. Note in this case that the highest scalar concentration observed is only about 4% of that in the lower layer.

Probability distributions of scalar concentration anomaly are shown in figures 3.3.17 and 3.3.18. It is expected that the scalar flux depends on combinations of parameters from both sides of the interface (see §5.1) so it is not surprising that distribution functions do not display a simple Ri dependence. The maximum concentration anomaly, Γ_m, however, is expected to depend solely on Ri. Figure 3.3.19 shows Γ_m as a function of Ri (using a probability threshold, K, of 0.01), and with the exception of one point at Ri=10.1 (whose error may be underestimated), the data are well represented by $\Gamma_m \sim Ri^{-1}$.

In figure 3.3.20 concentration power spectra are shown, normalized using inertial (large-scale) scaling. Here the spectra collapse quite well, suggesting that large-scale disturbances scale with h and convect with the local mean velocity, u, independent of Ri.

Interfacial displacement spectra are shown in figure 3.3.21. A variety of mechanisms may be active in generating disturbances contributing to these spectra.

Low-frequency oscillations may be generated during start-up and persist through an experiment;† low and intermediate frequency oscillations may be induced by the roll-up and collapse of large-scale K-H billows (when Ri_s is sufficiently small); and high frequency waves may be generated by random pressure fluctuations induced by turbulent eddies impacting on the density interface (Phillips, 1966), or possibly by the feedback mechanism discussed by Lighthill (1962) for waves whose phase speed matches the fluid convection velocity close to the interface.

In figure 3.3.22 mean interfacial thicknesses are shown versus Ri_s. The model developed in §5.1 predicts $\delta/h_s \sim Ri_s^{-1}$ in the K-H regime†† and

$$\delta \sim \left[\frac{U_0 / \sqrt{Ri_0} + U_1 / \sqrt{Ri_1}}{U_0 / h_0 + U_1 / h_1} \right] \tag{4.2.2}$$

in the wave breaking regime. The data shown are consistent with these results.

In figure 3.3.23 the mean gradient Richardson number, Ri_g, is shown versus the mean shear Richardson number, Ri_s. In the K-H dominated regime, the data are consistent with $Ri_g \sim Ri_s^2$, which follows directly from $\delta/h_s \sim Ri_s^{-1}$ (see 3.3.8). In order for K-H instabilities to be active, Hazel (1972) suggests that the local gradient Richardson number (in the interface) must be less than about 0.2 to 0.25. (The critical value for instability depends on the precise forms of the velocity and density profiles and the location of boundaries.) In flows where K-H instabilities occur in a cyclic manner, this criterion may need only be met for a short period of time, so that the time-averaged gradient Richardson number, Ri_g, may be considerably larger than 0.25.

---

† It is believed, however, that long-period waves play no role in mixing and transport processes at the interface; it is intermediate (K-H) and high frequency waves which become locally unstable and lead to interfacial mixing.

†† Here the velocity gradient thickness, h_s, is artificially introduced. It is included merely for convenience to exhibit the differing forms for δ in the two mixing regimes.

An ad hoc criterion for (cyclic) instability in this case may be $Ri_g < Ri_{gc}$, where Ri_{gc} is the maximum value of Ri_g for which the local (in time) Richardson number can drop below about 0.2 to 0.25. Since Ri_g is determined by Ri_s (in the K-H regime) this may be given equivalently as $Ri_s < Ri_{sc}$ (here experiments suggest $Ri_{sc} \sim$ 0.4 to 0.45).

CHAPTER 5

ENTRAINMENT MODEL

5.1. Model Development

Consider two fluid layers of density ρ_1 and $\rho_1+\Delta\rho$, velocity (free stream) U_1 and U_0 and (boundary layer) thickness h_1 and h_0, respectively, separated by an interface of thickness δ, as shown below. The layer Reynolds numbers are assumed sufficiently large that the flow is turbulent, except very close to the interface where buoyancy forces are appreciable.

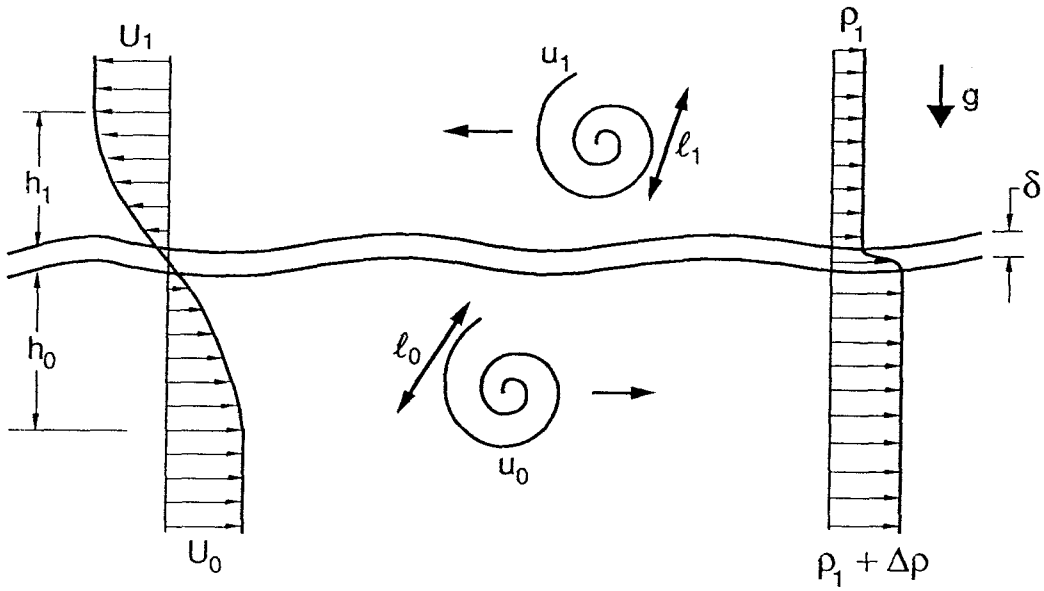

FIGURE 5.1.1. Schematic of two-layer entraining flow.

Consider turbulent eddies† of size ~ l and fluctuating velocity scale ~ u convecting past the interface with mean velocity ~ U. It is assumed that large-scale eddies contain the bulk of the turbulent kinetic energy so that $u \sim \left[\overline{u'^2} + \overline{v'^2} + \overline{w'^2}\right]^{1/2}$, where u', v', and w' are, respectively, the x, y, and z components of the fluctuating velocity (here and throughout the symbol ~ denotes proportionality). It is understood that distributions about characteristic scales are implied in the scaling arguments; it is assumed that distributions do not change significantly with variations in Reynolds number or buoyancy flux (i.e. h/L is small, where L is the Monin-Obukhov length, given by 4.1.1). The average spacing between entraining eddies is taken to scale with the eddy size so that at a fixed position, $\mathbf{x_0}$, near the interface, the frequency of eddy interaction (from one side of the interface) is given by

$$f_e \sim \frac{U}{l}, \tag{5.1.1}$$

and the average duration of an eddy interaction is

$$t_i \sim \frac{l}{U}. \tag{5.1.2}$$

These assumptions are supported by experimental observations which suggest that scouring 'events' are spaced by about 5h/U to 10h/U and have duration h/U to 2h/U, independent of Ri. During an interaction, the influence of an eddy extends, on average, a distance

$$d_i \sim u t_i$$

into the interface, or using (5.1.2),

† An 'eddy' is loosely defined here as a compact, coherent turbulent formation (inhomogeneity). It is assumed that large-scale eddies are responsible for the bulk of the entrainment and henceforth 'eddy' refers to a large-scale eddy.

$$d_i \sim \frac{ul}{U}. \tag{5.1.3}$$

Assuming that during an eddy interaction interfacial fluid is accelerated to velocity ~ u in the vertical, then in time t_i this fluid travels a vertical distance

$$y_i \sim ut_i$$

or, using (5.1.2),

$$y_i \sim ul / U.$$

An eddy will interact with the interface for a time

$$t_e \sim \frac{l}{u} \tag{5.1.4}$$

(eddy turnover time), and will effectively scour fluid over a distance ~ Ul/u along the interface. From conservation of energy it is required that the kinetic energy of an eddy be greater than or equal to the work done in lifting interfacial fluid; this then requires that Ri < c, where c is a constant between about 10 and 100. If Ri > c then the spacing between entraining eddies and the distance over which they scour may depend on Ri. For the purposes of this discussion it is assumed Ri < c.

It may be assumed that interfacial fluid is permanently entrained if it resides in the layer long enough to become 'incorporated', the time taken scaling with the eddy turnover time, t_e.† Scoured interfacial fluid whose residence time is less than this falls

† The incorporation process consists of stretching fluid elements into fine strands so that molecular diffusion can act effectively. Broadwell & Mungal (1991) suggest that the time required to stretch the interface of a large-scale 'blob' of passive scalar to scales on the order of the Kolmogorov microscale scales with l/u. The additional time required for local straining to further reduce the scale of the interface (to the Batchelor scale) and for subsequent molecular diffusion is negligible compared with l/u. Thus the total time for 'incorporation' scales with l/u.

back to the interface and is not entrained.

Consider an element of fluid of density $\rho_1+\theta\Delta\rho$ (θ ranging from 0 to 1) scoured from the interface and accelerated to velocity ~ u in the vertical. Upon being scoured, the fluid element is subject to a gravitational force ~ $\Gamma\Delta\rho g$ acting toward the interface (here Γ is the concentration anomaly, defined such that if fluid is scoured from above, $\Gamma=\theta$, and if fluid is scoured from below, $\Gamma=1-\theta$). In the absence of turbulent motions, the time that the fluid element resides in the layer is given by

$$t_a \sim \frac{2u}{\Gamma\Delta b}. \tag{5.1.5}$$

For permanent entrainment it is necessary that t_a be greater than t_e which places an upper bound on Γ, for permanent entrainment, given by

$$\Gamma_m \sim \frac{u^2}{\Delta b l}. \tag{5.1.6}$$

It is convenient in flows of this type to define an entrainment velocity, u_e, as the equivalent volume of adjacent layer fluid incorporated into a layer per unit area per unit time. For convenience, u_e will henceforth denote the one-way entrainment from lower to upper layer and all unsubscripted symbols will refer to upper layer variables. (All results apply equally to the reciprocal case of one-way entrainment from below.) The entrainment velocity at $\mathbf{x_0}$ is given by

$$u_e \sim f_e \int_0^{d_m} \Gamma(\xi)d\xi, \tag{5.1.7}$$

where d_m is the maximum depth into the interface fluid may be drawn from and permanently entrained. Assuming Γ is slowly varying, except in a narrow region near the center of the interface, this gives

$$u_e \sim f_e \delta \Gamma_m . \tag{5.1.8}$$

Under this assumption it also follows that

$$d_m \sim \delta . \tag{5.1.9}$$

Substituting (5.1.6) and (5.1.1) into (5.1.8) yields

$$E \sim \frac{\delta}{l}\left(\frac{u^2}{\Delta b l}\right), \tag{5.1.10}$$

where $E=u_e/U$. (If the interface velocity, u_i, is non-zero then U is replaced by $|U-u_i|$.) It then remains to find δ/l.

The mean interface thickness, δ, is now determined by considering a balance between eddy scouring (sharpening) and interfacial instabilities and molecular diffusion (thickening). Three interfacial mixing regimes are considered, classified as: (1) diffusion dominated, (2) wave breaking dominated, and (3) Kelvin-Helmholtz (K-H) dominated.

Case 1: Diffusion Dominated Interface

When the stability of the interface is so great that interfacial instabilities rarely, if ever, occur, then the thickening of the interface is due primarily to molecular diffusion. In this case, the rate of spreading of the interface (in the absence of eddy scouring) is given by $d\delta/dt \sim \kappa/\delta$, where κ is the molecular diffusivity of the stratifying scalar. The volume gained per unit area per unit time, u_{GD}, by the interface is then given by

$$u_{GD} \sim \frac{\kappa}{\delta} C, \tag{5.1.11}$$

where C is the area of the (distorted) interface divided by its projection on the horizontal plane (it is assumed here that $C \sim 1$, due to the high stability of the interface).

The volume lost from the interface per unit area per unit time, due to eddy scouring, is given by

$$u_L \sim d_{m0} f_{e0} + d_{m1} f_{e1},$$

and using (5.1.9) and (5.1.1) this gives

$$u_L \sim \delta \left[\frac{U_0}{l_0} + \frac{U_1}{l_1} \right]. \tag{5.1.12}$$

Assuming an equilibrium state, $u_L \sim u_{GD}$, the equilibrium interface thickness is given by

$$\delta_{eD} \sim \frac{\kappa^{1/2}}{\left[\frac{U_0}{l_0} + \frac{U_1}{l_1}\right]^{1/2}}. \tag{5.1.13}$$

Assuming $l \sim h$ (supported by experimental observations which suggest $t_i \sim h/U$ to $2h/U$, independent of Ri), and $u \sim U$ (which follows from $u \sim u_*$, assuming u_*/U does not vary appreciably with Ri, Re, or Pe), substituting (5.1.13) into (5.1.10) yields

$$E \sim \left(\frac{U^2}{\Delta b h}\right)\frac{1}{h}\frac{\kappa^{1/2}}{\left(\frac{U_0}{h_0} + \frac{U_1}{h_1}\right)^{1/2}}. \tag{5.1.14}$$

In the simpler case when fluid on only one side of the interface is entraining, this reduces to

$$E \sim \left[\frac{U^2}{\Delta b h}\right]\left[\frac{\kappa}{Uh}\right]^{1/2}, \tag{5.1.15}$$

or

$$E \sim Ri^{-1}Pe^{-1/2}. \tag{5.1.16}$$

Case 2: Wave Breaking Regime

When the stability of the interface is such that large-scale K-H instabilities cannot occur, but finite-amplitude waves can become gravitationally unstable (upon interacting with the mean shear) and break, then thickening of the interface is dominated by wave effects.

It may be assumed that waves generated with sufficiently large aspect ratio, a/λ, (a is the initial wave amplitude and λ its wavelength) are distorted relatively quickly by the mean shear so that wave amplitudes and wavelengths at the time of breaking are not significantly different from initial values. (This is motivated by results from Frankignoul 1972 in a similar flow.) If an eddy generates a disturbance of wavelength $\lambda \sim Ul/u$ with energy proportional to the kinetic energy of the eddy, then the wave amplitude, $a \sim u\sqrt{lu/\Delta bU}$ (supported by experimental results from Narimousa & Fernando 1987). In this case, the frequency of wave breaking scales with the frequency of wave generation ~ f_e, and the volume gained per unit area per unit time by the interface is

$$u_{GB} \sim [f_{e0}u_0\sqrt{l_0u_0 / \Delta bU_0} + f_{e1}u_1\sqrt{l_1u_1 / \Delta bU_1}]. \qquad (5.1.17)$$

Assuming an equilibrium state, $u_{GB} \sim u_L$, the equilibrium interface thickness is given by

$$\delta_{eB} \sim \frac{\left[\frac{U_0}{l_0}u_0\sqrt{l_0u_0 / \Delta bU_0} + \frac{U_1}{l_1}u_1\sqrt{l_1u_1 / \Delta bU_1}\right]}{[U_0 / l_0 + U_1 / l_1]}. \qquad (5.1.18)$$

Substituting this into (5.1.10) and assuming, as before, $l \sim h$ and $u \sim U$ this yields

$$E \sim \frac{\left[\frac{U_0}{\sqrt{Ri_0}} + \frac{U_1}{\sqrt{Ri_1}}\right]}{h[U_0 / h_0 + U_1 / h_1]} Ri^{-1}. \qquad (5.1.19)$$

When fluid on only one side of the interface is entraining this reduces simply to

$$E \sim Ri^{-3/2}. \qquad (5.1.20)$$

Case 3: K-H Regime

When the stability of the interface is such that large-scale K-H instabilities can occur, then these dominate the thickening process. Interfacial mixing (thickening) is effected by turbulent billows, which result from the roll-up of K-H instabilities. The maximum amplitude, a_B, achieved by a billow (before buoyancy forces precipitate its collapse) is given by

$$a_B \sim \frac{(\Delta U)^2}{\Delta b}, \tag{5.1.21}$$

where ΔU is the velocity difference between the two layers. (This is suggested by the experiments of Thorpe 1973, with constant of proportionality ~ 0.6.) After a billow collapses, the time taken for eddies to re-sharpen the interface sufficiently to induce a successive instability is taken as

$$t_s \sim \frac{\delta}{u_L}, \tag{5.1.22}$$

so that the volume gained per unit area per unit time by the interface is

$$u_{GKH} \sim \frac{(\Delta U)^2}{\Delta b \delta} u_L. \tag{5.1.23}$$

(Here it is implicitly assumed that the time for a billow to form and collapse is considerably less than the time for eddies to re-sharpen the interface.)

Assuming an equilibrium state, $u_{GKH} \sim u_L$, the equilibrium interface thickness is given by

$$\delta_{eKH} \sim \frac{(\Delta U)^2}{\Delta b}. \tag{5.1.24}$$

Substituting this into (5.1.10) and assuming, as before, $l \sim h$ and $u \sim U$, this yields

$$E \sim \left[\frac{U^2}{\Delta bh}\right]\left[\frac{(\Delta U)^2}{\Delta bh}\right]. \qquad (5.1.25)$$

In the case when fluid on only one side of the interface is entraining, this simplifies to

$$E \sim Ri^{-2}. \qquad (5.1.26)$$

(Here it is assumed $\Delta U \sim U$.)

Energy Considerations

In the case when fluid on only one side of the interface is entraining, the rate of supply of energy to the interfacial region (per unit area) is

$$e_s \sim \frac{\rho u^2 l^2}{l t_e},$$

or using (5.1.4),

$$e_s \sim \rho u^3. \qquad (5.1.27)$$

The concomitant rate of gain of potential energy by the entraining layer (per unit area) is

$$e_{pe} \sim \Delta\rho g u_e l. \qquad (5.1.28)$$

The ratio of these, $\varepsilon = e_{pe}/e_s$, represents the fraction of eddy kinetic energy that is converted to potential energy, or the 'efficiency' of energy conversion. Using (5.1.27) and (5.1.28), and assuming $l \sim h$ and $u \sim U$, this gives

$$\varepsilon \sim \mathrm{RiE}. \tag{5.1.29}$$

The energy conversion efficiency in each mixing regime is now determined.

In the diffusion dominated regime,

$$\varepsilon \sim \mathrm{Pe}^{-1/2}. \tag{5.1.30}$$

As Pe decreases, δ/l increases and an increasing fraction of eddy kinetic energy goes toward raising fluid for permanent entrainment and a decreasing fraction goes into wave energy. (This does not violate the assumption of proportionality between wave energy and eddy kinetic energy, however, since it is assumed that ε is always small.) To maximize entrainment, the energy transferred to interfacial waves should be minimized since this energy is lost to viscous dissipation and to the mean flow through shear-wave interaction.

In the wave breaking regime,

$$\varepsilon \sim \mathrm{Ri}^{-1/2}. \tag{5.1.31}$$

Although a portion of energy supplied to interfacial waves in this case goes toward increasing δ/l (and enhancing entrainment), some fraction of wave energy is dissipated in the wave breaking process and is transferred back to the mean flow through shear-wave interaction. As Ri decreases, the energy lost (eventually) to dissipation and shear-wave interaction decreases (relatively) and the potential energy gain by the entraining layer increases.

In the K-H regime,

$$\varepsilon \sim \mathrm{Ri}^{-1}. \tag{5.1.32}$$

In this case K-H billows (which extract energy from the mean flow directly) dominate the thickening process so that energy transferred to interfacial waves contributes little to e_{pe}. As Ri decreases, δ increases (by K-H billowing) and a greater fraction of fluid scoured from the interface can be permanently entrained.

Mixing Regime Boundaries

The boundaries separating mixing regimes are now explored for the case when fluid on only one side of the interface is entraining.

As discussed in §4.2, it is found that cyclical K-H instabilities are active when Ri_s is less than about 0.4 to 0.45. Assuming $Ri_s=Ri_s(Ri)$, the criterion for (cyclical) K-H instability may be given equivalently as $Ri < Ri_c$ (Narimousa & Fernando 1987 suggest $Ri_c \sim 5$ in their experiments), which sets an upper bound on Ri for K-H mixing. The lower bound in the K-H regime is governed by Ri at the onset of (small-scale) turbulence in the interface. If the interface first becomes turbulent at $Ri=Ri_t$, then model results for K-H mixing should be valid for $Ri_t < Ri < Ri_c$.

In the wave breaking regime, it is assumed that mixing by shear-driven wave instabilities is effective when a/λ ($\sim Ri^{-1/2}$) is greater than some value, say $(a/\lambda)_c$. This effectively sets an upper bound on Ri for wave breaking, given by $Ri_b \sim [(a/\lambda)_c]^2$ (Narimousa & Fernando suggest $Ri_b \sim 20$ in their experiments).

When $Ri_c < Ri < Ri_b$, interfacial thickening by molecular diffusion is also active. Using (5.1.11), (5.1.17), (5.1.1), and (5.1.12), its contribution becomes important (relative to mixing by wave breaking) when

$$Pe = cRi, \tag{5.1.33}$$

where c is a constant of order 1000.

The proposed boundaries separating mixing regimes are shown in figure 5.1.2.

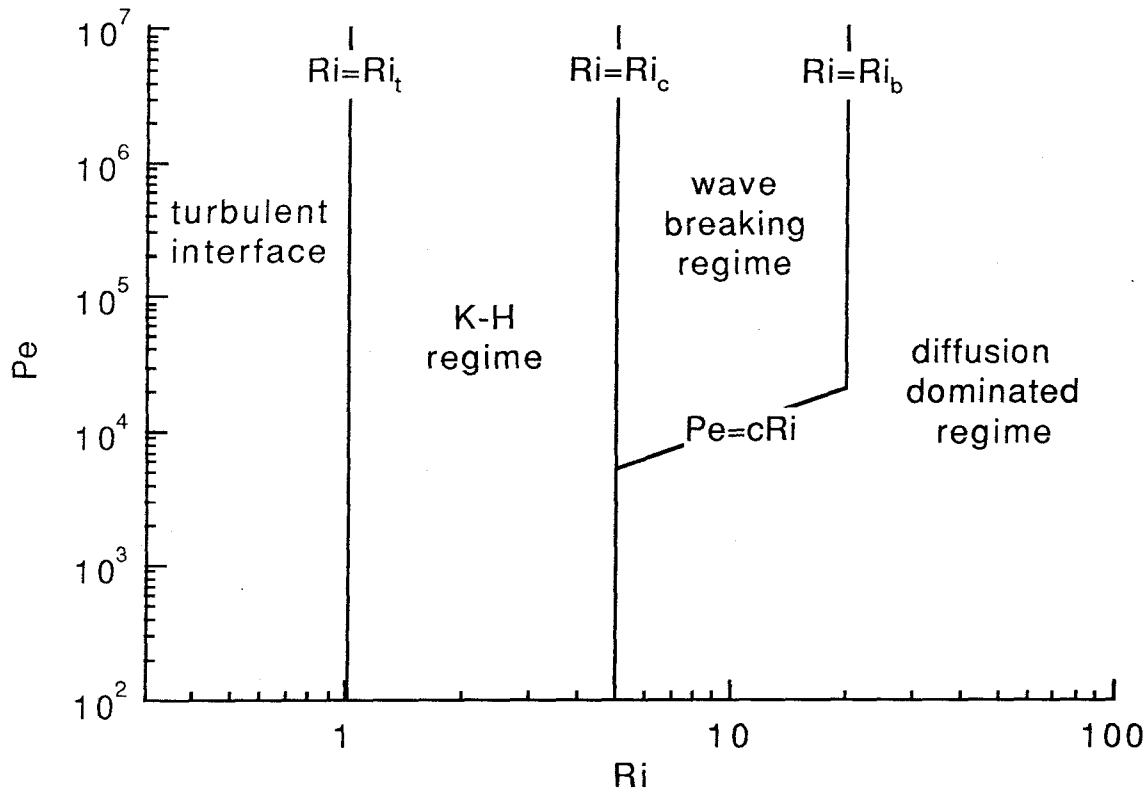

FIGURE 5.1.2. Mixing regime boundaries in Ri-Pe space. Numerical values of Ri and Pe delineating borders are only approximate.

5.2. Comparison with Experiment

To recapitulate, the main results from §5.1 for the case when fluid on only one side of the interface is entraining are: when interfacial mixing is primarily due to molecular diffusion,

$$\frac{\delta}{h} \sim Pe^{-1/2},$$

and

$$E \sim Ri^{-1}Pe^{-1/2};$$

when interfacial mixing is primarily due to interfacial wave breaking,

$$\frac{\delta}{h} \sim Ri^{-1/2},$$

and

$$E \sim Ri^{-3/2};$$

when interfacial mixing is primarily due to K-H instabilities,

$$\frac{\delta}{h} \sim Ri^{-1},$$

and

$$E \sim Ri^{-2};$$

and in all cases

$$\Gamma_m \sim Ri^{-1}.$$

Experimental results from the present study support the model predictions. As seen in figure 3.3.19, the data for Γ_m are well represented by $\Gamma_m \sim Ri^{-1}$ (independent of the dominant interfacial mixing mechanism), as predicted by the model. In figure 3.3.22 measurements (3) of interfacial thicknesses in the K-H regime are in agreement with the model result: $\delta \sim c_1(\Delta U)^2/\Delta b$, with $c_1 \sim 0.1$. Also, in the wave

breaking regime, interfacial thicknesses (2) are consistent with the model result, (4.2.2), with constant of proportionality ~ 0.4.

Results from previous studies also give support to the proposed entrainment model. Care must be taken, however, in assessing numerical values of E and Ri from different experiments as different investigators use different measures of velocity and length scales.

Entrainment results from Lofquist (1960) are re-plotted in figure 5.2.1. They may be interpreted as $E \sim Ri^{-2}$ for Ri less than about 5 and $E \sim Ri^{-3/2}$ for $5 < Ri < 10$, in agreement with model predictions (assuming, in his case, that mixing is K-H dominated for $Ri < 5$, and wave breaking dominated for $5 < Ri < 10$). For $Ri > 10$ the data are widely scattered due to difficulties associated with measuring low entrainment rates (it is also expected that diffusion effects become important at high Ri).

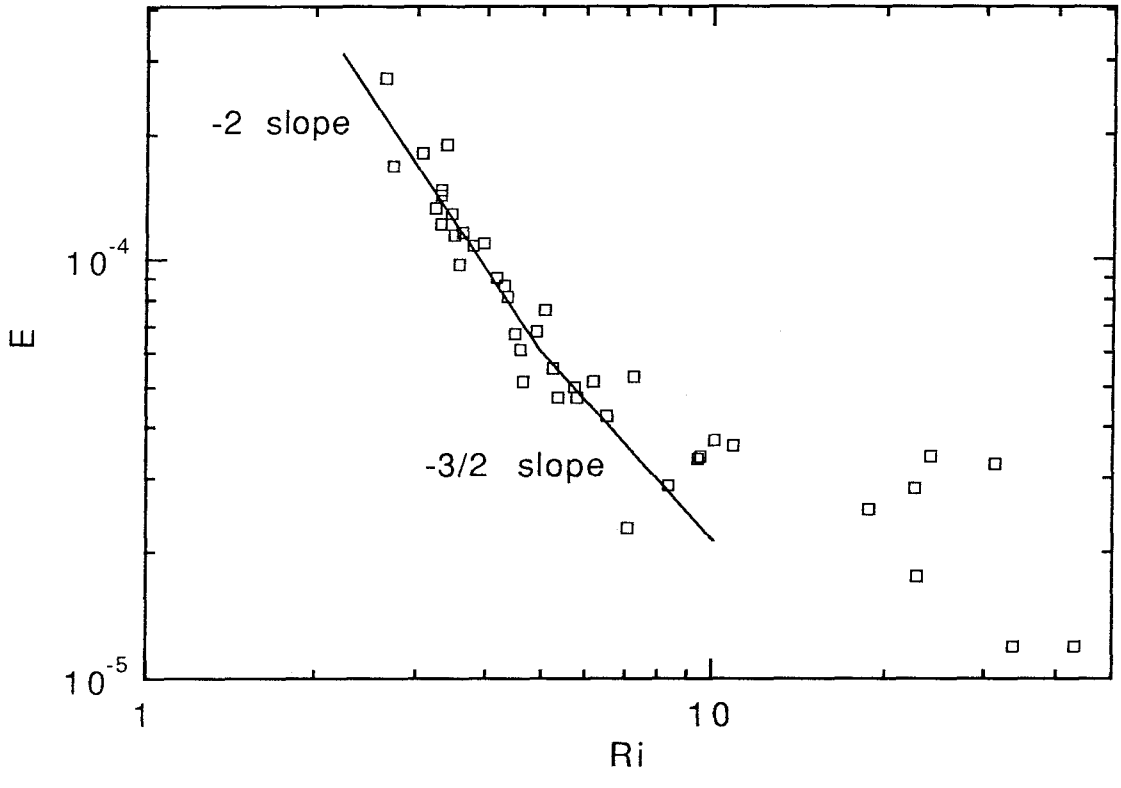

FIGURE 5.2.1. Entrainment results from Lofquist (1960). Here Ri is based on the mean layer velocity and the layer hydraulic radius (typically about one-third of the layer depth).

The entrainment results of Deardorff & Willis (1982) are re-plotted in figure 5.2.2. Their results may be interpreted as $E \sim Ri^{-2}$ for $0.7 < Ri < 3$ and $E \sim Ri^{-3/2}$ for $3 < Ri < 20$, in agreement with model predictions (assuming, in their case, that mixing is K-H dominated in the first range and wave breaking dominated in the second).

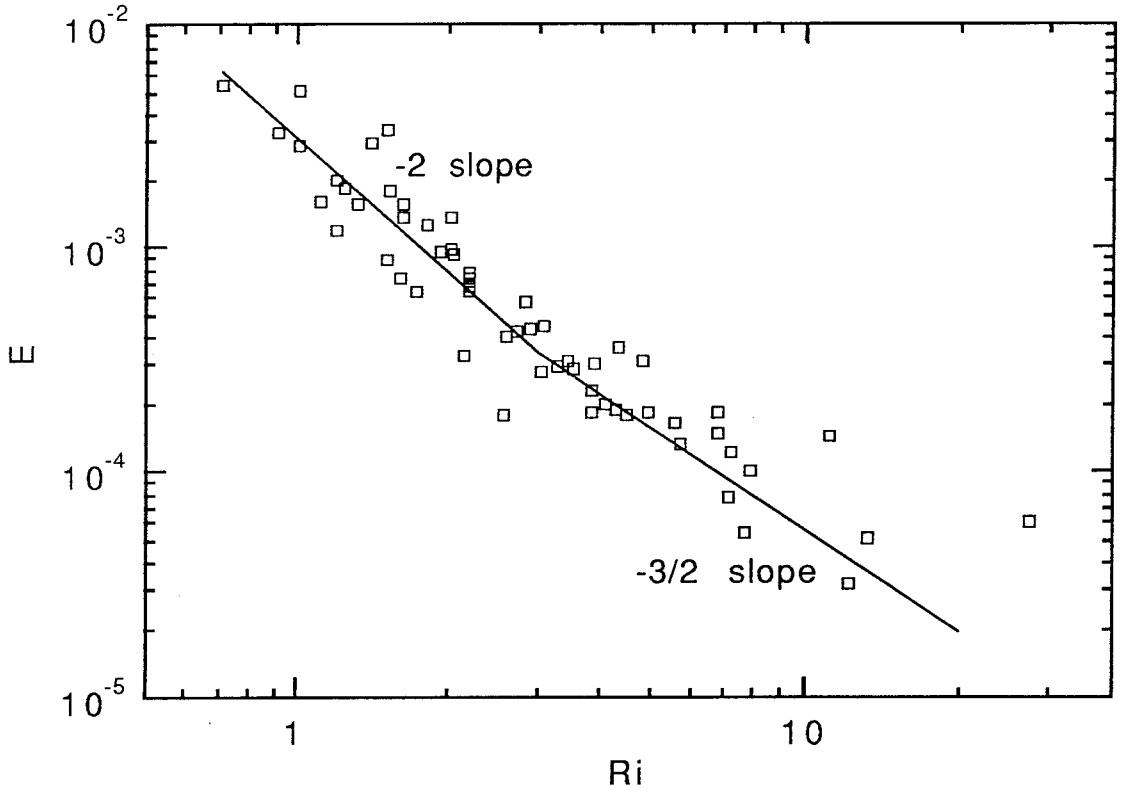

FIGURE 5.2.2. Entrainment results from Deardorff & Willis (1982). Here Ri is based on the mixed layer depth and the velocity jump at the interface.

Recent measurements of interfacial thicknesses by Stephensen & Fernando (1991) using LIF are re-plotted in figure 5.2.3. For Ri less than about 5 the data are well represented by $\delta/h \sim Ri^{-1}$, in agreement with the model result (assuming mixing is K-H dominated). For Ri > 5 their results are consistent with $\delta/h \sim Ri^{-1/2}$, however scatter in the data is appreciable.

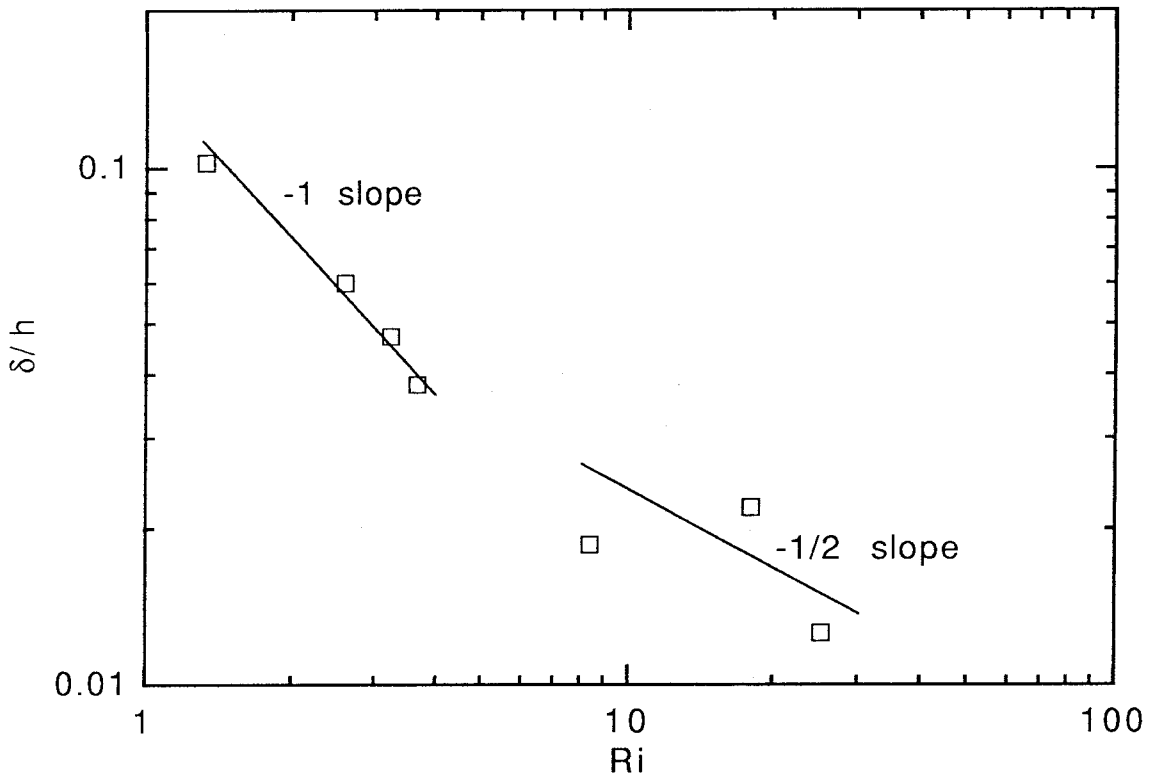

FIGURE 5.2.3. Mean interface thicknesses from Stephensen & Fernando (1991).

5.3. Application of Results

Phillips (1966) broadly classifies density interfacial entrainment as either (a) fully turbulent, (b) buoyancy attenuated turbulent, or (c) quasi-laminar. In the first case, buoyancy has negligible effect on turbulent motions (Ri<<1); the interface is grossly convoluted by large-scale eddies and entrainment proceeds as if the fluids are homogeneous. In the second case, buoyancy prevents large-scale deformations of the interface; however, the interface thickness, δ, is much smaller than the scale at which buoyancy forces are appreciable (given by the Ozmidov scale, $l_R \sim (\varepsilon/N^3)^{1/2}$, where ε is the dissipation rate and N is the Brunt-Väisälä frequency) and small-scale turbulence persists at the interface. In the third case, $\delta >> l_R$ and small-scale turbulent motions are inhibited at the interface. Results from this study fall into category (c): quasi-laminar entrainment.

Of course practical situations arise for which the present results are not applicable. Flows falling into category (a) or (b) are outside the region of validity of the entrainment model. Also, the model results are not applicable to flows where the density interface is replaced by a gradual buoyancy gradient, such as in a partially mixed estuary (results of Rohr *et al.* 1988 are relevant in this case).

Important problems for which the present results are directly applicable include: stratified estuary flow (with a sharp internal density interface), mixed layer deepening in the ocean, and mixed-layer growth beneath a temperature inversion in the atmospheric boundary layer.

The entrainment results may be directly incorporated in an integral formulation of the stratified estuary problem, akin to the approach taken by Ellison & Turner (1959). This method gives results for integral properties in each layer as a function of longitudinal position, such as mean velocity and species concentration, as well as the

mean position of the interface. (Of course numerical constants need to be determined by scale experiments for a given geometry.)

The model results may also be employed directly in the study of mixed layer growth in the upper ocean or atmospheric boundary layer. Ignoring Coriolis effects and assuming horizontally homogeneous flow with an initially linear buoyancy gradient, the mixed layer growth rate is given by

$$\frac{dD}{dt} = UE, \tag{5.3.1}$$

where D is the depth of the mixed layer (Kato & Phillips 1969). For simplicity it may also be assumed that U is constant and $\Delta b = N_0^2 D$, where N_0 is the initial Brunt-Väsälä frequency.

In the initial stages of growth it is expected that mixing is K-H dominated so that, using (5.1.26), the mixed layer growth rate is

$$\frac{dD}{dt} \sim \left(\frac{U^5}{N_0^4}\right) D^{-4}. \tag{5.3.2}$$

As Ri increases (D and Δb increase with time), mixing eventually becomes wave breaking dominated and, using (5.1.20),

$$\frac{dD}{dt} \sim \left(\frac{U^4}{N_0^3}\right) D^{-3}. \tag{5.3.3.}$$

As Ri further increases, interfacial mixing may become diffusion dominated, in which case, using (5.1.16),

$$\frac{dD}{dt} \sim \left(\frac{U^5 \kappa}{N_0{}^4}\right)^{1/2} D^{-5/2}. \qquad (5.3.4)$$

(Again, numerical constants in 5.3.2 to 5.3.4 need to be determined by scale experiments for a given flow geometry.)

CHAPTER 6

CONCLUSIONS

6.1. Discussion

As discussed previously, the present model predictions for entrainment and interface thickness receive support from experimental results from this study, and from the previous work of Lofquist (1960), Deardorff & Willis (1982), and Stephensen & Fernando (1991); however, some seemingly contradictory results appear in the literature, which must be reconciled.

As mentioned in §1.1, Ellison & Turner (1959) studied entrainment primarily over a range of Ri, $0 < Ri < 0.8$, in which the interface was turbulent; their results fall into Phillips' category (a) fully turbulent entrainment, or (b) buoyancy attenuated turbulent entrainment, and are not germane to the present study. It is expected that when flow at the interface is turbulent, adjacent layer fluid may be directly incorporated by the engulfing action of locally generated eddies (and subsequent diffusion and amplification of vorticity). In this case, present model results are no longer applicable; the entrainment relation is expected to be of a different form and any similarity to results of the present model for quasi-laminar entrainment would be entirely fortuitous.

Although entrainment results of Lofquist lend support to the current model, his results also suggest $\delta/h \sim$ constant for $2 < Ri < 40$, which is at variance with present model predictions and disagrees with experimental results from the present work and the results of Stephensen & Fernando. Narimousa & Fernando (1987) also suggest $\delta/h \sim$ constant for $1 < Ri < 15$. A lack of spatial resolution in both Lofquist's and Narimousa & Fernando's experiments may explain the apparent discrepancy,

especially in light of the fact that interface thicknesses measured using LIF in this study and those measured by Stephensen & Fernando are considerably smaller than the thicknesses measured by Lofquist and Narimousa & Fernando.

Kato & Phillips (KP, 1966) and Kantha, Phillips & Azad (KPA, 1977) use the shear velocity, u_*, to scale their results. Since the contribution to u_* from side-wall drag can be appreciable in their experiments (see Price 1979), it is difficult to compare their results with results from the present entrainment model. Price (1979) has attempted to re-scale the KP and KPA results using an inferred mean velocity, U; however, this analysis is questionable (see Deardorff & Willis 1982), and his derived result, $E \sim Ri^{-4}$, is dubious.

The results of Moore & Long (1971) suggest an entrainment relation $E \sim Ri^{-1}$ for $1 < Ri < 30$, in disagreement both with present model predictions and with results from Lofquist and Deardorff & Willis. Linden (1973) comments that jets employed by Moore & Long to generate their flow must have introduced additional turbulent length and velocity scales, not accounted for in a single Ri parameterization. The extent to which the jets influenced entrainment at the interface in their experiments is uncertain, and the relevance of Moore & Long's result is questionable.

More recent results from Narimousa & Fernando appear to follow $E \sim Ri^{-1.2}$ for $1.5 < Ri < 15$. This result is also at variance both with present model predictions and with results from Lofquist and Deardorff & Willis. The reason for this discrepancy is currently not understood; it is possible that peculiarities in start-up conditions may account for this, but more experimental information is necessary to find the definite cause for the disagreement.

Although the entrainment model developed by Linden (1973) pertains, strictly speaking, to zero-mean shear entrainment, it is instructive to compare his model to

that developed here. In his model, Linden assumes that large-scale eddies are responsible for the bulk of entrainment, and models them as a collection of coherent vortices. He assumes that the eddies, or vortices, randomly impinge on the interface, and entrainment is by ejection ('splashing') of adjacent layer fluid into the turbulent layer during the interface recoil stage (as suggested by his experiments using vortex rings). He assumes that potential energy gained through entrainment is proportional to kinetic energy supplied by the impinging eddies. He further assumes that the spacing between impinging eddies is proportional to the distorted eddy size, $l' \sim l\mathrm{Ri}^{1/2}$, and that the vortex interaction time scales with $\sqrt{l/\Delta b}$ (interface recoil time). From this he derives $E \sim \mathrm{Ri}^{-3/2}$, where Ri is defined in terms of characteristic velocity and length scales of the eddies.

In the current model, it is also proposed that large-scale eddies are responsible for the bulk of entrainment. However, the regime considered here is one in which eddies cannot fully penetrate the interface (and permanently entrain adjacent layer fluid); they can only scour pre-mixed, intermediate density fluid from the interfacial region. As in Linden's model, it is assumed that energy transferred to interfacial disturbances is proportional to the kinetic energy supplied by large-scale eddies. However, in contrast with Linden's work, the potential energy ultimately gained by the system is not assumed proportional to the energy supplied by the eddies. A fraction of interfacial disturbance energy (not proportional to the eddy kinetic energy) is lost through viscous dissipation and is transferred back to the mean flow through shear-wave interaction. It is also assumed in the present model that the spacing between entraining eddies scales with l (not l') and that an eddy will interact with the interface for a period of time that scales with l/u (not $\sqrt{l/\Delta b}$).

Linden's model was presumably developed to describe low Ri, zero-mean shear experiments; the present entrainment model is germane to cases in which a

mean shear exists, and Ri is large enough so that the interfacial flow is (quasi) laminar. The present model predicts $E \sim Ri^{-1}Pe^{-1/2}$, $E \sim Ri^{-3/2}$, and $E \sim Ri^{-2}$ in the diffusive, wave breaking, and K-H mixing regimes, respectively; Linden's model predicts $E \sim Ri^{-3/2}$. The agreement between the two in the present model's wave breaking regime is purely coincidental.

Mory (1991) has also developed an entrainment model for zero-mean shear mixing. In contrast with Linden's model, Mory assumes entrainment is due to small-scale eddies which induce (locally) high shear rates at the interface, resulting in small-scale K-H instabilities. He assumes that potential energy gained through K-H mixing (and subsequent advection of mixed fluid by turbulent eddies) is proportional to kinetic energy supplied by small-scale eddies. From this he derives $E \sim Ri^{-3/2}$, when Pe is large, and $E \sim Pe^{-1/3}Ri^{-1}$, for low to moderate Pe, where Ri and Pe are defined in terms of local turbulent length and velocity scales.

Contrary to the Mory model, experimental observations in the present work suggest entrainment is due to large-scale eddies; there appears to be no evidence of small-scale K-H type instabilities induced by small-scale eddies. Moreover, the scouring events and local interfacial instabilities (either K-H or wave breaking) in the present experiments appear to be uncorrelated in time.

To conclude this discussion, it is interesting to note the difference between interfacial waves generated in the zero-mean shear experiments of Hannoun & List (HL, 1988) and those in the present study. In the former case, it is suggested that interfacial waves, generated by random pressure fluctuations induced by turbulent eddies, induce local regions of intense shear in the interface which lead to breakdown by K-H instability (as first postulated by Phillips 1966). Wave energy is confined to a small region about the interface and the wave field becomes saturated (to the limit of

the Phillips instability) over a finite range of wavenumbers. In the present experiments, it appears that Phillips' mechanism for interfacial mixing is inactive since waves generated by turbulent pressure fluctuations are immediately distorted by the mean shear and either transfer energy back to the mean flow through shear-wave interaction (Phillips, 1966) or, if their initial aspect ratio (a/λ) is sufficiently large, become gravitationally unstable and break in a relatively short period of time (Frankignoul, 1972).

CHAPTER 6

CONCLUSIONS

6.1. Summary

High resolution velocity and concentration measurements have been made using combined LDV and LIF in two-layer, density stratified shear flows for Ri between about 1 and 10. Through the study of velocity and concentration data, mixing and transport mechanisms at the density interface have been identified, and a model for interfacial mixing and entrainment has been developed. The main results from the experiments and model are now summarized.

1. Profiles of mean and fluctuating velocity near the density interface for Ri between about 1 and 10 are qualitatively similar to those in an equivalent turbulent boundary layer flow over a rigid surface. Estimates of the Monin-Obukhov length show that the effect of the buoyancy flux on turbulence characteristics near the interface should be small.

2. The experiments suggest that entrainment in all cases is due to scouring by large-scale turbulent eddies; these act to sharpen the interface by stripping fluid from its outer edges.

3. In no cases studied is fluid entrained directly from one layer to the other; entrainment is always of premixed interfacial fluid of intermediate density.

4. Interfacial mixing is found to depend on the mean shear Richardson number, Ri_S. For Ri_S less than about 0.4 to 0.45, large-scale K-H instabilities are observed whose formation and growth into turbulent billows occurs in a cyclic manner; at larger

Ri_S, shear driven (finite-amplitude) wave breaking is observed. The net result of the instabilities in both cases is the local mixing of fluid and thickening of the interface.

5. A model for entrainment has been developed based on a local equilibrium hypothesis. It is suggested that if the flow is in an approximate (local) equilibrium then the rate of loss of fluid from the interfacial region by eddy scouring is balanced by the rate of production of mixed fluid by interfacial instabilities and molecular diffusion. The main results of the model for one-sided entrainment are as follows: when interfacial mixing is molecular diffusion dominated, $\delta/h \sim Pe^{-1/2}$ and $E \sim Ri^{-1}Pe^{-1/2}$; when mixing is wave breaking dominated, $\delta/h \sim Ri^{-1/2}$ and $E \sim Ri^{-3/2}$; when mixing is K-H dominated, $\delta/h \sim Ri^{-1}$ and $E \sim Ri^{-2}$; and in all cases the maximum concentration anomaly is $\Gamma_m \sim Ri^{-1}$.

6. Experimental results from this study support the proposed entrainment model: the data are in agreement with $\Gamma_m \sim Ri^{-1}$, and measured interfacial thicknesses are consistent with model results.

7. Results from previous studies also support the model: the entrainment data of Lofquist (1960) and Deardorff & Willis (1982) are in agreement with model predictions, as are the interfacial thickness measurements of Stephensen & Fernando (1991).

8. The one-sided entrainment model has been simply extended to include the case when both layers are entraining. In the latter case entrainment is no longer a simple function of Ri or Pe; rather it depends on combinations of parameters from both layers.

6.2. Suggestions for Future Work

In order to make progress in some reasonable period of time, the scope of this study has been necessarily restricted. During the course of the investigation, however, important issues have arisen whose study would have constituted the basis of several additional theses. These issues have therefore been only cursorily addressed and further study is needed. Such issues include: (1) the role played by sheared interfacial waves in the vertical transport of momentum and the dependence of the interfacial velocity gradient on local parameters; (2) the effect of Reynolds number on entrainment; (3) the influence of the buoyancy flux on properties of turbulence near and away from the interface; (4) the mechanics of interfacial wave generation by a turbulent shear flow; and (5) the evolution of finite-amplitude waves on a sheared density interface.

In addition, further experiments are desired to test the validity of the proposed entrainment model. In particular, high resolution measurements of interfacial thicknesses, maximum concentration anomaly, and scalar flux are desirable over a wide range of Ri.

It is anticipated that with recent advances in experimental, theoretical and computational techniques, further advances will be forthcoming so that mixing and entrainment can be confidently modelled in this important class of density-stratified shear flows.

References

ARMI, L. 1986 The hydraulics of two flowing layers with different densities. *J. Fluid Mech.* **163**, 27-58

BROADWELL J. E. & MUNGAL, M. G. 1991 Large-scale structures and molecular mixing. *Phys. Fluids A*, **3** 1193-1206

CLAUSER, F. H. 1956 The turbulent boundary layer. *Advan. Appl. Mech.* **4**, 1-51

CSANADY, G. T. 1978 Turbulent interface layers. *J. Geophys. Res.* **83**, C5, 2329-2342

DEARDORFF, J. W. & WILLIS, G. E. 1982 Dependence of mixed-layer entrainment on shear stress and velocity jump. *J. Fluid Mech.* **115**, 123-149

DRAIN, L.E. 1980 *The Laser-Doppler Technique*. Wiley-Interscience

DURST, F., MELLING, A. & WHITELAW, J. H. 1981 *Principles and Practice of Laser-Doppler Anemometry*, 2nd ed. Academic Press

ELLISON, T. H. & TURNER, J.S. 1959 Turbulent entrainment in stratified flows. *J. Fluid Mech.* **6**, 423-448

FERNANDO, H. J. S. 1991 Turbulent mixing in stratified fluids. *Annu. Rev. Fluid Mech.* **23**, 455-493

FRANKIGNOUL, C. J. 1972 Stability of finite amplitude internal waves in a shear flow. *Geophys. Fluid Dyn.* **4**, 91-99

GARTRELL, G. 1978 A signal processor for a laser-Doppler velocimeter. *Technical Memo. 78-5*, W. M. Keck Laboratory of Hydraulics and Water Resources, California Institute of Technology, Pasadena, Ca.

GARTRELL, G. 1979 Studies on the mixing in a density-stratified shear flow. Ph. D. thesis, California Institute of Technology, Pasadena, Ca.

GRASS, A. J. 1971 Structural features of turbulent flow over smooth and rough boundaries. *J. Fluid Mech.* **50**, 233-255

HANNOUN, I. A. 1985 Matching the refractive index in density stratified flows. *Technical Memo. 85-1*, W. M. Keck Laboratory of Hydraulics and Water Resources, California Institute of Technology, Pasadena, Ca.

HANNOUN, I. A. 1987 Turbulent mixing in stably-stratified fluids subjected to zero-mean shear. Ph. D. thesis, California Institute of Technology, Pasadena, Ca.

HANNOUN, I. A. & LIST, E. J. 1988 Turbulent mixing at a shear-free density interface. *J. Fluid Mech.* **189**, 211-234

HAZEL, P. 1972 Numerical studies on the stability of inviscid stratified shear flows. *J. Fluid Mech.* **51**, 39-61

KANTHA, L. H., PHILLIPS, O. M. & AZAD, R. S. 1977 On turbulent entrainment at a stable density interface. *J. Fluid Mech.* **79**, 753-768

KATO, H. & PHILLIPS, O. M. 1969 On the penetration of a turbulent layer into stratified fluid. *J. Fluid Mech.* **37**, 643-655

KEULEGAN, G. H. 1949 Interfacial instability and mixing in stratified flows. *J. Res. Natl. Bur. Stand.* **43**, 487-500.

KOOCHESFAHANI, M. M. 1984 Experiments on turbulent mixing and chemical reactions in a liquid mixing layer. Ph. D. thesis, California Institute of Technology, Pasadena, Ca.

LAWRENCE, G. A., BROWAND, F. K. & REDEKOPP, L. G. 1991 The stability of a sheared density interface. *Phys. Fluids A* **3**, 2360-2370

LIGHTHILL, M. J. 1962 Physical interpretation of the mathematical theory of wave generation by wind. *J. Fluid Mech.* **14**, 385-398

LOFQUIST, K. 1960 Flow and stress near an interface between stratified liquids. *Phys. Fluids* **3**, 158-175

LUMLEY, J. L., PANOFSKY, H. A. 1964 *The Structure of Atmospheric Turbulence.* Interscience

MONIN, A. S. & YAGLOM, A. M. 1971 *Statistical Fluid Mechanics: Vol. I*, MIT Press

MOORE, M. J. & LONG, R. 1971 An experimental investigation of turbulent stratified shearing flow. *J. Fluid Mech.* **163**, 27-58

NARIMOUSA, S., LONG, R. & KITAIGORODSKII, S. 1986 Entrainment due to turbulent shear flow at the interface of a stably stratified fluid. *Tellus* **38A**, 76-87

NARIMOUSA, S. & FERNANDO, H. J. S. 1987 On the sheared density interface of an entraining stratified fluid. *J. Fluid Mech.* **174**, 1-22

PAPANTONIOU, D. P. 1986 Observations in turbulent buoyant jets by use of laser-induced fluorescence. Ph. D. thesis, California Institute of Technology, Pasadena, Ca.

PHILLIPS, O. M. 1966 *The Dynamics of the Upper Ocean.* Cambridge University Press

PHILLIPS, O.M. 1977 Entrainment. In *Modelling and Prediction of the Upper layers of the Ocean* (ed. E. B. Kraus) Pergamon

PRESS, W. H., FLANNERY, B.P., TEUKOLSKY, S.A. & VETTERLING, W.T. 1989 *Numerical Recipes*. Cambridge University Press

PRICE, J. F. 1979 On the scaling of stress-driven entrainment experiments. *J. Fluid Mech.* **90**, 509-529

RASI, M. 1989 Mixing in density-stratified conjugate flows. Ph. D. thesis, California Institute of Technology, Pasadena, Ca.

RETICON 1981 *LC 300A Camera Manual.* EG & G Reticon

ROHR, J. J., ITSWEIRE, E. C., HELLAND, K. N., VAN ATTA, C. W. 1988 Growth and decay of turbulence in a stably stratified shear flow. *J. Fluid Mech.* **195**, 77-111

SIEGMAN, A. E. 1986 *Lasers*. University Science Books

STEPHENSEN, P. W. & FERNANDO, H. J. S. 1991 Turbulence and mixing in a stratified shear flow. *Geophys. Astrophys. Fluid Dyn.* **59**, 147-164

TENNEKES, H. & LUMLEY, J. L. 1972 *A First Course in Turbulence*. MIT Press

THORPE, S. A. 1973 Experiments on instability and turbulence in a stratified shear flow. *J. Fluid Mech.* **61**, 731-751

TURNER, J. S. 1973 *Buoyancy Effects in Fluids*. Cambridge University Press